

# **Measurement of the Antiproton to Proton Flux Ratio with the Alpha Magnetic Spectrometer on the International Space Station**

Der Fakultät für Mathematik, Informatik und Naturwissenschaften der RWTH Aachen  
University vorgelegte Dissertation zur Erlangung des akademischen Grades eines Doktors  
der Naturwissenschaften

vorgelegt von

**Sichen Li, M.Sc.**

aus

Xi'an

Berichter: Univ.-Prof. Dr. rer. nat. Stefan Schael

Univ.-Prof. Dr. rer. nat. Christopher Wiebusch



# Eidesstattliche Erklärung

Sichen Li erklärt hiermit, dass diese Dissertation und die darin dargelegten Inhalte die eigenen sind und selbstständig, als Ergebnis der eigenen originären Forschung, generiert wurden.

Hiermit erkläre ich an Eides statt

- 1 Diese Arbeit wurde vollständig oder größtenteils in der Phase als Doktorand dieser Fakultät und Universität angefertigt;
- 2 Sofern irgendein Bestandteil dieser Dissertation zuvor für einen akademischen Abschluss oder eine andere Qualifikation an dieser oder einer anderen Institution verwendet wurde, wurde dies klar angezeigt;
- 3 Wenn immer andere eigene- oder Veröffentlichungen Dritter herangezogen wurden, wurden diese klar benannt;
- 4 Wenn aus anderen eigenen- oder Veröffentlichungen Dritter zitiert wurde, wurde stets die Quelle hierfür angegeben. Diese Dissertation ist vollständig meine eigene Arbeit, mit der Ausnahme solcher Zitate;
- 5 Alle wesentlichen Quellen von Unterstützung wurden benannt;
- 6 Wenn immer ein Teil dieser Dissertation auf der Zusammenarbeit mit anderen basiert, wurde von mir klar gekennzeichnet, was von anderen und was von mir selbst erarbeitet wurde;
- 7 Kein Teil dieser Arbeit wurde vor deren Einreichung veröffentlicht.

Aachen, 16. Feb 2023

## *Abstract*

### **Measurement of the Antiproton to Proton Flux Ratio with the Alpha Magnetic Spectrometer on the International Space Station**

The measurement of the cosmic antiproton to proton flux ratio is a very sensitive probe of the sources of cosmic rays and their propagation. Cosmic antiprotons are assumed to be mainly secondary cosmic rays from interactions of primary cosmic rays like protons with the interstellar medium.

In this thesis, the antiproton to proton flux ratio has been measured with the AMS-02 experiment on the ISS in the rigidity range from 1 to 525 GV with data recorded between 2011 and 2021. In the rigidity range below 10 GV, cosmic rays are significantly affected by the time variation of the solar magnetic field. Antiprotons and protons propagate differently in the solar magnetic field. Therefore, the long-term precision measurements by AMS-02 allow for a deeper understanding of charge sign dependent solar modulation effects.

For the first time, in the rigidity range up to 18 GV, the antiproton to proton flux ratio is shown with a time resolution of 162 days, corresponding to six Bartels Rotations. Unexpectedly, a different time structure is observed than in the electron to positron ratio below 3 GV. The significance of the time structure decreases with increasing rigidity, and no significant time structure is observed for rigidities above 10 GV.

Antiprotons, like positrons, are sensitive probes for dark matter annihilation processes. No significant structures are observed in the time-averaged antiproton to proton flux ratio. The antiproton to proton flux ratio is expected to decrease for rigidities above  $\sim$ 40 GV. The slope in this rigidity range was measured to be  $(-1.44 \pm 0.42) \times 10^{-5}$ .

## CONTENTS

1 : INTRODUCTION . . . . .	1
2 : COSMIC RAYS . . . . .	3
2.1 Cosmic Rays . . . . .	3
2.2 Sources of cosmic rays . . . . .	5
2.3 Propagation . . . . .	7
2.4 Cosmic antiprotons measurement . . . . .	11
3 : AMS-02 EXPERIMENT . . . . .	13
3.1 Experiment Overview . . . . .	13
3.2 Transition Radiation Detector . . . . .	15
3.3 Silicon Tracker . . . . .	17
3.4 Time Of Flight . . . . .	22
3.5 Ring-Imaging Cherenkov Detector . . . . .	23
3.6 Electromagnetic Calorimeter . . . . .	25
3.7 Anti-Coincidence Counter . . . . .	26
4 : ANALYSIS . . . . .	28
4.1 Data Selection . . . . .	30
4.2 Charge Confusion Estimator . . . . .	36
4.3 TRD Estimator . . . . .	41
4.4 Template Fit . . . . .	41
4.5 Effective Acceptance . . . . .	58
4.6 Measuring Time . . . . .	60
4.7 Unfolding . . . . .	65
4.8 Antiproton To Proton Flux Ratio . . . . .	67
4.9 Systematic Uncertainties . . . . .	71
5 : RESULTS . . . . .	79
5.1 Time Averaged Result . . . . .	79
5.2 Time Dependent Result . . . . .	83
6 : SUMMARY . . . . .	89
Appendix A : Input variables for charge confusion estimator . . . . .	91

Appendix B : Table of Results . . . . .	97
Appendix C : Acronyms . . . . .	107
LIST OF FIGURES . . . . .	109
LIST OF TABLES . . . . .	113
BIBLIOGRAPHY . . . . .	115
ACKNOWLEDGEMENTS . . . . .	126

# CHAPTER 1

## INTRODUCTION

The story of cosmic rays began in 1912 when a balloon experiment carried out by Victor Hess showed a significant rise in the air ionization rate with increasing altitude, confirming the existence of cosmic rays [1] . The discovery of cosmic rays opened a new window to explore our universe supplementing the astronomical observations. Since then, enormous effort has been put in to identify the components of cosmic rays and to measure their flux in a wide energy scale range. Due to the very high levels of energy that cosmic rays can reach, they provide a unique opportunity to study high energy particles with energy above the TeV scale and even higher than the energy levels reached by modern particle colliders.

Before any particle accelerator was built, the main source to study high energy particles was the cosmic rays. The positron was firstly found in 1932 by Carl David Anderson in cosmic rays [2] . That was the first antiparticle to be discovered. After that, particle accelerators made great progress and the antiproton was discovered in 1955 by Emilio Segrè and Owen Chamberlain at the Bevatron particle accelerator [3] . The presence of antiprotons in cosmic rays was firstly confirmed in 1979 by two balloon experiments [4, 5] , the effort to study cosmic antiprotons has never stopped.

Due to the Earth's atmosphere, cosmic antiprotons can only be measured either by balloon experiments or space spectrometers. In this thesis, data collected by the AMS-02 experiment is used to determine the antiproton to proton flux ratio in time-averaged analysis and time-dependent analysis. The AMS-02 detector was installed on the International Space Station (ISS) in May 2011 and has a permanent magnet to distinguish the sign of the particles' rigidity. Up to May 2021, cosmic ray data of ten years has been collected, and is used for the present analysis.

The antiproton to proton flux ratio has been studied with the AMS-02 experiment and other experiments. Above 60 GV the antiproton to proton flux ratio is observed to be stable, rather than going down as predicted by traditional secondary production. This behavior indicates that an additional contribution like dark matter is needed or the cosmic ray propagation model needs to be revised. In this thesis, the updated antiproton to proton flux ratio will be given with the latest ten years dataset.

When the protons and antiprotons enter the heliosphere, they encounter a turbulent solar wind with an embedded heliospheric magnetic field (HMF), this leads to a time-dependent change in the antiproton to proton flux ratio. To observe this time structure in the flux ratio, long-time and precise measurements of cosmic protons and antiprotons are needed. Before the AMS-02 experiment, there was no continuous measurement of cosmic antiprotons. The balloon experiments measured cosmic antiprotons in several flights. The Space spectrometer PAMELA published time-averaged antiproton results [6] . Since AMS-02 has been monitoring cosmic rays continuously up to today, the time-dependent antiproton analysis is possible to be done with the data collected. In this thesis, the time-dependent antiproton to proton flux ratio is presented in six Bartels Rotations time resolution, this is the first time that the long-time structure of the antiproton to proton flux ratio is observed.

Chapter 2 presents a general picture of cosmic rays. An overview of the AMS-02 experiment and its sub-detectors is given in Chapter 3. Chapter 4 describes the antiproton analysis techniques used in this thesis. The result of time-averaged antiproton to proton flux ratio using ten years of AMS-02 data, as well as the time-dependent antiproton to proton flux ratio with a time resolution of six Bartels Rotations are presented in Chapter 5. Chapter 6 gives a summary and a conclusion on this thesis.

# CHAPTER 2

## COSMIC RAYS

### 2.1. Cosmic Rays

The humankind has been continuously driven by the curiosity to explore the unknown world. Up to today the highest particle energy that can be achieved through man-made particle accelerators is at the few TeV scale. To study the beyond, our universe itself serves as a tool. Universe is the ultimate laboratory for particle physics.

The spectrum of cosmic rays covers an incredibly wide range in intensity and energy. The measured cosmic ray flux is seen at Earth varying about 31 orders of magnitude, which corresponds to the scale of the visible Universe compared to the human hair diameter. The measured energy of cosmic rays can go up to the ZeV level ( $10^{21}$  eV), such an unprecedented energy can not be currently generated by man-made facilities. The large dynamic range can be seen in figure 2.1(a). As shown in this figure, the cosmic ray flux follows a power law:

$$\Phi(E) \propto E^{-\gamma} \quad (2.1)$$

where  $\Phi$  is the flux,  $E$  is the energy and  $\gamma$  is the spectral index.

The spectral index of the cosmic ray is around 2.7. Below  $10^{10}$  eV (10 GeV) the flux is lower than the power law extrapolation because low energy particles can be deflected by the solar magnetic field and not reach around the Earth. From around  $3 \times 10^{15}$  (3 PeV) to  $4 \times 10^{18}$  eV (4 EeV), the spectrum index steeps to around 3.1, which is called "knee". Above 4 EeV the spectrum index backs to around 2.7, the transition period is called "ankle". In addition, although the theoretical upper limit on the energy of cosmic ray protons, the Greisen–Zatsepin–Kuzmin (GZK) limit, is equal to  $5 \times 10^{19}$  eV (50 EeV) [7, 8], there are experiments, which appear to have detected cosmic rays with energies higher than this limit [9, 10]. This fact poses an unsolved puzzle that needs to be investigated. These features and observations are important to understand the sources of cosmic rays and their propagation.

Earth is constantly bombarded by subatomic particles. Due to the Earth's atmosphere, the ground-based cosmic rays experiments can only measure cascades of cosmic rays. To measure the cosmic rays directly, detectors have to be placed above the atmosphere. The AMS-02 experiment is conducted on the ISS, which maintains an orbit with an average altitude of 417 km, therefore it can precisely measure the cosmic rays avoiding their interactions with the atmosphere.

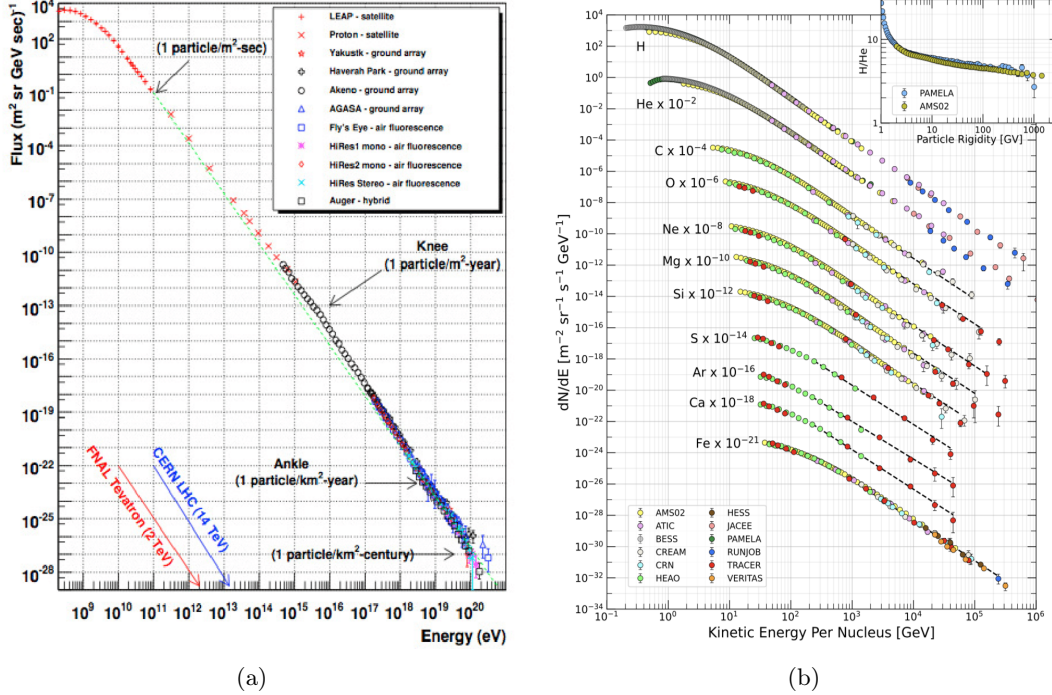


Figure 2.1: a) Cosmic ray spectrum has a wide range in flux and energy [11] , the knee is at around 1 PeV and the ankle is at 4 EeV. b) The fluxes of different components of cosmic rays follow a universal power law trend [12] .

There are two kinds of cosmic rays: primary and secondary. Primary cosmic rays are produced in astrophysical sources, while secondary cosmic rays are produced from the interactions between the primary cosmic rays and the interstellar medium. Primary cosmic rays mainly comprise protons, electrons, He, C, O, Ne, Mg, Si, Fe and others. Secondary cosmic rays consist of mainly positrons, antiprotons, Li, Be, B, F, and others. The precise measurement of cosmic rays can provide information about the astrophysical sources and also the propagation processes as well.

Cosmic rays consist of many components. For primary cosmic rays, 89% are protons, 10% are helium nuclei and around 1% are heavy elements. In figure 2.1(b) the fluxes of different cosmic ray components are shown. A universal power law spectrum is observed in all kinds of cosmic rays, which supports the assumption of a general electro-magnetic

acceleration mechanism, though small differences still need to be investigated. With the efforts of different measurements, the fluxes of cosmic ray components have been measured for a large energy range.

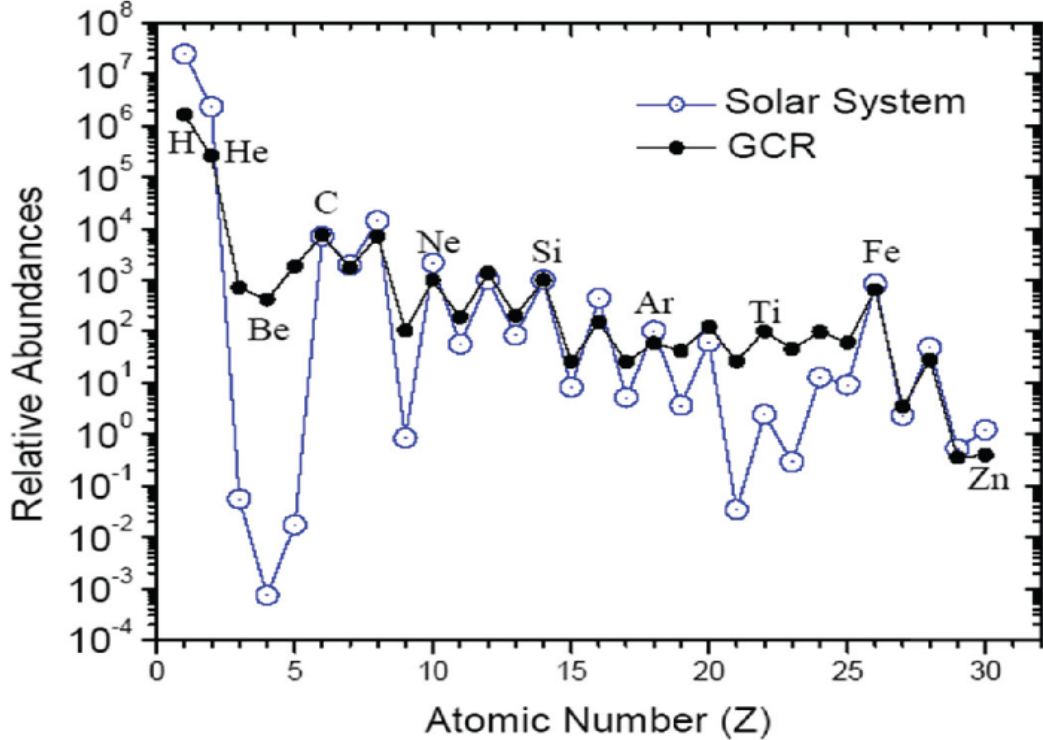


Figure 2.2: A good agreement of element abundances between the GCR and the solar system is shown [13] , except some differences like over-abundance of H and He in solar system, excess of Li, Be, B in GCR and others.

In figure 2.2, the abundances of the galactic cosmic rays (GCR) arriving near Earth compared to the ones of the solar system are shown. In general, there is good agreement between these two kinds of abundances, the differences illustrate the part of secondary production of cosmic rays. The reduced abundance of the galactic cosmic hydrogen and helium is due to the effects of the solar magnetic field. Due to the spallation and interactions of the cosmic rays, the C, N and O nuclei would break into elements of lower mass, namely Li, Be, and B. This fact explains the higher abundances of Li, Be and B in the GCR.

## 2.2. Sources of cosmic rays

Traditionally, the supernova remnants (SNRs) are considered to be the main source of cosmic rays. This idea was firstly suggested by Baade and Zwicky in 1934 [14] . Apart from SNR, some other sources can also contribute to cosmic rays production, like pulsars can produce electron and positron pairs then accelerate them in the pulsar wind nebula (PWN), or dark matter can produce additional positrons and antiprotons from annihilation. Therefore, a

high precision measurement of the cosmic ray flux is certainly a probe to understand the sources of cosmic rays.

A supernova is a stellar explosion event that can expel several solar masses of material with very high speed. There are mainly two mechanisms of supernova creation [15] : a) a white dwarf accretes matter from a companion star until it reaches the Chandrasekhar mass limit and then a nuclear fusion is triggered, and b) a massive star undergoes gravitational core collapse. During a supernova explosion, matter is ejected and accelerated at velocities of a few percent of the speed of light. As the ejected material travels faster than the speed of sound in the Interstellar Medium (ISM), it creates an expanding shock wave that sweeps up the interstellar material of gas and dust creating a "supernova remnant" [16] .

Charged particles can be absorbed into the supernova remnant and be confined in it. They gain energy and are accelerated while trapped in the supernova remnant until their energy is large enough to escape from it. The acceleration mechanisms are called "First Order Fermi Mechanism" and "Second Order Fermi Mechanism". The first one describes the particles crossing the shock front repeatedly gaining energy [17] . The second one describes the acceleration from the particle collisions with magnetic clouds in the interstellar medium [18] . These acceleration processes in the supernova remnant eventually lead to a power law energy spectrum.

Apart from the SNRs, pulsars can also produce high energy cosmic rays. Pulsars are rapidly rotating neutron stars with a strong magnetic field. A PWN is usually formed around a pulsar within the shell of a supernova remnant, where electrons and positrons can be produced by pair production [19, 20] . The shock of the PWN with the surrounding matter can accelerate these charged particles to very high energies [21, 22] . This effect results in an important contribution to the cosmic electron and positron spectra in the high energy range.

Since particles are produced via pair production and proton (antiproton) is much heavier than electron (positron), pulsars can produce positrons while antiprotons can not be produced by pulsars [23, 24] . Therefore, the contribution of cosmic antiprotons to the cosmic ray spectrum, can only result from the interactions between the primary cosmic rays and the ISM. Based on this, some models give the predictions of the antiproton flux or antiproton to proton flux ratio purely from secondary production [25, 26] . By comparing the measurement of the cosmic antiproton, if an excess in the cosmic antiproton is observed, different sources of antiproton production, like dark matter should be investigated [27, 28, 29] . For example, dark matter can produce additional positrons and antiprotons via annihilation besides secondary production, the additional components from dark matter plus the secondary production could be used to fit the measured cosmic antiproton spectrum [30] . In summary, by measuring the antiproton spectrum precisely, the sources of cosmic antiprotons can be studied.

## 2.3. Propagation

### 2.3.1. Cosmic rays propagating in the galaxy

When the accelerated cosmic rays leave the SNRs, they travel through the Galaxy and then interact with the ISM producing secondary cosmic rays. By hadronic production, antiprotons can be generated. Positrons and electrons lose their energy by bremsstrahlung and synchrotron radiation in the interaction collisions. Due to their charge, cosmic rays are scattered on the magneto-hydrodynamic (MHD) waves, so their trajectory is deflected from a straight line. The path of cosmic rays can be described by a diffusion process. The effects of this diffusion, as well as other physical effects, can be quantitatively described by the transport equation [31] :

$$\frac{\partial \psi(\vec{r}, p, t)}{\partial t} = q(\vec{r}, p, t) + \vec{\nabla} \cdot (D_{xx} \vec{\nabla} \psi - \vec{V} \psi) + \frac{\partial}{\partial p} p^2 D_{pp} \frac{\partial}{\partial p} \frac{1}{p^2} \psi - \frac{\partial}{\partial p} \left[ \dot{p} \psi - \frac{p}{3} (\vec{\nabla} \cdot \vec{V}) \psi \right] - \frac{1}{\tau_f} \psi - \frac{1}{\tau_r} \psi \quad (2.2)$$

where  $\psi(\vec{r}, p, t)$  is the density of cosmic rays at point  $\vec{r}$  with momentum  $p$ . The terms of the equation describe different physical processes and are explained here:

- $q(\vec{r}, p, t)$  denotes the source term, that includes the primary sources, and the contributions from spallation and decay processes.
- $D_{xx}$  is the spatial diffusion coefficient that describes the scattering off the magneto-hydrodynamic waves.
- $\vec{V}$  is the convection velocity. The galactic winds cause an additional convective transport.
- $D_{pp}$  is the momentum diffusion coefficient. Apart from the spatial diffusion process, charged particles traveling in MHD waves undergo stochastic re-acceleration that can be described by the momentum diffusion coefficient.
- $\vec{\nabla} \cdot \vec{V}$  denotes the adiabatic momentum change, this term is the work against the pressure of the interstellar gas.
- $\tau_f$  and  $\tau_r$  are the time scales of fragmentation and radioactive decay respectively.

For each particle type a propagation equation is used, leading to a very complex system of differential equations. To solve these equations analytically is impossible, therefore numerical calculations are more practical, like Monte-Carlo based approaches. Software numerical tools that are widely used to obtain the solution of the transport equation are the following: GALPROP [32] , USINE [33] , and DRAGON [34] .

Alternatively, it is possible to solve simplified approximations of Eq. 2.2. The basic assumption is that the galaxy is a box where particles can freely propagate while undergoing only elastic scattering. In this case, the density of cosmic rays does not depend on the location within the box. At the edge of the box, the particles are reflected with a probability  $1 - P_{\text{esc}}$ , and the  $P_{\text{esc}}$  is the probability of escaping to the outside of the box. As a consequence, the diffusion term can be replaced by escape time  $\tau_{\text{esc}}$ . With this assumption, the transport equation can be simplified as:

$$\frac{\partial \psi(\vec{r}, p, t)}{\partial t} = \psi_0(p) \cdot \delta(t) - \frac{\psi(p, t)}{\tau_{\text{esc}}} \quad (2.3)$$

where  $\tau_{\text{esc}}$  is escape time which represents the constant escape probability,  $\psi_0(p)$  is the injection homogenous source of particles at the time  $t=0$ . This simplified approximation is called the Leaky-Box model [35] and its solution is:

$$\psi(p, t) = \psi_0(p) \exp\left(-\frac{t}{\tau_{\text{esc}}}\right) \quad (2.4)$$

### 2.3.2. Cosmic ray propagating in the heliosphere

The Sun is continuously ejecting from its upper atmosphere a stream of charged particles when the energy of those particles surpasses the escape limit, this form the solar wind [36, 37]. The solar wind plasma drags outwards the solar magnetic field forming the HMF [38]. Because of the rotation of the Sun, the HMF has a spiral shape which is called Parker spiral, and the shape of the HMF is changing with the Sun's activity. The opposite polarity of HMF is separated by the heliospheric current sheet (HCS). The charged particles of the solar wind reach speeds of around 400 km/s, meaning they are faster than the speed of the magnetosonic wave, therefore they are supersonic. After traveling for some distance and encountering the interstellar medium, the speed of the solar wind abruptly decelerates and becomes subsonic at the termination shock [39]. Figure 2.3(a) shows a diagram of the heliosphere. The Voyager 1 probe became the first spacecraft to cross the termination shock in 2004 and later in 2012 to encounter the heliopause [40]. As shown in Figure 2.3(b), the solar wind particle rate dramatically decreases after reaching the outer border of the heliosphere.

Sunspot is a spot that looks darker than the surrounding areas on the Sun's photosphere, which represents solar activity. During the solar maximum, the number of sunspots reaches the maximum and the polarity of the HMF reverses. The sunspot number changes in a cycle of 11 years. Considering the polarity, a full cycle of the Sun's activity is 22 years [42]. The solar cycles have been counted since 1755 and now we are in solar cycle 25 [43, 44].

When galactic cosmic rays enter the solar system, they travel through the heliosphere first before reaching the Earth. The propagation process is similar to the propagation in the

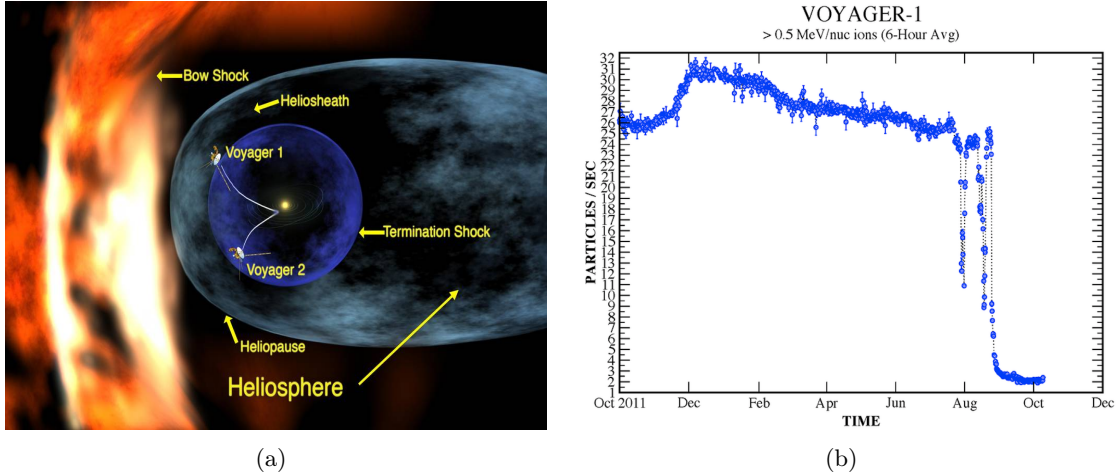


Figure 2.3: a) Diagram of the heliosphere. Credit: NASA/Walt Feimer; b) Particle rate detected by Voyager 1 (from October 2011 through October 2012) [41].

galaxy but the diffusion coefficient is orders of magnitude smaller. Since the full transportation equation can not be solved analytically, a simplified model proposed in [45] is usually used and it describes the process as the diffusion through the HMF. In this model, under the force-field approximation, an analytical solution of the one-dimensional steady-state equation is derived, which relates the GCR spectrum measured at Earth  $J$  and in the local interstellar space  $J_{\text{LIS}}$ :

$$J(T_E) = \frac{T_E(T_E + 2M)}{T_{\text{HP}}(T_{\text{HP}} + 2M)} J_{\text{LIS}}(T_{\text{HP}}) \quad (2.5)$$

where the  $M$  is the particle mass,  $T_E$  and  $T_{\text{HP}}$  are the kinetic energies of the particle at Earth and at the heliopause.  $T_{\text{HP}} = T_E + Z\phi$ , and  $\phi$  is called modulation potential, which depends on the solar wind speed and the diffusion coefficient. Since the solar activity and the physical status of the heliopause vary following the 22-year cycle, the measured GCR spectrum at Earth also shows a variation of the 22-year cycle. This is called solar modulation.

In the figure 2.4, the different ground-based cosmic neutron measurements and the monthly mean sunspot numbers are shown. The cosmic neutron counts show the intensity of hadronic cosmic rays, which indicate the measured cosmic rays at Earth. The sunspot numbers are correlated to solar activity. When the GCRs enter the solar system, they interact with the solar wind and magnetic fields. A large solar activity reduces the cosmic rays and vice versa. Therefore, the sunspot numbers and the cosmic neutron counts are anti-correlated. By measuring the cosmic ray flux over a long period of time, the impact of solar activity can be studied. Until recently, the only continuous cosmic ray flux measurements over a long period of time have been performed only for the dominant components of the cosmic spectrum like protons, helium, electron or neutrons produced in cascades in the Earth's atmosphere. There

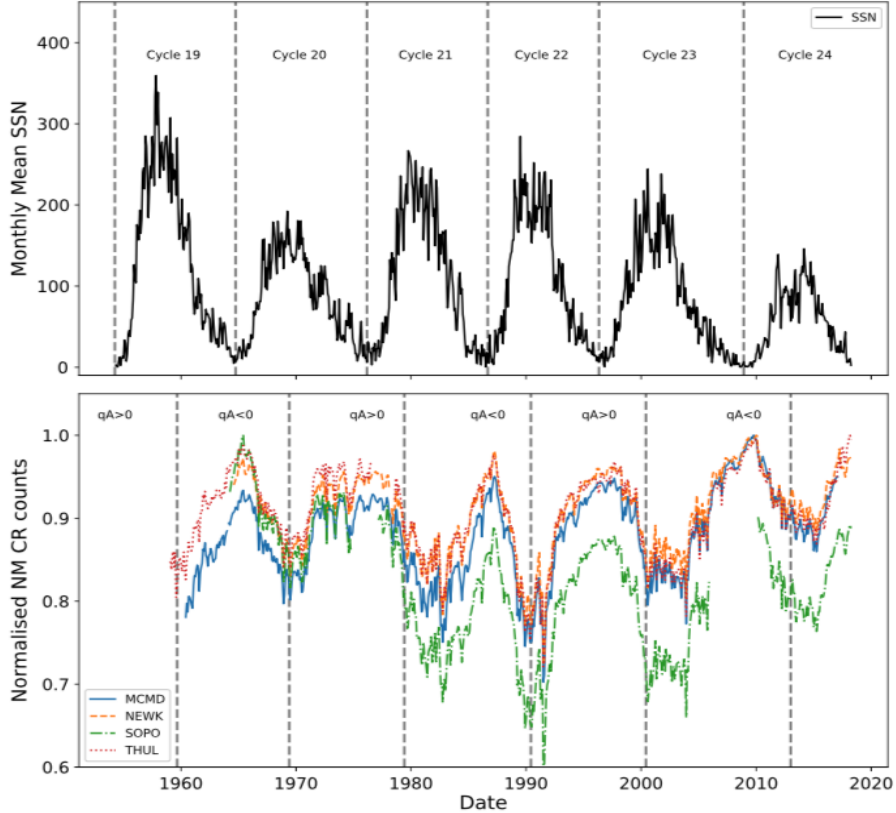


Figure 2.4: Bottom figure: The cosmic rays (CR) intensity recorded by neutron monitor (NM) counts from four different stations (MCMD = McMurdo, NEWK = Newark, SOPO = South Pole, THUL = Thule). The vertical lines show the approximations of epochs of solar magnetic-field polarity reversals and  $qA$  is the solar polarity. Top figure: Monthly mean sunspot numbers (SSN) over the latest six solar cycles. The vertical lines show the beginning of each solar cycle. The figure is taken from [46] .

is no continuous measurement of rare cosmic ray components like antiproton. Since the AMS-02 experiment has been collecting cosmic data for 10 years, the first time-dependent antiproton measurement can be achieved.

Due to the sign of charged particles, they drift differently in different polarities. For example, in positive polarity, the positively charged particles drift toward the Sun from the heliospheric poles and outwards to Earth. While the negatively charged particles drift arriving at Earth inwards along the HCS. This leads to different diffusion processes in the heliosphere. This charge-dependent modulation results in a different behavior between antiprotons and protons, furthermore, the antiproton to proton flux ratio behaves differently in opposite polarity periods. Similarly, positron and electron also behave differently due to opposite charge signs. In the time-dependent positron to electron flux ratio measurement by AMS-02 [47] , this can be observed. Also, the reversal of polarity is not easy to be determined clearly. The measurement of the positron to electron flux ratio can provide

information about the reversal period.

## 2.4. Cosmic antiprotons measurement

Cosmic rays were discovered in 1912 [1] , the antiproton was discovered in 1955 [48] , and the first measurements of cosmic antiproton component were performed in 1979 [4, 5] , when two pioneering balloon flight experiments published their results about cosmic antiprotons independently. The first one was carried out by Bogomolov et al. and the data taking was from 1972 to 1977 by three individual flights, the residual air was  $11 \text{ g/cm}^2$  so a correction was needed. The result showed two candidates of cosmic antiprotons in the kinetic energy range of 2-5 GeV. The second one was carried out by R. L. Golden et al. in Palestine in Texas and the data taking was from June 21 to June 22 1979. The residual air in the flight altitude was  $5.4 \text{ g/cm}^2$ . The spectrometer had a superconducting magnet and the group reported 46 antiproton candidates from 5.6 to 12.5 GV.

After decades of effort, many cosmic ray experiments published results about cosmic antiprotons. For example, the BESS experiment, which is a balloon flight experiment [49] , had nine successful flight campaigns since 1993. Then the apparatus was upgraded and renamed as BESS-Polar. The BESS-Polar was carried out in 2004 and 2008 respectively in the Antarctic [50, 51] and both flights measured the cosmic antiprotons [52, 53] . In the final result from the BESS-Polar II experiment, the group used data taken from Dec 2007 to Jan 2008 (a period corresponding to a solar minimum) and reported the measurement of 7886 cosmic antiprotons in the kinetic energy range from 0.17 to 3.5 GeV [53] .

Due to the limited height of the balloon flight experiments, the correction of the residual air has to be considered to get a flux result above the atmosphere. The correction that the residual air creates can be overcome if a spectrometer is placed in space where the residual air is negligible.

The first satellite-based cosmic antiproton measurement was performed by the PAMELA detector. PAMELA's mission lasted from June 2006 to February 2016 at a float altitude between 350 km and 610 km. The orbital period of the host satellite Resurs-DK1 was 94 min [54] . The PAMELA group published several antiproton results and the last one was in 2012 [6, 55, 56] with a maximum measured energy of 350 GeV [6] . This result shows a relatively flat antiproton to proton flux ratio in the high energy range, which is different from the traditional prediction of cosmic antiprotons from purely secondary production. In 2016 the AMS-02 experiment published its first result on cosmic antiprotons extending the measured rigidity range up to 450 GV using cosmic ray data collected during the first four years of its operation [57] . The details of the AMS-02 experiment will be shown in the next chapter.

Apart from the experiment mentioned above, there are other balloon experiments that measured cosmic antiprotons. The antiproton flux results from these experiments are given in figure 2.5.

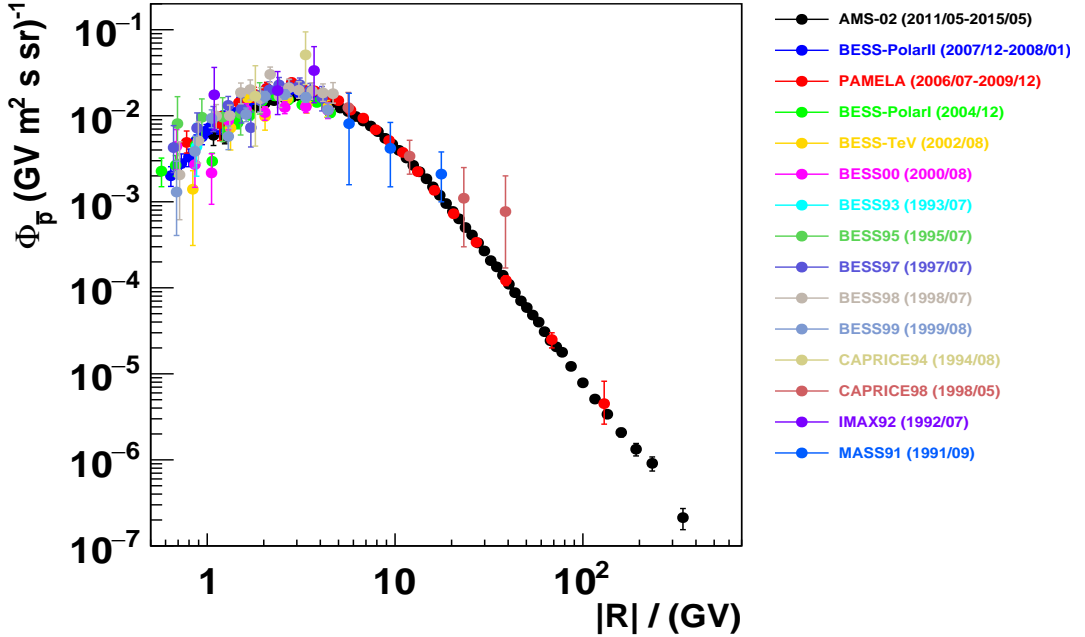


Figure 2.5: The antiproton flux measured by AMS-02 [57] , BESS-Polar II [53] , PAMELA [6] , Bess-Polar I [52] , Bess-TeV [58] , BESS00 [59] , BESS93 [60] , BESS95 [61] , BESS97 [62] , BESS98 [63] , BESS99 [59] , CAPRICE94 [64] , CAPRICE98 [65] , IMAX92 [66] , MASS91 [67] .

Compared to antiproton measurement, the proton measurement is much easier since it is overwhelmingly dominant in cosmic rays. Many experiments have published the measurements of cosmic protons [68, 69, 70, 71, 72, 73] . In this thesis, I will focus on the antiproton to proton flux ratio. Proton is primary cosmic ray and antiproton is believed to be secondary cosmic ray. Therefore, the antiproton to proton flux ratio is a probe to study the secondary to primary cosmic ray ratio, which can be used to investigate the source and the propagation of cosmic rays. Since the proton flux is about  $10^4$  times greater than the antiproton flux, measuring the antiproton flux to 1% accuracy requires a separation power of  $\sim 10^6$ . This leads to a challenge in high-energy measurement.

# CHAPTER 3

## AMS-02 EXPERIMENT

### 3.1. Experiment Overview

The Alpha Magnetic Spectrometer (AMS) experiment was proposed by Nobel laureate Prof. Samuel Ting from MIT in 1994 and was soon accepted [74]. The goal of the experiment is to search for antimatter and dark matter in the universe and to provide precise measurements of the fluxes for different components of the cosmic rays, which is crucial for understanding the sources of cosmic rays and their basic propagation model [75].

To test the feasibility of a particle spectrometer in space, a prototype called AMS-01 (figure 3.1(a)) was designed, which was a simplified version of the final detector. The test flight was conducted in 1998 during the space shuttle mission STS-91 [76], see figure 3.1(b). By collecting cosmic ray data for ten days, the test flight proved that placing and operating a spectrometer in space is possible.

After several years of construction and testing, the AMS-02 detector was launched aboard the space shuttle Endeavour during mission STS 134 from Kennedy Space Center on 16 May 2011. Three days later, the detector was installed on the ISS's S3 Upper Inboard Payload Attach Site and began collecting data. Figure 3.2 shows the location of AMS-02 on the ISS.

The AMS-02 detector has a size of  $5\text{ m} \times 4\text{ m} \times 3\text{ m}$  and weighs 7.5 t [80]. It has a permanent magnet that provides a magnetic field of 0.14 T and in combination with nine silicon tracker layers the rigidity of the cosmic particles can be measured. Within the magnet, the Anti-Coincidence Counters (ACC) are used as a veto system to reject particles entering the detector sideways. At the top of the experiment, there is a Transition Radiation Detector (TRD), which can distinguish light and heavy particles. Above and below the magnet there are two Time-Of-Flight (TOF) systems which provide the trigger and the measurements of the velocity and the charge of the particles. Below the lower part of the TOF, a Ring-Imaging Cherenkov (RICH) detector is located so the particle's velocity can be measured. At the bottom of the detector, there is an Electromagnetic Calorimeter (ECAL) which measures the energy of the particles. The geometry of all the sub-detectors is illustrated in figure 3.3.

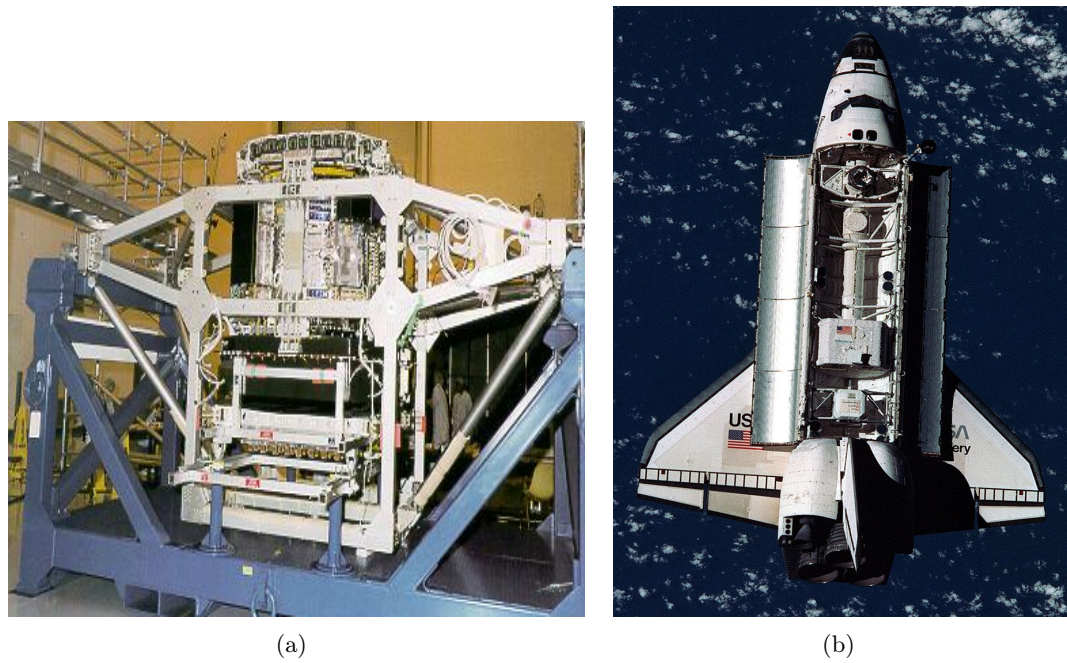


Figure 3.1: a) The AMS-01 detector at the Kennedy Space Center (NASA) with its support structure [77] ; b) The AMS-01 detector aboard the Space Shuttle Discovery during the STS-91 mission in June 1998 [78] .



Figure 3.2: The AMS-02 detector mounted on the ISS S3 Upper Inboard Payload Attach Site (Image modified from [79] ).

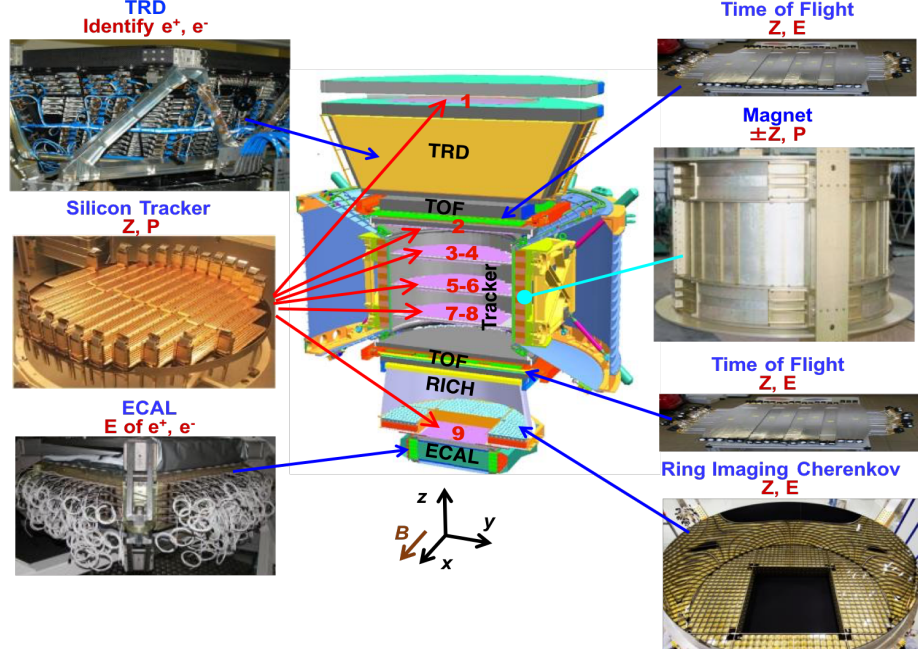


Figure 3.3: Schematic view of the AMS-02 experiment and all its sub-detectors [81] .

Detector operations have been conducted since the launch to make the experiment run smoothly. These operations can be distinguished in flight and ground operations. As part of the flight operations, the collected data is transmitted from the ISS to tracking and data relay satellites (TDRS). Then through the S (low rate) and Ku (high rate) radiofrequency bands, the data is transmitted to the White Sands Ground Terminal (WSGT) in New Mexico. Over the NASA networks, the data is then directed to the Marshall Space Flight Center (MSFC) and is written on disk. At last, the data is transmitted over the Internet and copied to the Payload Operations Control Centre (POCC) at CERN.

### 3.2. Transition Radiation Detector

The TRD can separate different particles based on the transition radiation emitted. Transition radiation is emitted when a relativistic charged particle goes through the boundary between two different media with different dielectric constants [82] . The emitted radiation is produced due to the different solutions of Maxwell's equations of the electric and magnetic fields of the moving charged particle in these two media, so photons have to be emitted when the particle crosses the boundary. The intensity of the emitted photon is proportional to the Lorentz factor  $\gamma$ , so for a relativistic charged particle, the emitted transition radiation photons have wavelengths in the X-ray range of the electromagnetic spectrum and their direction is mostly forward. The angle between transition radiation and particle path is proportional to  $1/\gamma$ .

The AMS-02 experiment has a transition radiation detector placed on the top of the ex-



Figure 3.4: The TRD and its support structure during construction [81] .

periment between the tracker layer one and the upper TOF layer [83, 84] . The TRD has 5248 proportional straw tubes; each one has a 6 mm diameter and a maximum length of 2 m. The straw tubes have double-layer kapton-aluminum foil walls of 72  $\mu\text{m}$  in thickness and at their center there is a 30  $\mu\text{m}$  gold-plated tungsten wire. The tubes are filled with a xenon (Xe) and carbon dioxide (CO<sub>2</sub>) gas mixture, which is supplied by two storage tanks (5 kg CO<sub>2</sub> and 49 kg Xe). When a charged particle goes through the straw tube it ionizes the Xe atoms and the produced electrons drift towards the anode wire creating an avalanche of ionization proportional to the energy loss of the particle. Finally, a signal is induced on the anode wire. The CO<sub>2</sub> quenches the environment and reset it to its initial state. So far, no detectable large leak in the AMS-02 TRD gas system has been observed. Due to gas diffusion across the tube walls, the loss of CO<sub>2</sub> is around 0.47 g/day and the loss for Xe is negligible. This ensures that the TRD can be stably operated until 2039.

The TRD tubes are assembled in 328 modules and one module has 16 tubes. Furthermore, all these modules are mounted in 20 layers. Twelve layers are placed along the Y axis in the middle of TRD, four layers are placed along the x-axis on top, and four layers along the x-axis are on the bottom. In figure 3.4, the TRD and its support structure are shown.

Figure 3.5(a) shows an illustration where an electron and a proton go through one TRD layer. The upper part of the layer is a 20 mm thick fleece radiator, which consists of 10  $\mu\text{m}$  thick polypropylene or polyethylene fibers. The lower part of the layer is made of straw tubes. When a relativistic charged particle goes through the radiator, transition radiation may be produced. For example, the  $dE/dX$  signal can be recorded after a proton traverses

the layer. While an electron passes the layer, the transition radiation can also be collected in straw tubes. Figure 3.5(b) shows the energy distributions measured by TRD straw tubes for 60 GeV protons, pions, muons and 20 GeV electrons during a test beam at CERN. Due to the transition radiation emitted by electrons, there is an additional contribution from the transition radiation photons at around  $\sim 10$  keV in the electron's spectrum.

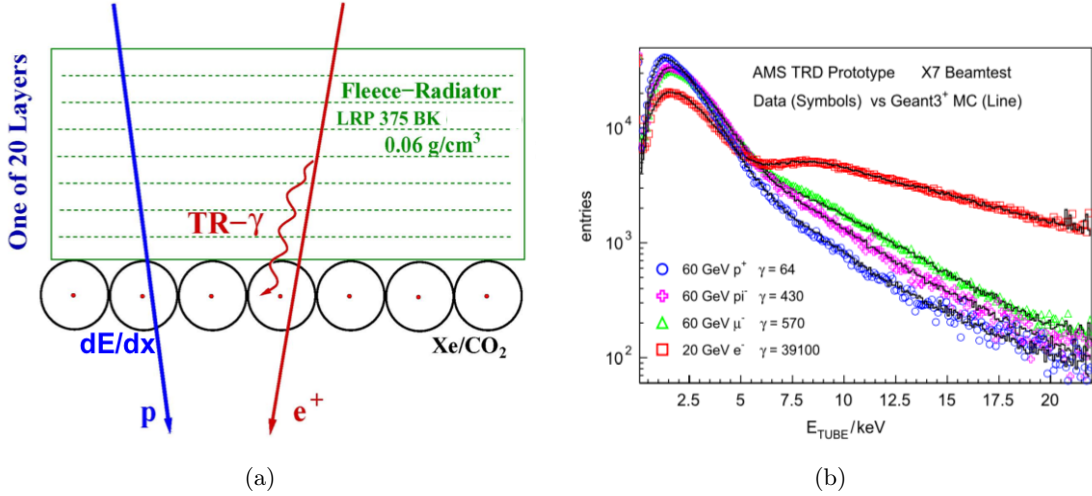


Figure 3.5: Illustration of the TRD separation between electrons and protons: a) the transition radiation emitted by a positron while the proton can only produce the  $dE/dX$  signals in the TRD [81] ; b) the energy distributions measured by TRD straw tubes for 60 GeV protons, pions, muons and 20 GeV electrons during a beam test at CERN [85] .

### 3.3. Silicon Tracker

To measure the rigidity and its sign, the AMS-02 detector is equipped with a silicon tracker and a magnet. The magnet used in the AMS-02 experiment is a permanent magnet with a 0.14 T magnetic field. The magnet has 64 Nd-Fe-B sectors arranged in a cylindrical shaped structure with a height of 0.8 m and an inner diameter of 1.1 m. The produced magnetic field is almost linear, and the magnetic field direction is defined as the X direction, the vertical direction is the Z direction, so the particle bending plane is the YZ plane. Outside the magnet, the leaking magnetic field is negligible so that the design can minimize the effect of the Earth's magnetic field on the ISS. In figure 3.6, the permanent magnet used in AMS-02 is shown.

The tracker of AMS-02 has nine silicon layers: the first layer is on the top of the TRD, the second layer is above the magnet and below the upper TOF, layers 3 to 8 are the so-called inner tracker layers as they are installed inside the permanent magnet and layer 9 is placed above the ECAL and below the RICH. In total, all nine layers have 2264 double-sided silicon micro-strip sensors. They are arranged into 192 ladders [87, 88] . The total active measurement area is 6.75  $m^2$ . Each ladder has 1024 readout strips, 640 on the p-side and



Figure 3.6: Preparing for test of the permanent magnet in China Academy of Launch Vehicle Technology (CALT) [81] .

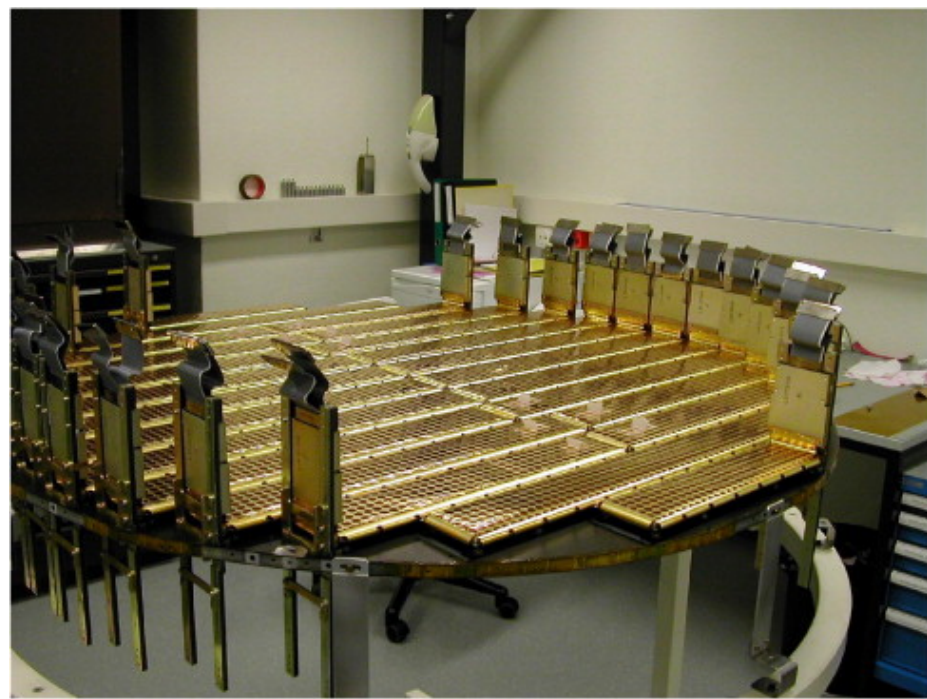


Figure 3.7: A silicon tracker inner plane fully equipped with ladders [86] .

384 on the n-side of the silicon sensors. So in total, there are 196608 readout channels. In figure 3.7, a tracker inner plane equipped with ladders is shown.

Each double-sided silicon micro-strip sensor has a size of  $41.360 \times 72.045 \text{ mm}^2 \times 0.3 \text{ mm}$ . When a particle goes through the sensor it creates electron-hole pairs in the middle. The created electrons drift toward the n-side and the holes toward the p-side. The X position measurement is obtained from the n-side and the Y position measurement is obtained from the p-side. Figure 3.8 illustrates the process. The tracker's design results in spatial resolution of  $10 \mu\text{m}$  and  $30 \mu\text{m}$  in the bending and non-bending direction respectively for protons. Given the track hit positions, the rigidity and its sign can be reconstructed. By default, the rigidity is reconstructed with all the tracker layer hits.

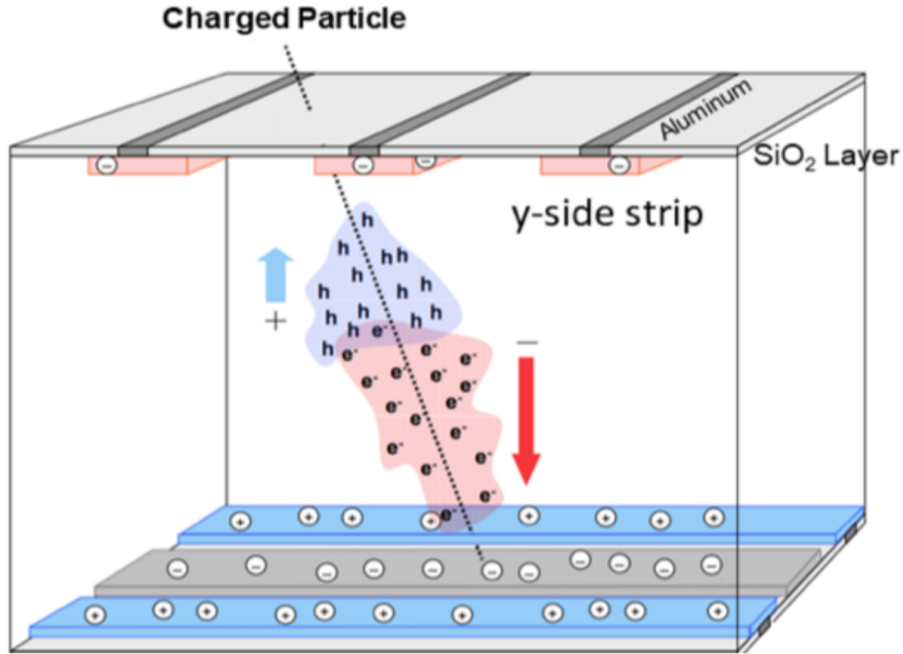


Figure 3.8: Principle of the operation of the double-sided silicon micro-strip sensors. The electron-hole pairs produced by a charged particle drift towards the strips of the sensor as showing in this figure [81].

According to the presence of the tracker track hits in the different layers, various categories of tracker patterns can be defined. The tracker pattern definitions are given in table 3.1. In this table,  $\checkmark$  denotes "have a hit associated to the track in this layer" and  $\times$  denotes "does not have a hit associated to the track in this layer".

In addition, the deposited ionization energy  $dE/dX$  is proportional to the square of the particle charge ( $Z^2$ ). Therefore, the charge measurement in each layer can be obtained. The charge resolution of the inner tracker layers is  $\Delta Z = 0.05$  for the charge of one particle.

The positions of the inner tracker layers are aligned and monitored by the Tracker Alignment System (TAS), which consists of 20 infrared laser beams that provides sub-micrometer

Table 3.1: Table of the tracker pattern definitions.

Tracker Pattern	Layer 1	Layer 2	Layer 9
0	✓	✓ or ×	✓
1	✓	✓	×
2	×	✓	✓
3	✓	×	×
4	×	✓	×
5	×	×	✓
-1	×	×	×

position measurements [89, 90]. The positions of layers 1 and 9 are aligned with respect to the inner tracker by using cosmic rays over two-minute time windows. The resulting position accuracy is 5  $\mu\text{m}$  for layer 1 and 6  $\mu\text{m}$  for layer 9.

Before the launch of AMS-02, the whole detector was tested and calibrated at the CERN SPS test beam facilities with 180 GeV and 400 GeV proton beams, as well as with positron, electron, and pion beams of 10 to 290 GeV. The tracker rigidity resolution function was determined with high precision and compared to MC simulation. Figure 3.9 shows the comparison between the tracker resolution measured at the 400 GeV proton beam and the one obtained by MC simulation. A good agreement between data and MC is observed.

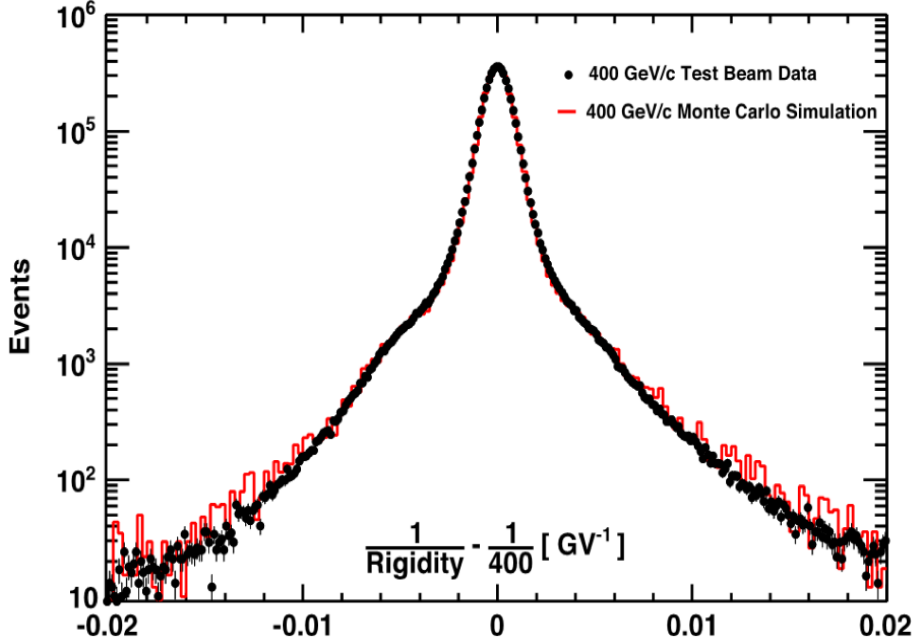


Figure 3.9: Comparison between the tracker resolution measured with 400 GeV protons at the test beam and the MC simulation [81].

Due to the resolution of the tracker and the multiple scattering [91] , the resolution of the momentum measurement can be described by:

$$\left(\frac{\sigma_p}{p}\right)^2 = \left(\sqrt{\frac{720}{N+4}} \frac{\sigma_x p \sin \theta}{0.3BL^2}\right)^2 + \left(\frac{0.2}{\beta B \sqrt{LX_0} \sin \theta}\right)^2 \quad (3.1)$$

where  $p$  is the momentum of the charged particle,  $B$  is the magnetic field,  $N$  is the equidistant measurements,  $\theta$  is the track inclination angle,  $L$  is the track length in the bending plane,  $\sigma_x$  is the sagitta resolution in the bending plane,  $\beta = \frac{v}{c}$ , and  $X_0$  is the radiation length of the traversed medium.

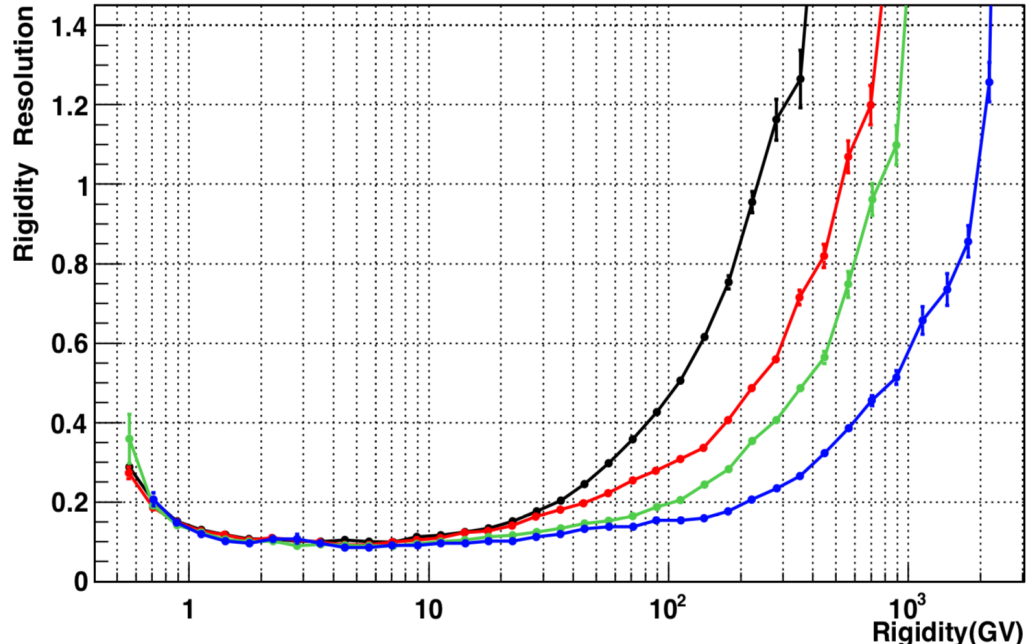


Figure 3.10: The AMS-02 tracker resolution from MC simulation for protons [92] . The four curves are for different tracker patterns: Black for inner tracker only, red for inner tracker plus layer 1, green for inner tracker plus layer 9 and blue for inner tracker plus layer 1 and 9.

In this equation, the momentum measurement equation consists of two terms. The first term describes the contribution of the tracker resolution and the second term the contribution of the multiple scattering. Since  $R = pc/Ze$ , the rigidity resolution is obtained. The AMS-02 tracker resolution has been studied extensively. In figure 3.10, the AMS-02 simulated rigidity resolution for cosmic protons is shown. Below 1.5 GV, the rise is due to the multiple scattering, and the rise in the high rigidity range is mostly due to the detector's resolution. The maximum detectable rigidity (MDR) is defined as the value of the rigidity  $R$  where  $\sigma_R = R$ . This value is usually used to describe the highest rigidity that can be measured. For the AMS-02 tracker, the MDR for the protons in the full span (tracker pattern 0) is

around 2 TV.

The heat produced by the electronics and radiators of the tracker can be removed by the Tracker Thermal Cooling System (TTCS). The TTCS is a two-phase CO<sub>2</sub> cooling system with four cooling pumps. Due to aging and technique problems, the old four pumps were replaced by four new pumps in several spacewalks from November 2019 to January 2020.

### 3.4. Time Of Flight

AMS-02 has four planes of TOF counters, plane 1 and 2 are above the magnet (Upper TOF), and plane 3 and 4 are below the magnet (Lower TOF) [93, 94]. Planes 1, 2, and 4 consist of eight plastic scintillator paddles, while plane 3 has ten paddles. The paddles have different lengths between 117 and 134 cm and a thickness of 1 cm. In the upper and lower TOF, the two planes are arranged in the X and Y directions as shown in figure 3.11. To avoid possible gaps between the paddles, the paddles are placed with a 0.5 cm overlapping. Each paddle is also equipped with 2 or 3 Photo-Multiplier Tubes (PMTs) on each end, which collect the light signal from the plastic scintillator and provide efficient particle detection.

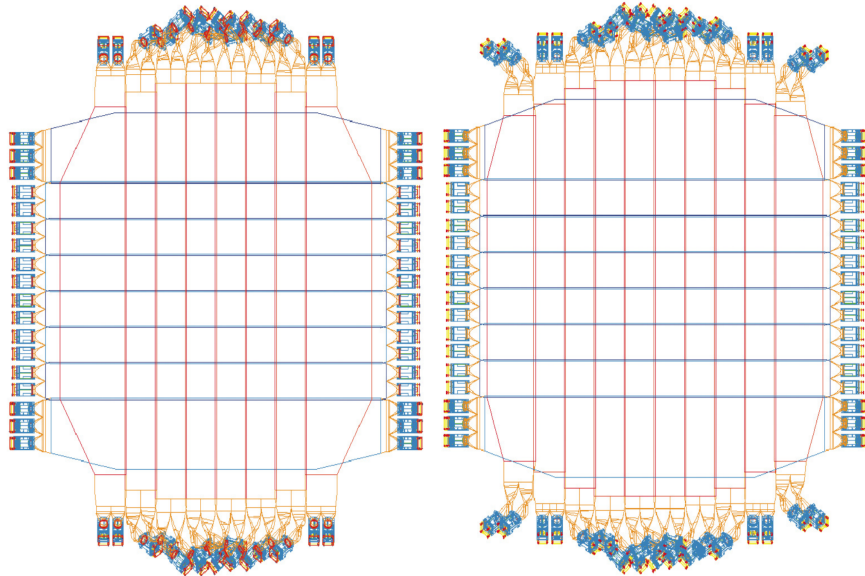


Figure 3.11: The TOF planes arrangement in the AMS-02 experiment. Left: Upper TOF and Right: Lower TOF [95].

The TOF system provides the particle's velocity by measuring the time difference between signals from the upper and lower TOF. Each counter's time resolution is around 160 ps, and the combined  $\beta$  resolution is around 4% for  $\beta \approx 1$  and  $Z = 1$  particles (figure 3.12(a)). This provides the ability to discriminate between the up-going and down-going particles. Also, since the particle's mass is determined by:

$$m = \frac{ZR}{\beta\gamma} \quad (3.2)$$

combined with the rigidity measurement from tracker, the particle's mass can be obtained.

Apart from measuring the velocity, the TOF can also provide the particle's charge. By measuring the ionization energy loss  $dE/dX$ , the charge of the particles can be independently obtained from the anode and dynode signals of the PMTs. The charge resolution is  $\Delta Z = 0.05$  for charge one particles (figure 3.12(b)).

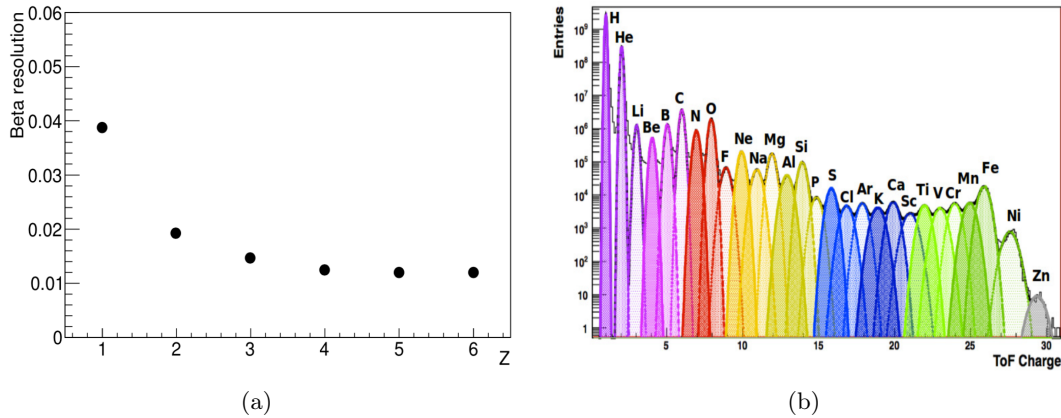


Figure 3.12: a) The TOF  $\beta$  resolution as a function for particle charge [95] ; b) The TOF charge distribution from protons ( $Z=1$ ) up to Zinc ( $Z=30$ ) [95] .

### 3.5. Ring-Imaging Cherenkov Detector

In the AMS-02 experiment, the RICH is installed below the lower TOF and above the ECAL. The RICH can measure the velocity and the charge of relativistic particles. It has two kinds of radiators at its top: a sodium fluoride (NaF) radiator in the center surrounded by a silica aerogel (Agl) radiator. Below the two radiators, there is an expansion volume in the middle and a PMT plane at the bottom [96, 97] . In figure 3.13, the components of the RICH are shown. The whole RICH has the shape of a cone with an upper radius of 60 cm, a lower radius of 67 cm, and a height of 47 cm.

When a charged particle traverses a dielectric radiator with a velocity greater than the velocity of light in this material, the particle emits a cone of Cherenkov photons. By measuring the emission opening angle of the Cherenkov radiation cone  $\theta = \arccos(1/n\beta)$ , the  $\beta$  of the particle can be obtained. The RICH in the AMS-02 experiment has a radiator plane of two non-overlapping radiators. The central radiator consists of 16 NaF tiles with a size of 85 mm  $\times$  85 mm  $\times$  5 mm each and a refractive index of  $n=1.33$ . Surrounding the NaF, there are 92 silica aerogel tiles with a size of 115 mm  $\times$  115 mm  $\times$  25 mm each and a refractive

index of  $n=1.05$  [96] .

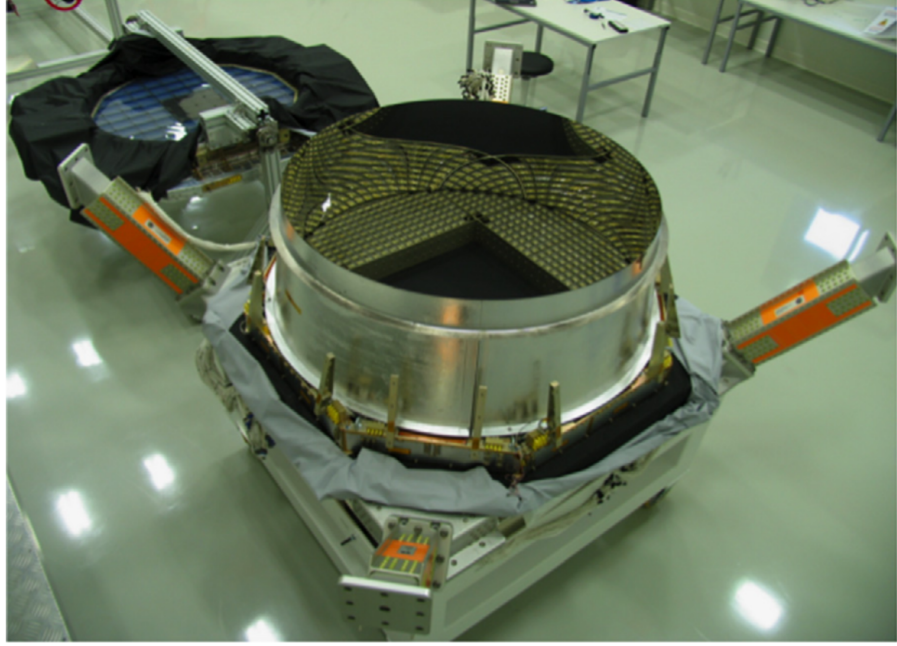


Figure 3.13: The RICH PMT plane and its expansion volume at the front of the picture and the two radiators in the background [98] .

Since  $\beta = v/c$  and  $n = c/v$ , this leads to the requirement that particles which pass through the NaF radiator should have a velocity  $\beta > 0.75$  in order to be detected, while those which pass through the AgI radiator should have a velocity  $\beta > 0.953$ .

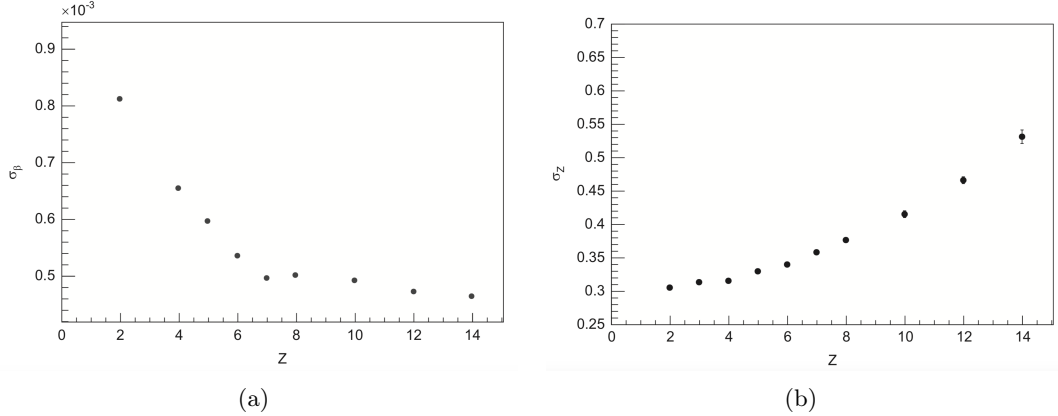


Figure 3.14: a) The RICH  $\beta$  resolution as a function of particle charge for the aerogel radiator [99] ; b) the RICH charge resolution as a function of particle charge [99] .

A highly reflective mirror surrounds the expansion volume to increase the detection efficiency.

The PMT detection plane at the bottom is equipped with 680 PMTs of  $4 \times 4$  multi anodes. These PMTs detect the Cherenkov photons emitted in the radiators, and the effective spatial granularity is  $8.5\text{ mm} \times 8.5\text{ mm}$ . Since the sum of the signal amplitudes is proportional to  $Z^2$ , the charge of the particle can also be measured.

The velocity resolution of RICH is  $\sim 10^{-3}$  for charge one particles for the aerogel radiator (figure 3.14(a)). The charge measurement of RICH provides a resolution better than 0.5 for particles of charge up to 12 (figure 3.14(b)).

### 3.6. Electromagnetic Calorimeter

The ECAL in the AMS-02 experiment can precisely measure the longitudinal and lateral electromagnetic shower development and also the deposited energy [100, 101]. It has a lead-scintillating fiber sandwich structure with an active area of  $648\text{ mm} \times 648\text{ mm}$ , a thickness of 166.5 mm and a weight of  $\sim 500\text{ kg}$ . The ECAL has 98 lead foils and 50000 scintillating fibers in total. The entire structure corresponds to 17 radiation lengths ( $X_0$ ).

The ECAL consists of 9 superlayers with a thickness of 18.5 mm each. Each superlayer is made of 11 grooved lead foils alternated with ten fiber layers glued together with optical epoxy (figure 3.15) [102], while the last foil of the last superlayer is made of aluminum. In each superlayer, the fibers are oriented along one direction only. By alternatively stacking the nine superlayers in the X and Y directions (five superlayers in the X direction and four in the Y direction), the 3D image of the shower shape is obtained. Each superlayer's fibers are read out by 36 PMTs at only one end. In total, the ECAL has 324 PMTs [103].

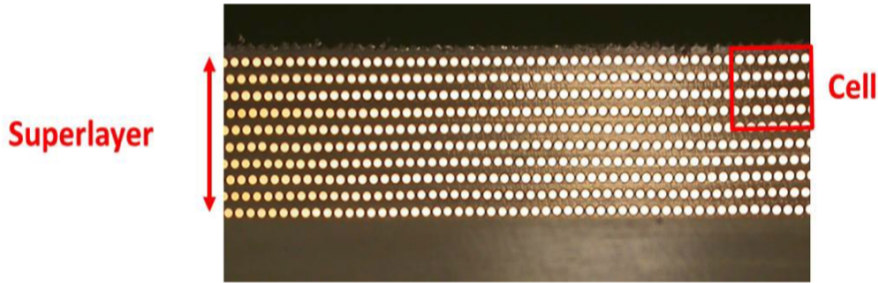


Figure 3.15: The ECAL superlayer structure. One cell is shown in red [103].

When a particle goes through the ECAL, it interacts in an electromagnetic or hadronic way producing a shower [104]. When an electron or positron traverses the ECAL, it emits photons by bremsstrahlung, then the emitted photons convert to electrons and positrons further by pair production, so a cascaded electromagnetic shower develops. While a proton or antiproton traverses the ECAL, it passes as a minimum ionizing particle (MIP) and leaves a relatively clear track. The produced hadronic shower primarily consists of pions and kaons which can interact or decay further. Due to the transverse momenta for massive secondaries and the possible production of neutral particles, the hadronic shower is wider and more

irregular than the electromagnetic shower.

The different shower shapes can be used to distinguish between electrons and protons (antiprotons). Combined with the tracker measurement ( $E/|R|$  cut), the ECAL provides a proton rejection power larger than  $10^4$  at an electron efficiency of 90% in the energy range of 3 to 1000 GeV. In figure 3.16(a), the proton rejection of the ECAL is shown.

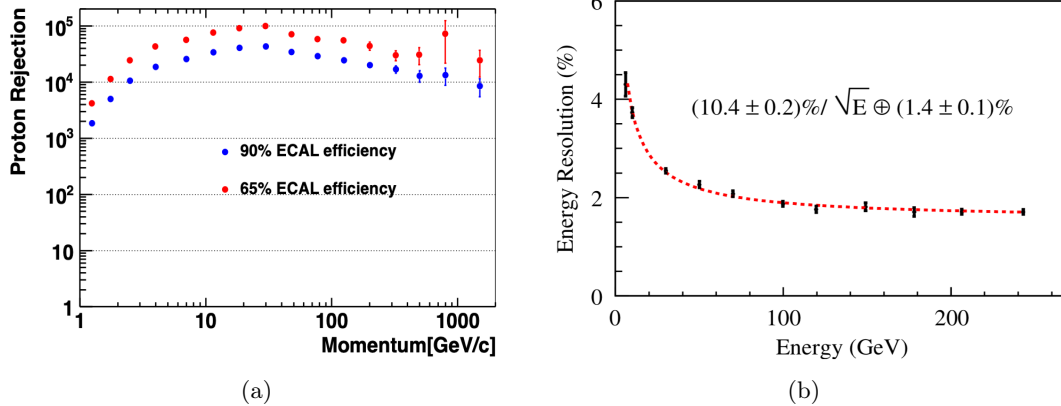


Figure 3.16: a) The proton rejection of the ECAL at 65% and 90% electron efficiency [81] . b) The ECAL energy resolution determined from test beam data. The function of equation 3.3 is also shown (red dashed line) [105] .

The energy resolution has been determined in a CERN test beam [106] and can be described by [105] :

$$\frac{\sigma(E)}{E} = \frac{(10.4 \pm 0.2)\%}{\sqrt{E(\text{GeV})}} \oplus (1.4 \pm 0.1)\% \quad (3.3)$$

Figure 3.16(b) shows the ECAL energy resolution measured in the test beam.

### 3.7. Anti-Coincidence Counter

The ACC in the AMS-02 experiment surrounds the inner tracker inside the magnet bore [107, 108] (figure 3.17(a)). Their purpose is to reject unwanted events with particles entering or leaving the inner tracker from the side. Moreover the ACC is used to reduce the trigger rate when the ISS is going through an area that is overwhelmingly dominant by low energy particle flux like the South Atlantic Anomaly (SAA) [109] .

The ACC has a cylinder shape of 1.1 m in diameter and 0.83 m in height. It is composed of 16 curved scintillator (Bicron BC-414) panels with 8 mm thickness, as shown in figure 3.17(b). When a particle traverses the ACC panels, it emits photons by ionization energy

loss in the scintillators. Then the light is absorbed by the wavelength shifting fibres (WLS, Kuraray Y-11(200)M) that are embedded into the panels, and is transported to the PMTs (Hamamatsu R5946) placed on both ends of the ACC structure.

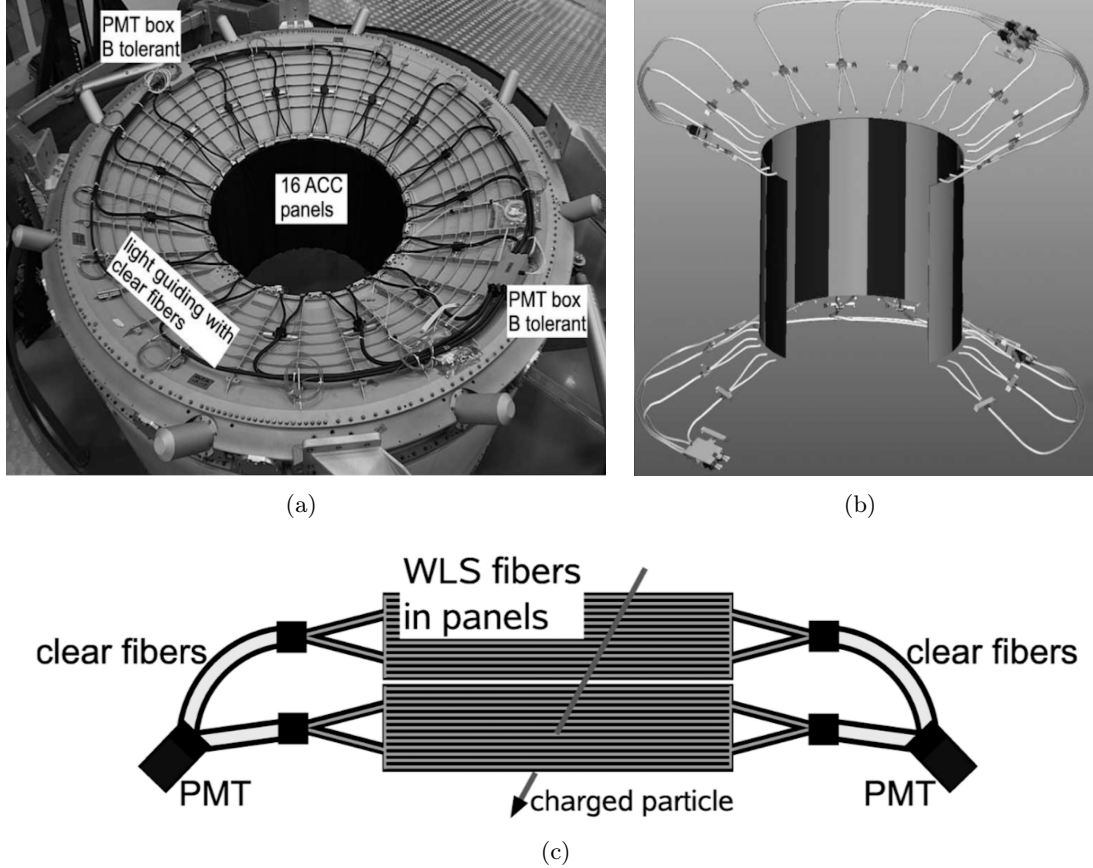


Figure 3.17: a) The ACC system. b) The arrangement of the ACC scintillator panels. c) A panel pair and its connections to the PMTs [110] .

A pair of panels is connected to two same PMTs through clear fibers, as shown in figure 3.17(c). This design provides redundancy capabilities and saves weight. The slot between these two panels has a tongue and a groove structure to minimize the detection inefficiency. The ACC panels efficiency has been measured at a muon test beam at CERN and found to be equal to 99.99% [81] .

The ACC signals are used in the trigger logic to veto events with particles crossing from the side of the detector. Combined with the information from the TOF, the trigger is generated [109] .

# CHAPTER 4

## ANALYSIS

In this chapter, the details of the antiproton analysis will be given, including all the steps of deriving the time-averaged and time-dependent antiproton to proton flux ratio. To determine the flux ratio, the definition of flux should be given first. In general, the flux as a function of true rigidity is calculated by:

$$\Phi(|R|_{\text{true}}) = \frac{N(|R|_{\text{true}})}{\Delta R \cdot T(|R|_{\text{true}}) \cdot A(|R|_{\text{true}}) \cdot \epsilon(|R|_{\text{true}})} \quad (4.1)$$

where  $N(|R|_{\text{true}})$  is the number of events in this rigidity bin,  $\Delta R$  is the rigidity bins width,  $T(|R|_{\text{true}})$  is the measuring time,  $\epsilon(|R|_{\text{true}})$  is the trigger efficiency and  $A(|R|_{\text{true}})$  is the effective acceptance. The quantities in equation 4.1 are as a function of true rigidity, while the number of events, derived from the template fit (a method to extract signal and background events from the total event distribution, see Section 4.4), is expressed as a function of reconstructed rigidity. To get the event number in true rigidity, a procedure called "unfolding" is performed. This will be discussed further in section 4.7.

In this thesis, the objective is the antiproton to proton flux ratio. Therefore, the dedicated formula should be determined based on the equation 4.1. Given the antiproton and proton flux definitions:

$$\begin{aligned} \Phi_{\bar{p}}(|R|_{\text{true}}) &= \frac{N_{\bar{p}}(|R|_{\text{true}})}{\Delta R_{\bar{p}} \cdot T_{\bar{p}}(|R|_{\text{true}}) \cdot A_{\bar{p}}(|R|_{\text{true}}) \cdot \epsilon_{\bar{p}}(|R|_{\text{true}})} \\ \Phi_p(|R|_{\text{true}}) &= \frac{N_p(|R|_{\text{true}})}{\Delta R_p \cdot T_p(|R|_{\text{true}}) \cdot A_p(|R|_{\text{true}}) \cdot \epsilon_p(|R|_{\text{true}})} \end{aligned} \quad (4.2)$$

the antiproton to proton flux ratio is defined as the antiproton flux divided by the proton flux. In this process, some terms can be strictly canceled out, like in the AMS-02 positron to electron flux ratio analysis [111]. Therefore, the overall calculation can be simplified:

$$\begin{aligned}
\frac{\Phi_{\bar{p}}(|R|_{\text{true}})}{\Phi_p(|R|_{\text{true}})} &= \frac{N_{\bar{p}}(|R|_{\text{true}}) \cdot \Delta R_{\bar{p}} \cdot T_{\bar{p}}(|R|_{\text{true}}) \cdot A_p(|R|_{\text{true}}) \cdot \epsilon_p(|R|_{\text{true}})}{N_p(|R|_{\text{true}}) \cdot \Delta R_{\bar{p}} \cdot T_{\bar{p}}(|R|_{\text{true}}) \cdot A_{\bar{p}}(|R|_{\text{true}}) \cdot \epsilon_{\bar{p}}(|R|_{\text{true}})} \\
&= \frac{N_{\bar{p}}(|R|_{\text{true}}) \cdot A_p(|R|_{\text{true}})}{N_p(|R|_{\text{true}}) \cdot A_{\bar{p}}(|R|_{\text{true}})} \\
&= \frac{N_{\bar{p}}(|R|_{\text{true}}) \cdot A_p^{\text{MC}}(|R|_{\text{true}}) \cdot (1 + \delta_p(|R|_{\text{true}}))}{N_p(|R|_{\text{true}}) \cdot A_p^{\text{MC}}(|R|_{\text{true}}) \cdot (1 + \delta_{\bar{p}}(|R|_{\text{true}}))} \\
&= \frac{N_{\bar{p}}(|R|_{\text{true}}) \cdot A_p^{\text{MC}}(|R|_{\text{true}})}{N_p(|R|_{\text{true}}) \cdot A_{\bar{p}}^{\text{MC}}(|R|_{\text{true}})}
\end{aligned} \tag{4.3}$$

where  $A_p^{\text{MC}}(|R|_{\text{true}})$  and  $A_{\bar{p}}^{\text{MC}}(|R|_{\text{true}})$  are the effective acceptances of proton and antiproton taken from the MC,  $\delta_p(|R|_{\text{true}})$  and  $\delta_{\bar{p}}(|R|_{\text{true}})$  are the data/MC corrections of the proton and antiproton effective acceptances, more details about these will be given in section 4.5. As shown in equation 4.3 the terms that cancel out in the antiproton to proton flux ratio are the rigidity bin width  $\Delta R$ , the measuring time  $T(|R|_{\text{true}})$ , the trigger efficiency  $\epsilon(|R|_{\text{true}})$  and the data/MC corrections of the effective acceptance  $(1 + \delta(|R|_{\text{true}}))$ . The details of these terms will be shown in detail in the following sections. These cancellations simplify the calculation of the antiproton to proton flux ratio.

For the time-dependent antiproton to proton flux ratio calculation, the formula in time bin  $i$  is given in Equation 4.4, which is similar to the time-averaged one. The difference is that the number of events is obtained from the individual template fits in every six Bartels Rotation time bin.

$$\begin{aligned}
\frac{\Phi_{\bar{p},i}(|R|_{\text{true}})}{\Phi_{p,i}(|R|_{\text{true}})} &= \frac{N_{\bar{p},i}(|R|_{\text{true}}) \cdot \Delta R_{\bar{p},i} \cdot T_{\bar{p},i}(|R|_{\text{true}}) \cdot A_{p,i}(|R|_{\text{true}}) \cdot \epsilon_{p,i}(|R|_{\text{true}})}{N_{p,i}(|R|_{\text{true}}) \cdot \Delta R_{\bar{p},i} \cdot T_{\bar{p},i}(|R|_{\text{true}}) \cdot A_{\bar{p},i}(|R|_{\text{true}}) \cdot \epsilon_{\bar{p},i}(|R|_{\text{true}})} \\
&= \frac{N_{\bar{p},i}(|R|_{\text{true}}) \cdot A_{p,i}^{\text{MC}}(|R|_{\text{true}})}{N_{p,i}(|R|_{\text{true}}) \cdot A_{\bar{p},i}^{\text{MC}}(|R|_{\text{true}})}
\end{aligned} \tag{4.4}$$

In section 4.1, the cuts and selections are discussed. Section 4.2 shows the construction of the charge confusion estimator. Section 4.3 describes how the TRD likelihood estimator is constructed. In section 4.4, the template fit procedures to get the antiproton signals in different rigidity ranges are shown. Section 4.5 gives the details about how to calculate the effective acceptances of antiproton and proton. In section 4.6, the measuring time used in this analysis is determined. Although the measuring time is canceled in the antiproton to proton flux ratio calculation, it has to be calculated because the rigidity cutoff is not simulated in the MC simulation which is used for unfolding, also the measuring time in the time-dependent analysis is important to understand the event numbers change. Section 4.7 shows the unfolding procedure. In section 4.8, the antiproton to proton flux ratio is given with statistical uncertainty only. In section 4.9, the different systematic uncertainties in different rigidity ranges are discussed.

## 4.1. Data Selection

### 4.1.1. AMS-02 Data and Monte Carlo Simulation

This section provides information on the data used in this analysis and presents the complete list of cuts and selections. In this analysis, the AMS-02 experiment data has been collected from May 20th 2011 to May 3rd 2021. Collected raw data need some calibration and alignment work and then can be reconstructed via the AMS-02 official software (named gbatch), resulting in the analysis data stored in ROOT files. The ROOT data analysis format is developed at CERN and it is dedicated for High energy particle physics analysis [112]. Furthermore, a software package developed in Aachen called ACSoft is used to further process and store the data in a higher-level structure called ACQT [113]. The analysis in this thesis is based on the so-called pass7 version of data (reconstructed via gbatch in version B1130).

The rigidity binning used in this analysis is the same as the one used in the previous AMS-02 proton analysis [68], which is determined by the rigidity resolution. At the rigidity regions higher than 80.5 GV, the rigidity bins are merged in every two bins to increase antiproton statistics.

For the time-dependent analysis, the collected ISS data is divided into six Bartels Rotations time bins. A Bartels Rotation is exactly 27 days, close to the synodic rotation period of the Sun. Because of the rigidity cutoff, the statistics in the low rigidity range in each time interval is limited. Therefore, the rigidity bins are also merged in every two original time-averaged rigidity bins in time-dependent antiproton analysis. The data collection used in this thesis started in May 2011, which corresponds to the Bartels Rotation 2426, and ended in May 2021, at the Bartels Rotation 2561. In total, the data can be divided into 23 intervals of six Bartels Rotations each though the last time bin has less data than the full six Bartels Rotations.

Due to the upgrade of the cooling system of the AMS silicon tracker that took place from Nov 2019 to Jan 2020, the operation mode frequently changed during some periods as the cooling system pump had to be switched off. The data collected during these time periods is excluded and not used in this analysis.

To validate the sub-detector's performance and study the detector's operation, an extensive set of MC simulations has been produced by the AMS-02 collaboration with the help of the Geant4 framework [114, 115]. The Geant4 is a software toolkit that simulates the passage of particles through matter. The interactions of the cosmic ray particles with all the AMS-02 sub-detectors and their support structure can be studied with this toolkit. By comparing the data distributions for different variables between MC and ISS data, the sub-detector's response to different cosmic rays can be systematically studied.

In this thesis, the used MC datasets are:

- B1042 Protons MC with generated momentum from 20 to 16000 GeV
- B1042 Protons MC with generated momentum from 1 to 800 GeV
- B1042 Antiprotons MC with generated momentum from 1 to 800 GeV
- B1220 Antiprotons MC with generated momentum from 0.2 to 1000 GeV
- B1091 Electrons MC with generated momentum from 0.25 to 200 GeV
- B1091 Electrons MC with generated momentum from 200 to 2000 GeV

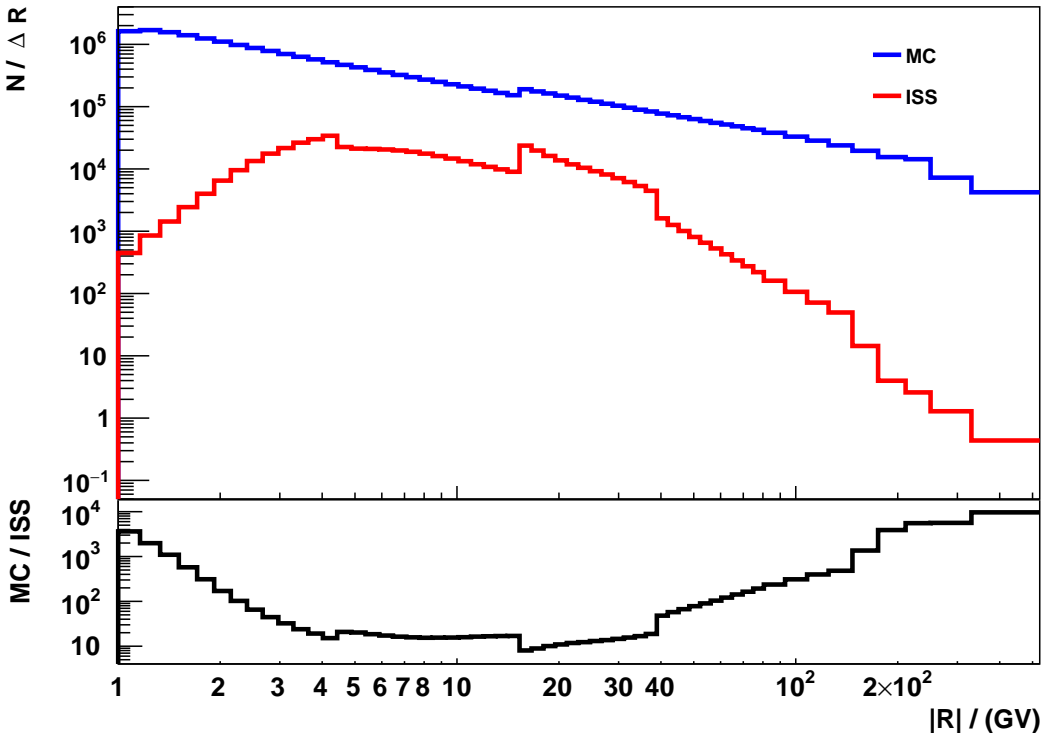


Figure 4.1: The statistics comparison between antiproton numbers from MC simulation and antiproton events from ISS data. The jumps in the ISS data are due to the different selections in different rigidity ranges. The statistics of antiproton MC is at least ten times larger than the antiproton events from ISS data.

In figure 4.1, the statistics of antiproton MC simulation and the antiproton events from the ISS data (which will be given in the following sections) are shown. The antiproton MC statistics is at least ten times larger than the antiproton events determined from the ISS data.

Different MC datasets are generated in different momentum ranges for various purposes. For example, one of the main purposes of using MC proton data in this analysis is to study

the proton charge confusion events, which are proton events but measured with the wrong rigidity sign. The reasons are finite tracker rigidity resolution and the interactions with the sub-detectors [92]. By selecting the negative rigidity data samples from the proton MC dataset, the proton charge confusion events can be studied. This issue will be discussed in more detail in Section 4.2. The MC datasets are also used for other purposes like calculating effective acceptance and determining the systematic uncertainties due to acceptance, these will be shown in detail later in this chapter.

For the simulated MC events, the generated momentum spectrum does not perfectly match the real cosmic spectrum. This could introduce bias in some variable distributions in MC. In order to correct this, the weight of each event in a MC dataset has to be reassigned by making the flux computed from this MC dataset equal to a reference flux. For example, the AMS-02 published proton flux result [68] is used as the reference flux for proton MC datasets. The acquired re-weighting factor will be used in filling variable histograms for further study.

Up to May 2021, the AMS-02 experiment has collected more than 174 billion cosmic ray events. To select antiproton events from them, cuts and event selections are applied. There are two levels of selection; the first one is the so-called “Preselection” and the second one is the more refined “Selection”. In the next few subsections, the definition of all selections and their pass ratios will be given. The pass ratio is the event number passed in this cut to the total event number before applying the selector (a group of cuts at this level of selection) to which this cut belongs.

#### 4.1.2. Preselection Cuts

The first level of cuts and selections is the preselection. The purpose is to discard data taken during bad sub-detectors operation conditions or have bad quality. These selections are general and applied before any cosmic ray component AMS-02 analyses. The preselection consists of two parts: data taking quality cuts and analysis data quality cuts. Each part is a selector.

Data taking quality cuts require all the sub-detectors running in nominal conditions, and the data taking conditions are normal. The first one excludes the period that any sub-detector operates under special conditions or undergoes testing. For example, the TRD gas refill procedure takes place once per month. In this period, the data taken is not included in this analysis. The second one requires that the data taking period is normal. For instance, if the ISS is in the SAA area, the data taken in this period is not included in this analysis. In summary, Table 4.1 shows the pass ratios of all the data taking quality cuts.

The data taking quality cuts ensure that the events selected were collected during normal operation time periods, but for analysis, further quality selections are needed to ensure the analysis based on these data is meaningful. The analysis data quality cuts are used to discard the bad quality collected data. In Table 4.2, the complete list of the analysis data

Table 4.1: List of data taking quality cuts and their pass ratios

Cuts	Description	Pass Ratio
<b>Bad Runs</b>	Remove the events collected when the sub-detector is in unstable condition, for example the TRD gas refill period or when the DAQ was unavailable.	99.73 %
<b>Second Within Run</b>	Remove the events collected without a run ID.	99.92 %
<b>Bad Reconstruction Period</b>	Remove the events collected in low reconstruction efficiency. The number of reconstructed events over the trigger rate should be nominal, otherwise the reconstruction efficiency is very low.	95.15 %
<b>Bad Facing Angle</b>	Remove the events collected when the zenith angle of the ISS is larger than $40^\circ$ .	99.78 %
<b>No Missed Events</b>	Remove the seconds if there are more than 10% events missing in this second. This situation could result from transferring problems in the DAQ boards or buffer overflows issues.	99.91 %
<b>Bad Live Time</b>	Remove the seconds when the live time fraction (see Section 4.6) $< 0.5$ .	95.67 %
<b>Too Many Events In Second</b>	Remove the seconds if it contains more than 1800 reconstructed events. The rejected events are mostly taken from the SAA area or near the pole regions.	97.86 %
<b>Good Alignment</b>	Remove the seconds when the external tracker planes are not in good alignment. The shifts of the external tracker planes to be corrected are estimated by different AMS-02 groups and they should be consistent.	99.86 %
<b>High TRD Occupancy Period</b>	Remove the seconds when the TRD occupancy is very high, namely the mean number of recorded TRD hits per second is larger than 1000.	97.80 %
<b>No Hardware Errors</b>	Remove the seconds when the hardware errors are detected, for example the bit-flips in the electronic boards.	99.91 %

quality cuts and their correspondent pass ratios are shown. The definitions of analysis data quality cuts are the following:

Table 4.2: List of analysis data quality cuts and their pass ratios

Cuts	Pass Ratio
<b>Particle is Downgoing</b>	59.84 %
<b>Has Hits in Central Inner Tracker</b>	70.16 %
<b>Has Single Tracker Track</b>	61.01 %
<b>Tracker Track Fit <math>\chi^2</math> in X</b>	97.33 %
<b>Tracker Track Fit <math>\chi^2</math> in Y</b>	90.64 %
<b>Has Hits in all four TOF Layers</b>	89.44 %

- The **Particle is Downgoing** is the cut on the particle's moving direction. By requiring that the TOF has  $\beta$  measurement and the TOF  $\beta$  to be positive, particles moving from the upper TOF to the lower TOF are selected. In this way, the particle's going direction from the top of the instrument to the bottom is achieved.
- The **Has Hits in Central Inner Tracker** requires hits in the tracker layers 3 or 4, 5 or 6, 7 or 8. To have an accurate rigidity measurement, the tracker hits inside the magnet are necessary. Therefore the central inner tracker should have enough hits for the rigidity measurement.
- The **Has Single Tracker Track** requires that for each event, only one reconstructed tracker track is found. To avoid multiple tracker tracks produced by interaction, this analysis only uses single tracker track events.
- The **Tracker Track Fit  $\chi^2$  in X** and **Tracker Track Fit  $\chi^2$  in Y** are the cuts that require the  $\chi^2/\text{ndf}$  of the tracker track fit to be less than 10 in both X and Y directions. To ensure the events used for analysis have good tracker track fit quality and subsequently correctly reconstructed rigidity, the cuts on  $\chi^2/\text{ndf}$  in the bending and unbending directions are mandatory.
- The **Has Hits in all four TOF Layers** requires that all the four TOF layers have hits. Since the TOF provides trigger and also the  $\beta$  measurement, hits on all four TOF layers give a precise response of the TOF.

#### 4.1.3. Selection Cuts

After the Preselection, a series of selection cuts relevant to the antiproton to proton ratio analysis are applied. These cuts are mainly used to select particles with charge equal to one (charge one particles) and ensure the good quality of the analysis events. The selection cuts and the pass ratios are presented in Table 4.3. There are three selectors in this table: Tracker

Charge, Upper and Lower TOF Charge, all the rest cuts in this table. The definitions of these cuts are the following:

Table 4.3: List of selection cuts and their pass ratios

Cuts	Pass Ratio
<b>Tracker Charge</b>	87.16%
<b>Upper TOF Charge</b>	97.46%
<b>Lower TOF Charge</b>	97.22%
<b>TRD Number Of Raw Hits</b>	98.89%
<b>TRD Active Layers</b>	90.71%
<b>Tracker Track In Trd Acceptance</b>	87.48%
<b>TRD TOF Track Match XY</b>	96.76%

- The **Tracker Charge** is the cut applied on the inner tracker charge  $Q_{\text{inner tracker}}$ . With the cut of  $0.7 < Q_{\text{inner tracker}} < 1.3$ , the charge one particle is selected from the tracker. The low rigidity analysis does not require any hits in the tracker layers L1 and L9. Therefore only the charge measurement in the inner tracker is guaranteed.
- The **Upper TOF Charge** is the cut on the upper TOF charge  $Q_{\text{UppTOF}}$ :  $0 < Q_{\text{UppTOF}} < 1.5$ . The lower value is 0, which cuts away the badly charge reconstructed events, and the higher value is 1.5, which cuts away events with charge 2 or higher.
- The **Lower TOF Charge** is the cut on the lower TOF charge  $Q_{\text{LowTOF}}$ :  $0 < Q_{\text{LowTOF}} < 2$ . The lower limit is 0 and the higher limit is 2. Due to the possible interaction between the two TOF layers, the cut value on the lower TOF is wider than on the upper TOF. In figure 4.2, the lower TOF charge distributions for ISS positive rigidity data and Proton MC in the rigidity bin of 0.7 to 18 GV are shown with the applied cut value.
- The **TRD Number Of Raw Hits** is the cut on the TRD Number Of Raw Hits  $N_{\text{TRD raw hits}}$ :  $8 < N_{\text{TRD raw hits}} < 1000$ . To ensure a good reconstruction of TRD variables, cuts on the minimum number of TRD raw hits are necessary.
- The **TRD Active Layers** is the cut on the TRD Active Layers  $N_{\text{TRD active layers}}$ :  $14 < N_{\text{TRD active layers}} < 20$ . To ensure a good TRD measurement of the event and construct the TRD Likelihood  $\Lambda_{\text{TRD}}$  (see Section 4.3) precisely, a minimum of TRD active layers is required.
- The **Tracker Track In Trd Acceptance** requires that the tracker track of the event is inside the TRD's geometrical acceptance. Therefore, the number of events with tracker tracks entering the detector from its side or are produced from interactions within the detector material can be reduced.

- The **TRD TOF Track Match XY** requires that the TRD track match the TOF track in X and Y directions. This ensures that the TRD track and TOF track are consistent with each other and a clean traverse path is obtained.

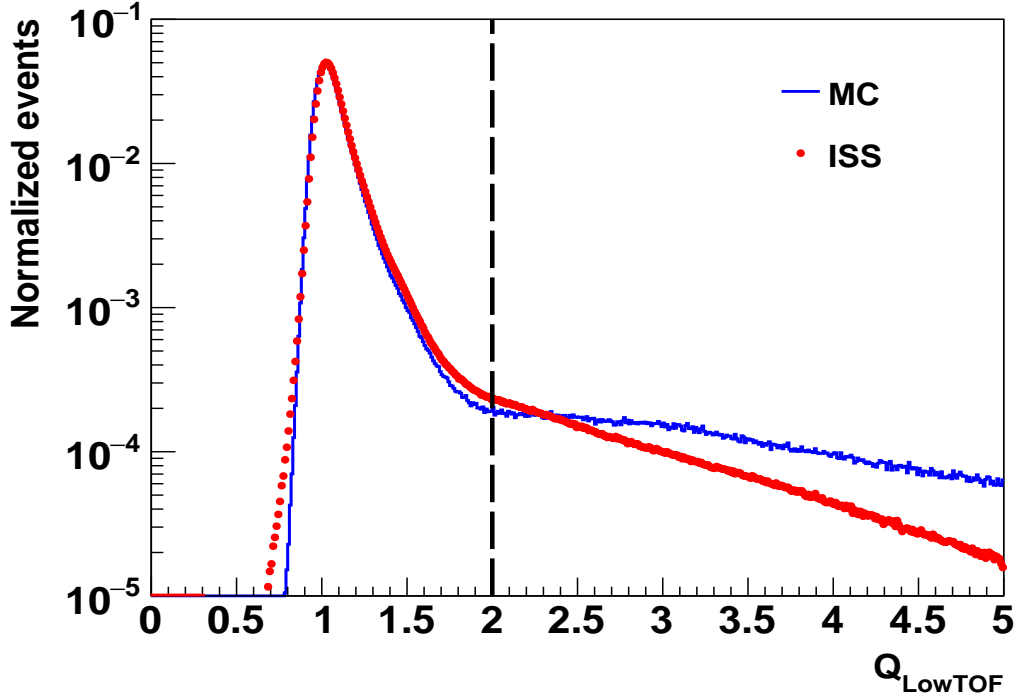


Figure 4.2: Comparison of the lower TOF charge distributions for ISS positive rigidity data and proton MC in the rigidity bin of 0.7 to 18 GV. The vertical black dashed line denotes the cut value. Higher charge events are removed after the cut. There are some differences between the tails of the distributions of data and MC, but this have no impact on the analysis since the templates in the low and intermediate rigidity range are taken from data directly (see Section 4.4).

## 4.2. Charge Confusion Estimator

"Charge Confused Protons" is defined as protons that are misconstrued with opposite rigidity signs. The first reason for it is the finite rigidity resolution. In figure 3.10, the AMS-02 tracker resolution is shown. With the resolution getting worse, the more likely rigidity sign to be constructed wrongly. The second reason is the interactions with the AMS sub-detectors: the particle scattering can produce kinks in the trajectory and spurious hits close to the particle track, which confuse the tracker fit and result in an opposite rigidity sign. The charge confused protons can mimic the behavior of charge correct antiprotons. Therefore,

the charge confused protons can go into the antiproton signal ranges when determining the antiprotons. With the rigidity going up, the number of events of wrongly reconstructed protons increases dramatically. In the high rigidity range, the largest background for the antiproton signal is the charge confused protons.

To solve this problem, the machine learning technique is used. The separation of antiproton signals and charge confused protons depends on the sign of rigidity. Since there are only two possible categories: positive rigidity and negative rigidity, the case falls into a binary classification. After checking the data/MC matching, the proton MC simulation data can be used in this learning process. Therefore, it is a supervised binary classification process.

To train the charge confusion classifier estimator, variables containing relevant information should be used. In this analysis, 16 variables from the sub-detectors are used for training. Most variables are from the tracker, and the others are from the TOF and the TRD. These variables are constructed by summarising the characteristics of charge confused proton events and have also been used in previous AMS-02 antiproton analyses [57] .

The training samples are taken from proton MC simulation. By selecting the negative rigidity events from proton MC data in the absolute rigidity range above 14 GV, the charge confused protons can be obtained. Below 14 GV the dominant background is secondary interactions and the contribution of charge confused proton is small. Since the antiproton and proton have only different charges, the antiproton's behavior in sub-detectors is assumed to be the same as the proton's, but only the rigidity sign is opposite. The charge correct antiproton samples can be replaced by charge correct proton samples but with opposite rigidity signs.

In figure 4.3, the four most important variables and their responses are given as examples to illustrate the information provided in order to separate the charge correct signal and the charge confused background. The importance of variables is identified by TMVA [116] during training. In the appendix, the complete list of the rest 12 variables and their definitions are shown.

The definitions of the four variables are given here:

1  $\Gamma_{\mathbf{L1L9}} = 100 \cdot \left( \frac{1}{R_{\text{Inner+L1}}} - \frac{1}{R_{\text{Inner+L9}}} \right) \cdot \frac{R}{|R|}$ .  $R_{\text{Inner+L1}}$  is the rigidity reconstructed using only the hits in the inner tracker layers and tracker layer 1.  $R_{\text{Inner+L9}}$  is the rigidity reconstructed using only the hits in the inner tracker layers and tracker layer 9.  $R$  is the rigidity reconstructed with the hits in all the tracker layers.

2  $\delta_R = \frac{R_{\text{Inner+L1}} - R_{\text{Inner+L9}}}{R_{\text{Inner+L1}} + R_{\text{Inner+L9}}}$ .  $R_{\text{Inner+L1}}$ ,  $R_{\text{Inner+L9}}$  and  $R$  have been defined in previous item.

3  $\delta_{\chi^2_y} = \frac{\chi^2_{y_{\text{Inner}}} - \chi^2_y}{\chi^2_{y_{\text{Inner}}} + \chi^2_y}$ . The  $\chi^2_{y_{\text{Inner}}}$  is the  $\chi^2$  of the Y side tracker track fitting only from the inner tracker layers. The  $\chi^2_y$  is the  $\chi^2$  of the Y side tracker track fitting from all the tracker layers.

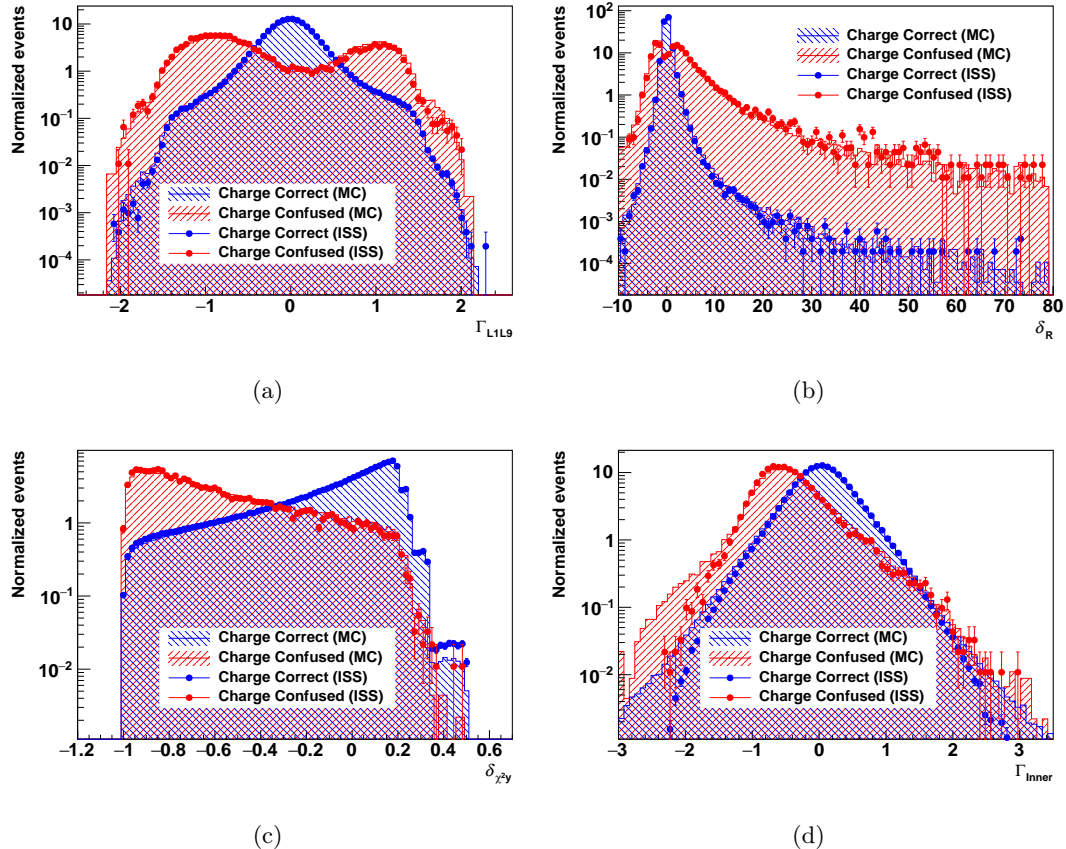


Figure 4.3: Four most important input variables used for training  $\Lambda_{CC}$ : a)  $\Gamma_{L1L9}$  b)  $\delta_R$  c)  $\delta_{\chi^2 y}$  d)  $\Gamma_{Inner}$  in the reconstructed rigidity bin of 330 to 525 GV in fullspan tracker pattern. The histograms are taken from proton MC simulation, the points are taken from ISS data. Charge correct samples are obtained by selecting positive rigidity. Since in this rigidity range, the ISS negative rigidity data is overwhelmingly dominant by charge confused protons, charge confused sample can simply be obtained by selecting negative rigidity. The distribution for the charge correct antiprotons is shown in blue while the distribution for the charge confused protons in red. Slight difference between MC and ISS data is observed in  $\Gamma_{Inner}$ , but since the output shapes of the MVA match well as we can see later, this impact is small.

$$4 \quad \Gamma_{\text{Inner}} = 100 \cdot \left( \frac{1}{R_{\text{Inner}}} - \frac{1}{R} \right) \cdot \frac{R}{|R|}. \quad R_{\text{Inner}} \text{ is the rigidity reconstructed only with the hits in the inner tracker layers. } R \text{ has been already defined earlier.}$$

As we see in Figure 4.3, the data and MC have similar distributions. This is important for further steps. The estimator training process is based on MC data. In order to make sure the trained estimator is applicable to data, the distributions of MC and data have to match each other.

All the input variables contain information about the differences between the signal and background. From the figure, the differences between signal distribution and background distribution are easy to observe. Due to the particle interaction with the AMS detector, the produced kinks in certain layers may confuse the tracker fit and lead to different rigidity values from the different tracker fits, also the  $\chi^2/\text{ndf}$  is worse. These are the reasons for the differences in the figure. These differences are used for the further training process.

In the TMVA framework, there are different training methods provided, like Boosted Decision Tree (BDT), Support Vector Machine (SVM), Gradient Tree Boosting (GTB), or the Likelihood method. To achieve the best separation performance, all the methods have been tried to get the best separation power. In this analysis, the Boosted Decision Tree (BDT) is used as the default method since it provides the best separation between signal and background.

The proton MC data is divided into positive rigidity sign and negative rigidity sign parts with the same amount of events. Each part is divided into a training sample, a validation sample and a test sample with a ratio of 6:3:1. The training is done in the same rigidity binning as the one used for antiproton to proton flux ratio, but only above 14.1 GV, since charge confusion protons are only dominant in the high rigidity range. To avoid overtraining, the training process requires that the response to the training sample should be the same as the response to the validation sample.

After training, the *charge confusion estimator*  $\Lambda_{\text{CC}}$  is obtained. In figure 4.4, the separation between the charge correct antiproton signal and the charge confused proton background in an example rigidity bin of 259-330 GV can be seen. The peak at 1 indicates the charge correct events and the peak at 0 the charge confused events. By setting a cut on  $\Lambda_{\text{CC}}$ , the charge correct antiproton sample can be obtained. But in this way, a part of the antiproton signal will be lost and some background events will contaminate the signal. Therefore, a template fit method is required to obtain the signal numbers precisely. This will be shown in Section 4.4. In figure 4.5, the rejection power in this rigidity bin is shown. The rejection power is defined as the inverse ratio of charge confused events at different charge correct event efficiency ranges.

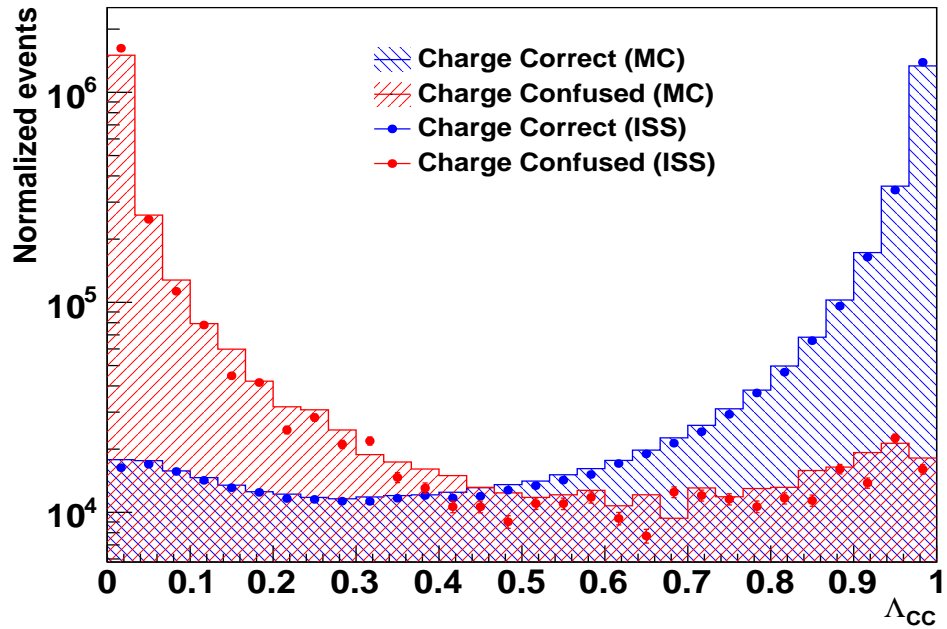


Figure 4.4: The charge confusion estimator  $\Lambda_{CC}$  for charge correct antiprotons (blue) and charge confused protons (red) in rigidity bin of 259 to 330 GV, histograms are taken from MC and points are taken from ISS data. MC and Data distributions match well.

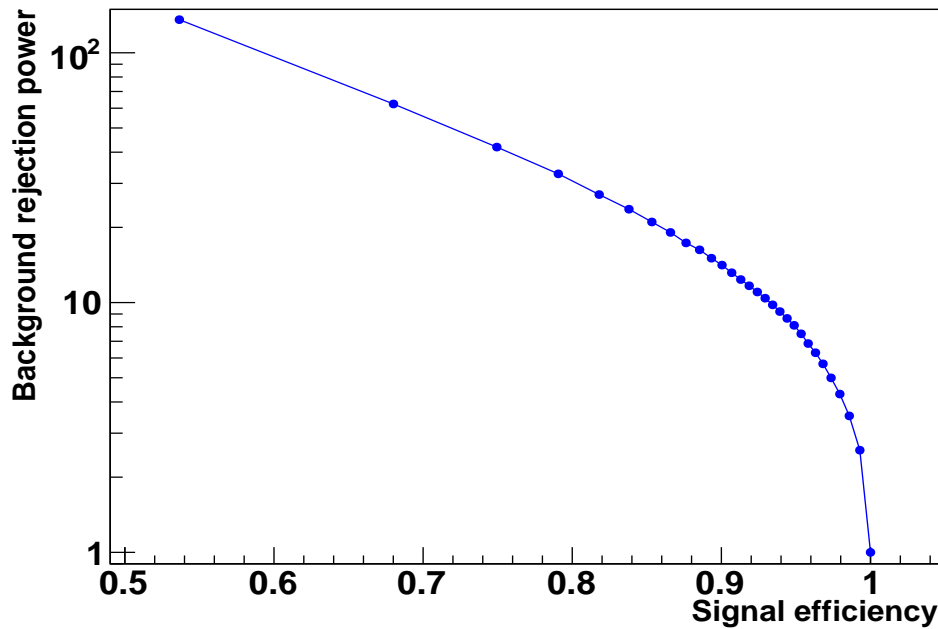


Figure 4.5: The background rejection power of charge confusion estimator  $\Lambda_{CC}$  in the rigidity bin of 259 to 330 GV.

### 4.3. TRD Estimator

Apart from charge confusion estimator  $\Lambda_{\text{CC}}$ , another estimator to be constructed before the antiproton signal determination is the TRD likelihood estimator  $\Lambda_{\text{TRD}}$ . The charge confusion estimator  $\Lambda_{\text{CC}}$  is constructed to identify charge confused proton background, while the TRD likelihood estimator  $\Lambda_{\text{TRD}}$  is constructed to separate light particle backgrounds like electrons from the signal.

As described in Section 3.2, the TRD sub-detector has the power to separate the heavy from the light particles. When the protons (antiprotons) pass through the tubes of the TRD, they lose energy which we can measure ( $dE/dX$  measurement). The electrons, due to their high Lorenz factor, emit transition radiation, which can be used to distinguish between electrons and protons (antiprotons).

According to the maximum likelihood method, the energy deposit distributions in the TRD are normalized and used as the probability distributions for each hit:  $p_k(E_{\text{dep}})$ . Then the information about all the layer hits, layer number, Xe partial pressure and pathlength inside the straw are combined to construct a likelihood  $\mathcal{L}$  for each particle species:

$$\mathcal{L} = \sqrt[n]{\sum_{k=1}^n p_k(E_{\text{dep}})} \quad (4.5)$$

For example, for electron and proton,  $\mathcal{L}_e$  and  $\mathcal{L}_p$  are constructed. According to Neyman-Pearson lemma [117], the separation power reaches its maximum in the form of the log-likelihood ratio. Therefore, the *TRD likelihood estimator*  $\Lambda_{\text{TRD}}$  is defined as:

$$\Lambda_{\text{TRD}} = -\log\left(\frac{\mathcal{L}_e}{\mathcal{L}_e + \mathcal{L}_p}\right) \quad (4.6)$$

the  $\Lambda_{\text{TRD}}$  provides separation power between electrons and protons. In figure 4.6, the  $\Lambda_{\text{TRD}}$  is shown in the example rigidity bin of 14.1 to 15.3 GV, the electrons and protons can be distinguished well. At the 90% electron efficiency range, the proton rejection power, which is defined as the inverse ratio of protons in this range, reaches more than  $10^4$  [118]. Similarly, the TRD likelihood estimator for the proton and the helium  $\Lambda_{\text{TRD}_{\text{P}/\text{He}}}$  is defined as  $-\log(\mathcal{L}_p/(\mathcal{L}_p + \mathcal{L}_{\text{He}}))$ .

### 4.4. Template Fit

In this section, the template fits are shown in detail for the time-averaged analysis and the time-dependent analysis. The template fit is a method to extract signal and background events from the total event distribution. If the data distribution is  $D(x)$  and it has  $k$  components, then the goal of the template fit is to extract the event number of different

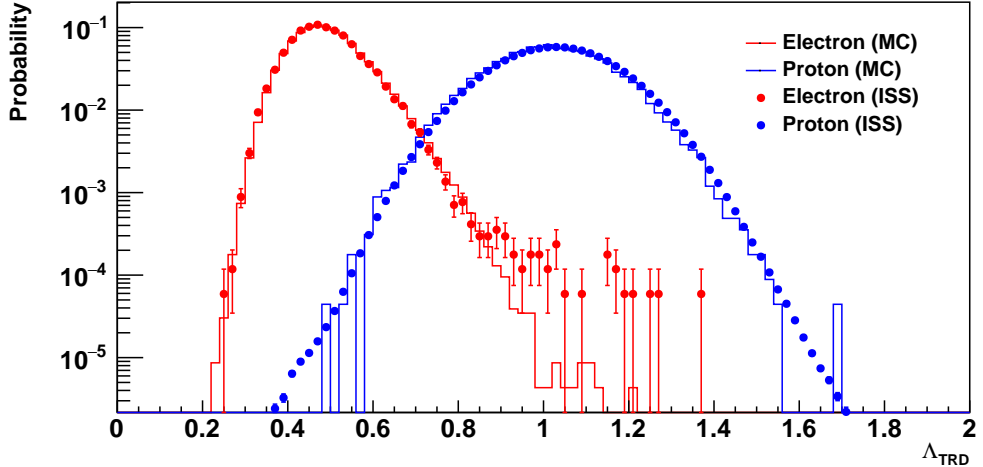


Figure 4.6: Separation between the electrons and protons in  $\Lambda_{\text{TRD}}$  in the rigidity bin of 14.1 to 15.3 GV. The electrons and protons can be separated well in  $\Lambda_{\text{TRD}}$ .

components from the data distribution. In this analysis, the binned maximum likelihood fit is used. The fit is performed by minimizing the negative log-likelihood function  $L$ :

$$L = - \left( \sum_x D(x) \cdot \log(P(x)) - N_{\text{total}} \right) \quad (4.7)$$

where  $N_{\text{total}}$  is the total number of event,  $P$  is the normalized likelihood, which is defined as the sum of the product of the number of events  $N_i$  and the PDF of the template  $P_i$ :

$$P(x) = \sum_{i=1}^k N_i \cdot P_i(x) \quad (4.8)$$

The minimization is achieved using the Minuit minimizer [119]. The PDFs of templates are constructed before the template fit and the numbers of events are free parameters. By minimizing the negative log-likelihood function, the best-fit parameters, namely the number of events for signals and backgrounds, can be extracted.

For different rigidity ranges, the template fit methods are different due to the sub-detector resolutions and background contributions. The selections used to obtain the signal and background templates will be discussed, and then the template fit result will be shown. In the time-dependent analysis, the template fit and the result in six Bartels Rotations will be given.

#### 4.4.1. Time-averaged analysis

The first ingredient to construct the antiproton to proton flux ratio is the number of events. As the background levels can not be ignored, cut-based analysis is not enough to get clean signals. Therefore, in order to extract clean antiproton signals, the template fit method is used in this analysis.

In different rigidity ranges, the detector resolutions and background components are different, and the whole analysis is divided into three parts: low rigidity range (1.0 GV to 6.5 GV), intermediate rigidity range (3.0 to 19.5 GV), and high rigidity range (14.1 to 525 GV). The rigidity ranges are the same with the ones used in the previous AMS-02 antiproton analysis [57]. In each range, a dedicated template fit method is used to get the antiproton signals, and the results in the overlappings from different template fit methods are used for crosschecks.

#### Low Rigidity Range

In the low rigidity range, the dominant background sources are light particles. Except the electrons, the interaction between the incoming particles with the AMS-02 materials can produce secondary interaction particles like pions. These background components have to be separated from the antiproton signals. Since the particle's mass is calculated from rigidity and  $\beta$  as given in equation 3.2, and the mass of the antiproton is much heavier than the background components in this range, the  $\beta$  measurements of antiproton signal is different from the backgrounds in a specific rigidity bin. In this rigidity range, the TOF can be used to separate antiprotons and backgrounds by measuring the  $\beta$ . With the rigidity going up, the separation power from  $\beta_{\text{TOF}}$  decreases, and at the same time, the TRD separation power increases, so the  $\Lambda_{\text{TRD}}$  can take over afterwards in the intermediate rigidity range. A 2D template fit in  $\Lambda_{\text{TRD}}$  and  $\beta_{\text{TOF}}$  ( $1/\beta_{\text{TOF}}$ ) is used in the low rigidity range to have a smooth and stable separation power. The range in low rigidity is from 1.0 GV to 6.5 GV. The lower limit is due to the low statistics after the geometrical cutoff, and the higher limit is due to the  $\beta_{\text{TOF}}$  resolution.

After the cuts and selections are applied, there are three major components in the data: antiprotons, electrons, and secondaries. The three templates must be constructed first to do the template fit. The antiproton template is taken from the ISS positive rigidity data since the clean proton data sample is easy to extract from it, and the rigidity sign does not impact the absolute value of the  $\beta_{\text{TOF}}$  and the  $\Lambda_{\text{TRD}}$ . The electron and the secondaries templates are taken from the ISS negative rigidity data. To get the clean electron and secondaries samples from it, dedicated selections are applied for each sample respectively. Furthermore, after the preselection and selection introduced in Section 4.1, the ISS data to be fitted should fulfill additional selection requirements in the low rigidity range. In table 4.4 the full list of selections is shown.

In table 4.4,  $\beta_{\text{RICH}}$  is the  $\beta$  measurement from the RICH,  $\beta(R, m) = \sqrt{\frac{R^2}{m^2 + R^2}}$  is the  $\beta$

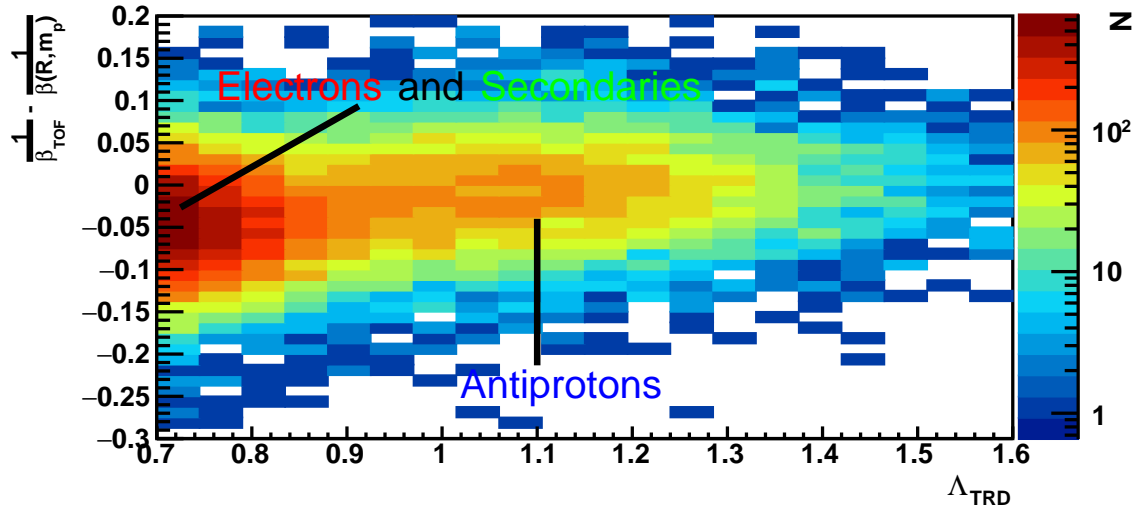
Table 4.4: List of selections to get all the templates and select further for the ISS data in the low rigidity range.

Antiproton Template	Electron Template
$\Lambda_{\text{TRD}_{\text{P}/\text{He}}} < 0.1$	Has $\beta$ measurement in RichAgl
TRD Number of tracks = 1	$ \beta_{\text{RICH}} - \beta(R, m_e)  < 0.002$
TRD Number of hits < 40	TRD Number of segments in XZ side = 1
$R > 0$	TRD Number of segments in YZ side = 1
	TRD Number of hits < 35
	$R < 0$
Secondaries Template	Further selections for ISS Data
Has $\beta$ measurement in RichAgl	$\Lambda_{\text{TRD}_{\text{P}/\text{He}}} < 0.1$
$ \beta_{\text{RICH}} - \beta(R, m_\pi)  < 0.002$	TRD Number of segments in XZ = 1
TRD Number of segments in XZ side > 1	TRD Number of segments in YZ = 1
TRD Number of segments in YZ side > 1	$R < 0$
TRD Number of hits > 50	
$R < 0$	

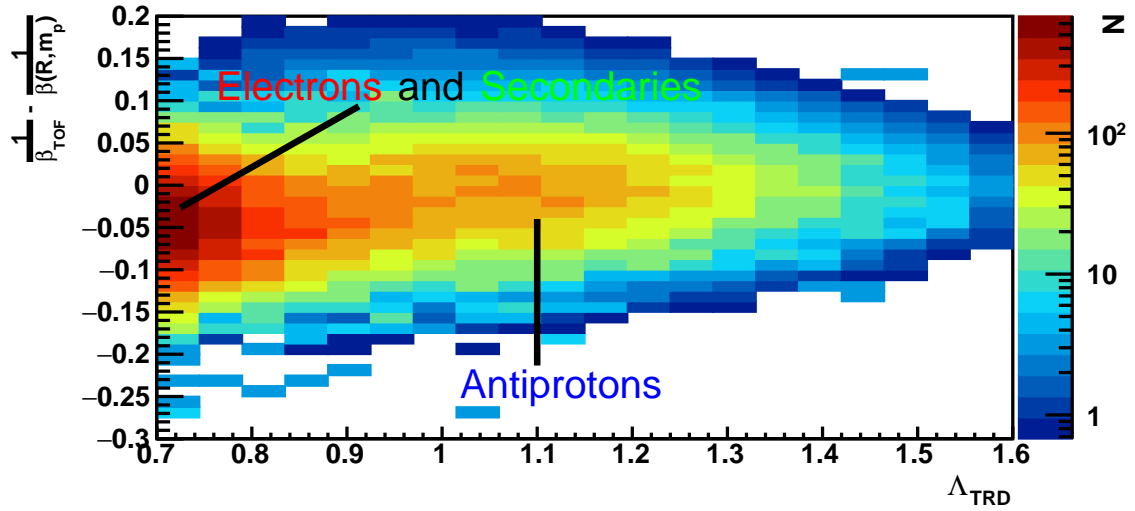
value constructed with rigidity  $R$  and mass  $m$ . Except for the cuts shown in the table, to remove most backgrounds before performing the template fit, additional template fit range cuts on  $\beta_{\text{TOF}}$  and  $\Lambda_{\text{TRD}}$  are applied to all the templates and ISS data to be fitted:  $\frac{1}{\beta_{\text{LowEdge}}(R)} < \frac{1}{\beta_{\text{TOF}}} - \frac{1}{\beta(R, m_p)} < 0.2$  and  $\Lambda_{\text{LowEdge}}(R) < \Lambda_{\text{TRD}} < 1.6$ .  $\beta_{\text{LowEdge}}(R)$  and  $\Lambda_{\text{LowEdge}}(R)$  denote the low edge of the template fit range. By varying the low edges, the systematic uncertainty of the template fit can be evaluated. This will be discussed further later in Section 4.9. For the final time-averaged antiproton to proton flux ratio, the template fit result at 90% signal efficiency is used.

In figure 4.7(a), the negative rigidity ISS data in the rigidity range of 2.97 to 3.29 GV is shown in  $1/\beta_{\text{TOF}}$  and  $\Lambda_{\text{TRD}}$  space. The three components are antiprotons, electrons and interaction secondaries.  $\Lambda_{\text{TRD}}$  cut of 0.7 is applied in this plot to remove the most backgrounds of electrons and interaction secondaries. In figure 4.7(b), an example template fit in this rigidity range is shown. To illustrate the separation, the 2D template fit is shown in two projections in figure 4.8. In  $1/\beta_{\text{TOF}}$  projection, further cut of  $\Lambda_{\text{TRD}} > 0.9$  is applied to reduce the backgrounds; similarly in  $\Lambda_{\text{TRD}}$  projection, further cut of  $1/\beta_{\text{TOF}} - 1/\beta(R, m_p) > 0.1$  is applied. Since it is a 2D template fit, the  $\chi^2/\text{ndf}$  is calculated individually in the two projections.

The template fits give the number of antiproton events in the low rigidity range. The proton number is obtained after selections introduced in Section 4.1 and further selections for ISS data in table 4.4 but  $R > 0$ . In figure 4.9 the number of antiproton and proton events as a function of the rigidity obtained is given.

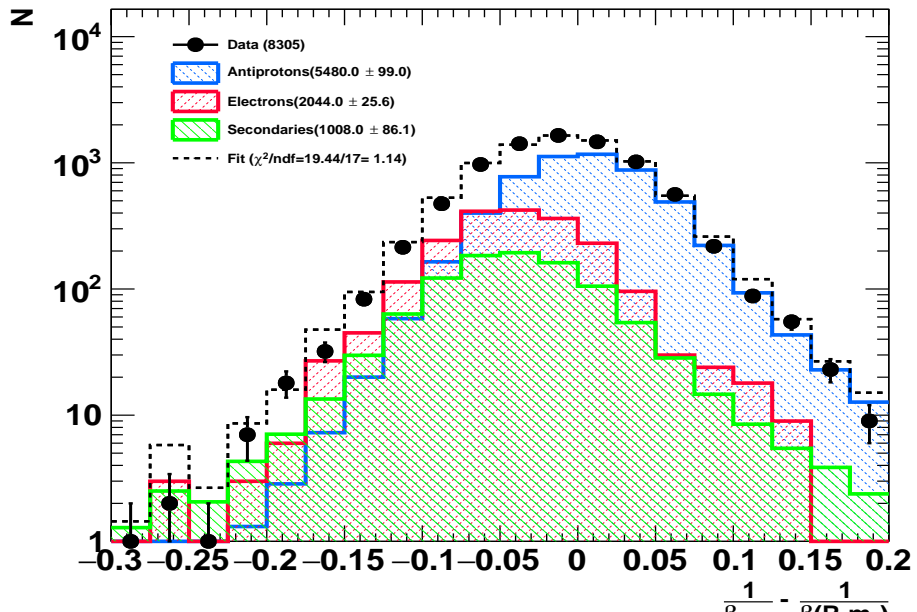


(a)

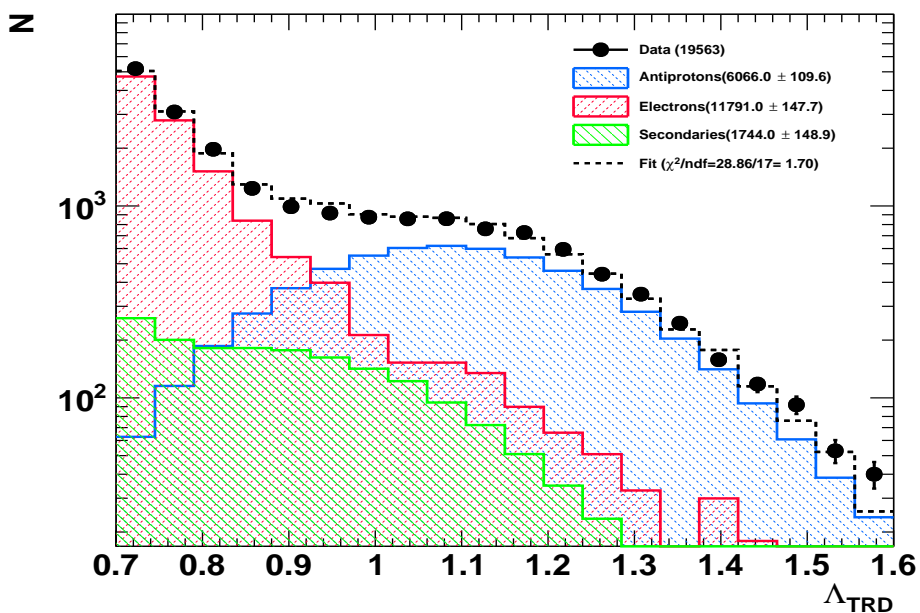


(b)

Figure 4.7: a) Negative rigidity ISS data in the rigidity range of 2.97 to 3.29 GV in  $1/\beta_{\text{TOF}}$  and  $\Lambda_{\text{TRD}}$  space. In the Y axis,  $1/\beta$  calculated with rigidity and antiproton mass is subtracted from the value of  $1/\beta_{\text{TOF}}$ , so the distribution of antiproton can be normalized to be around 0. Antiproton signal, electron and secondaries background components are seen in this plot. To remove the most backgrounds,  $\Lambda_{\text{TRD}}$  cut of 0.7 is applied in this plot. b) The 2D template fit result in the same rigidity bin of 2.97 to 3.29 GV in  $1/\beta_{\text{TOF}}$  and  $\Lambda_{\text{TRD}}$  space.



(a)



(b)

Figure 4.8: Example template fit in the low rigidity range of 2.97 to 3.29 GV. a)  $1/\beta_{\text{TOF}}$  projection. In this projection,  $1/\beta$  calculated with rigidity and antiproton mass is subtracted from the value of  $1/\beta_{\text{TOF}}$ . b)  $\Lambda_{\text{TRD}}$  projection.

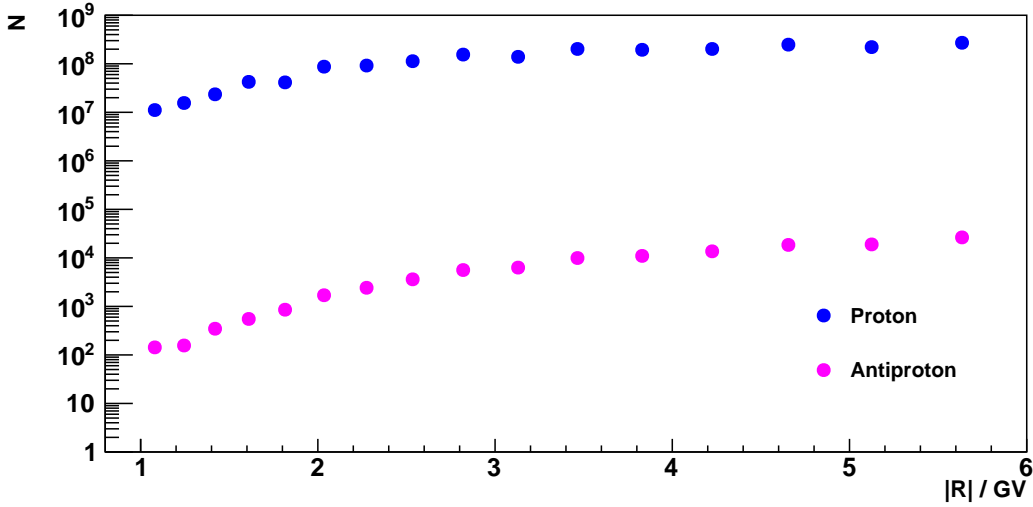


Figure 4.9: The numbers of antiproton and proton events as function of the rigidity obtained in the low rigidity range.

### Intermediate Rigidity Range

In the intermediate rigidity range, the 2D template fit in  $\beta_{TOF}$  and  $\Lambda_{TRD}$  is replaced by a 1D template fit in  $\Lambda_{TRD}$  since the separation power of  $\beta_{TOF}$  decreases with the rigidity going up and provides little power in this rigidity range. Above 20 GV, the component of charge confused protons gradually increases, so it has to be added as an additional template. Therefore the 1D template fit can only be implemented up to around 20 GV.

In the intermediate rigidity range, the interaction secondaries component is negligible. Therefore, the templates in this rigidity range are only formed for antiprotons and electrons. Like the template fit in the low rigidity range, the templates are also taken from the ISS data. The antiproton template is taken from positive rigidity data, and the electron template is taken from negative rigidity data. The dedicated selections for ISS data in the intermediate rigidity range are applied before the template fit. In table 4.5, the full list of selections that are used for the ISS data and in order to form the templates is given.

In table 4.5, the ECALBDT estimator is a value trained with ECAL response variables and can provide separation power between protons and electrons. If the particles go through the ECAL, a clean electron sample can be obtained by applying a cut of 0.5 on ECALBDT. To avoid the light particles background, if there is a  $\beta_{RICH}$  measurement then the value has to be less than  $\beta_{high}(R)$  to restrict the signal range. The  $\beta_{high}(R)$  is determined by 90% antiproton signal efficiency. Except for the cuts in this table, to remove most backgrounds before performing the template fit, an additional template fit range cut on  $\Lambda_{TRD}$  is applied to all the templates and ISS data to be fitted like described in the low rigidity range.

Table 4.5: List of selections to get all the templates and select further for the ISS data in the intermediate rigidity range.

Antiproton Template	Electron Template
$\beta_{\text{RICH}} < \beta_{\text{high}}(R)$	TRD Number of hits < 35
TRD Number of segments in XZ side = 1	ECALBDT > 0.5
TRD Number of segments in YZ side = 1	TRD Number of segments in XZ side = 1
$R > 0$	TRD Number of segments in YZ side = 1
	$R < 0$
<b>Further selections for ISS Data</b>	
$\beta_{\text{RICH}} < \beta_{\text{high}}(R)$	
TRD Number of segments in XZ side = 1	
TRD Number of segments in YZ side = 1	
$R < 0$	

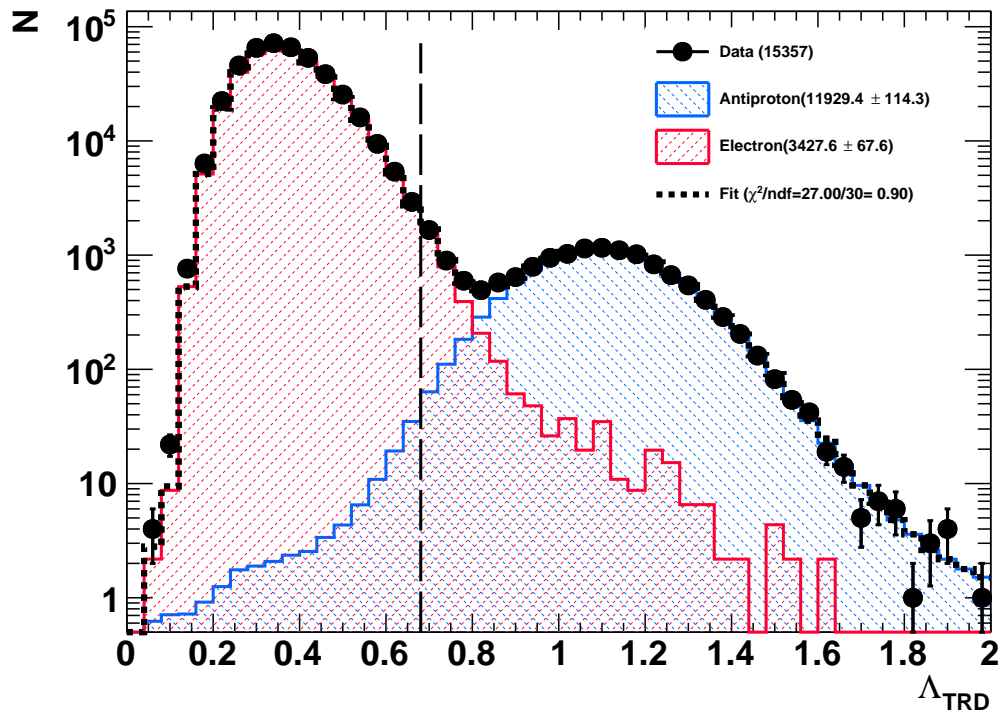


Figure 4.10: Example template fit in the intermediate rigidity range of 5.9 to 6.47 GV. To reduce the most electrons, the template fit is performed on the right side of the dashed line, which corresponds to around 99% antiproton signal efficiency.

In figure 4.10, an example template fit in the rigidity range of 5.9 to 6.47 GV is shown. The antiproton signal can be separated well from the electron background. To reduce the most background of electrons, the template fit range is set to around 99% antiproton signal efficiency (the dashed line).

The template fits give the number of antiproton events in the intermediate rigidity range. The proton number is obtained after selections introduced in Section 4.1 and further selections for ISS data in table 4.5 but  $R > 0$ . The obtained antiproton and proton numbers are shown in figure 4.11.

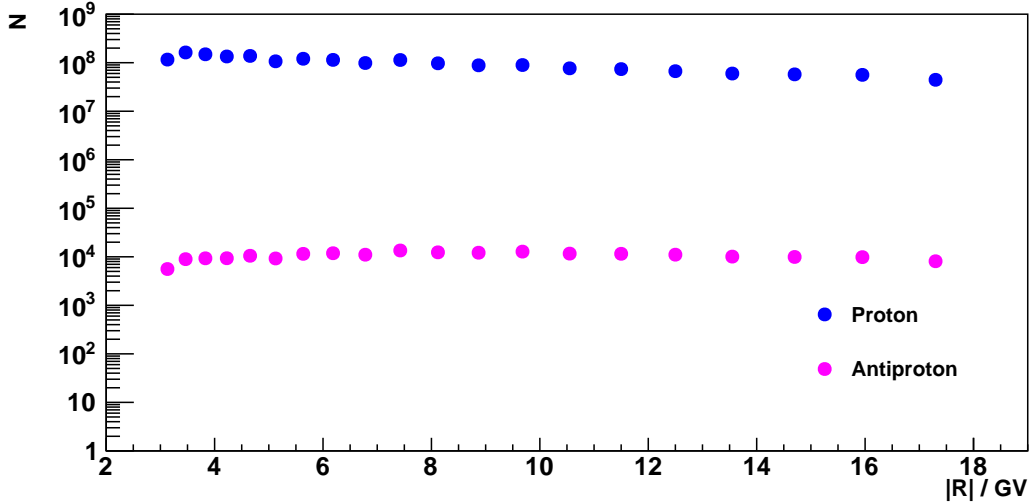


Figure 4.11: The numbers of antiproton and proton events as function of the rigidity obtained in the intermediate rigidity range.

### High Rigidity Range

In the high rigidity range, the contribution of charge confused protons increases. Therefore, the  $\Lambda_{\text{CC}}$  trained in Section 4.2 is used to separate antiprotons and charge confused protons. For electron separation, the TRD provides separation power, like in the low and intermediate rigidity ranges. In summary, a 2D template fit in  $\Lambda_{\text{CC}}$  and  $\Lambda_{\text{TRD}}$  is performed in this range to get the antiproton signal.

As shown in figure 3.10, different tracker patterns have different rigidity resolutions. To maximize the statistics and maintain the accuracy of rigidity measurement, the requirement of tracker patterns changes as rigidity goes up: No hit in tracker layers 1 and 9 is required below 38.9 GV; hit in either layer 1 and 9 is required from 38.9 to 147 GV; hit in layer 9 is required from 147 to 175 GV. Above 175 GV, hits in layers 1 and 9 are required. This selection requirement is the same as the one used in the previous AMS-02 publication [57]. From 80.5 GV, every two rigidity bins are merged to increase the statistics.

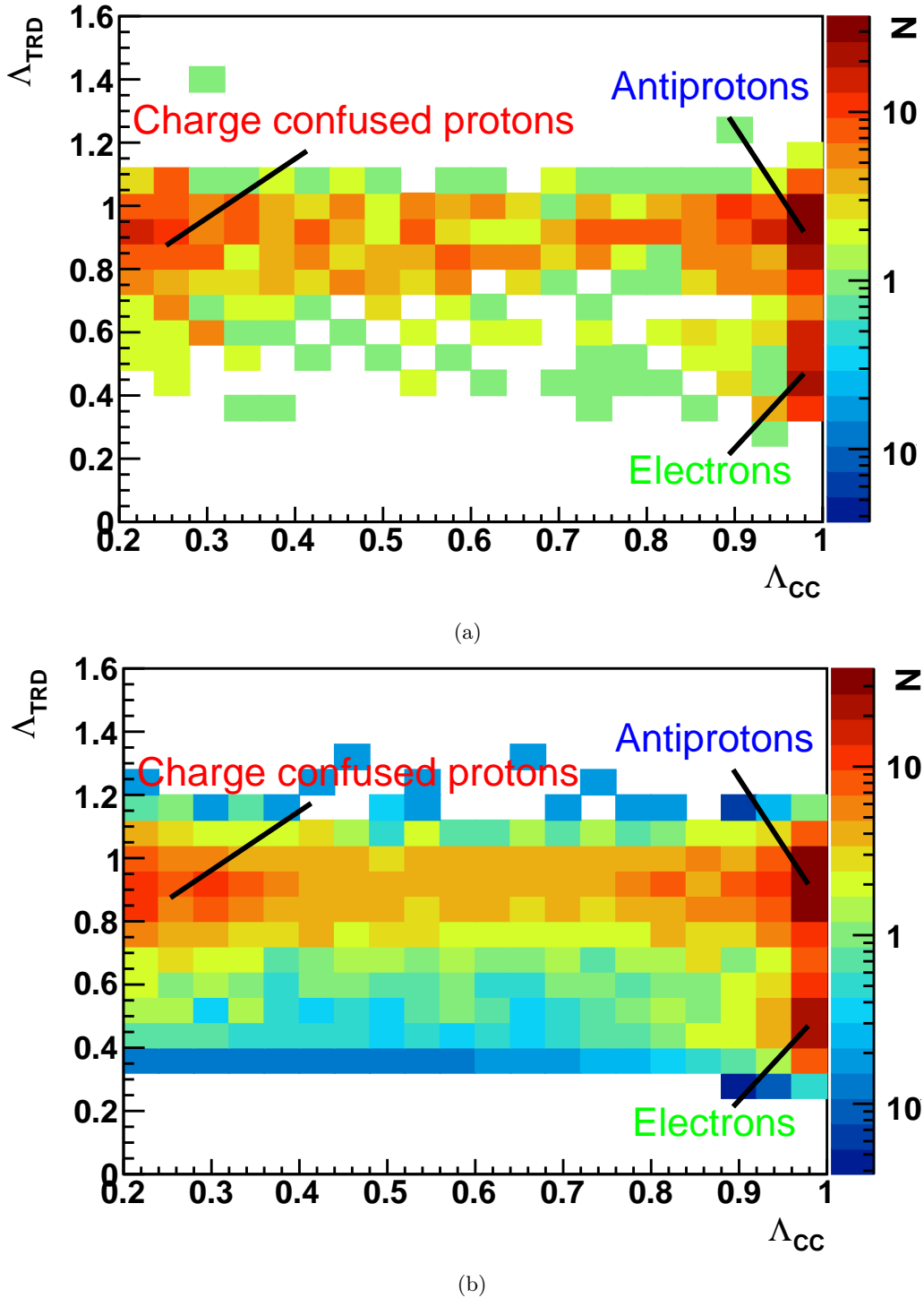
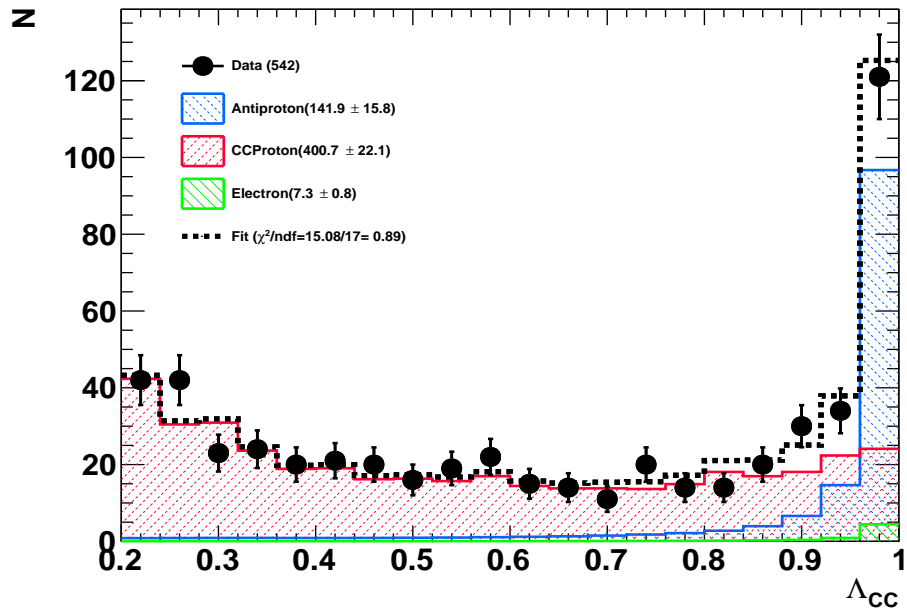
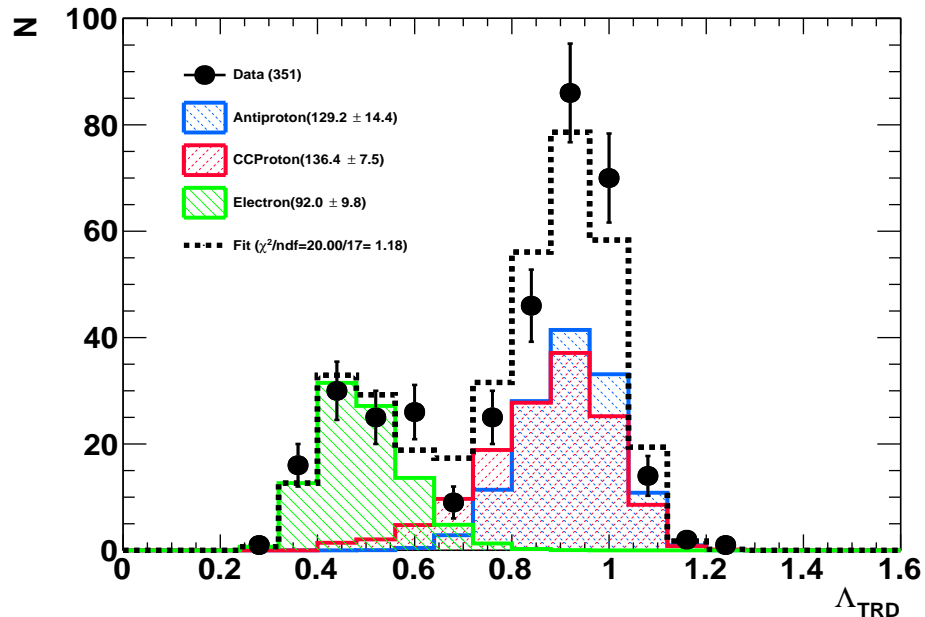


Figure 4.12: a) Negative rigidity ISS data in the rigidity range of 175 to 211 GV in  $\Lambda_{CC}$  and  $\Lambda_{TRD}$  space. Three components of antiprotons, electrons and charge confused protons are seen in this plot. To remove most backgrounds of charge confused protons,  $\Lambda_{CC}$  cut of 0.2 is applied. b) The 2D template fit result in the same rigidity bin of 175 to 211 GV in  $\Lambda_{CC}$  and  $\Lambda_{TRD}$  space.



(a)



(b)

Figure 4.13: Example template fit in the high rigidity range of 175 to 211 GV. a) In the  $\Lambda_{CC}$  projection,  $\Lambda_{TRD} > 0.7$  is applied and antiproton and charge confused proton can be separated well in this projection. b) In the  $\Lambda_{TRD}$  projection,  $\Lambda_{CC} > 0.75$  is applied and antiproton and electron can be separated well.

In the 2D template fit, the three templates are antiprotons, electrons, and charge confused protons. The antiproton template is taken from the ISS positive rigidity data, and the electron template is taken from the ISS negative rigidity data by ECALBDT. Finally, the charge confused proton template is formed by using proton MC simulation samples by selecting events with negative rigidity. To avoid the contamination of helium, the  $\Lambda_{\text{TRD}_{\text{P}/\text{He}}} < 0.3$  cut is applied for the negative rigidity data before the template fit.

To cut away the most background of charge confused protons, the template fit is performed in  $\Lambda_{\text{CC}} > 0.2$  range. In figure 4.12(a), the negative rigidity ISS data in the rigidity range of 175 to 211 GV is shown in  $\Lambda_{\text{CC}}$  and  $\Lambda_{\text{TRD}}$  space. The three components of antiprotons, electrons and charge confused protons are indicated in this figure. In figure 4.12(b), an example template fit in this rigidity range is shown. To illustrate the separation, the 2D template fit is shown in two projections in figure 4.13. In  $\Lambda_{\text{CC}}$  projection,  $\Lambda_{\text{TRD}} > 0.7$  is applied to show the separation between antiprotons and charge confused protons. In  $\Lambda_{\text{TRD}}$  projection,  $\Lambda_{\text{CC}} > 0.75$  is applied to show the separation between antiprotons and electrons. Since it is a 2D template fit, the  $\chi^2/\text{ndf}$  is calculated individually in the two projections.

The numbers of antiprotons and protons obtained in the high rigidity range are given in figure 4.14.

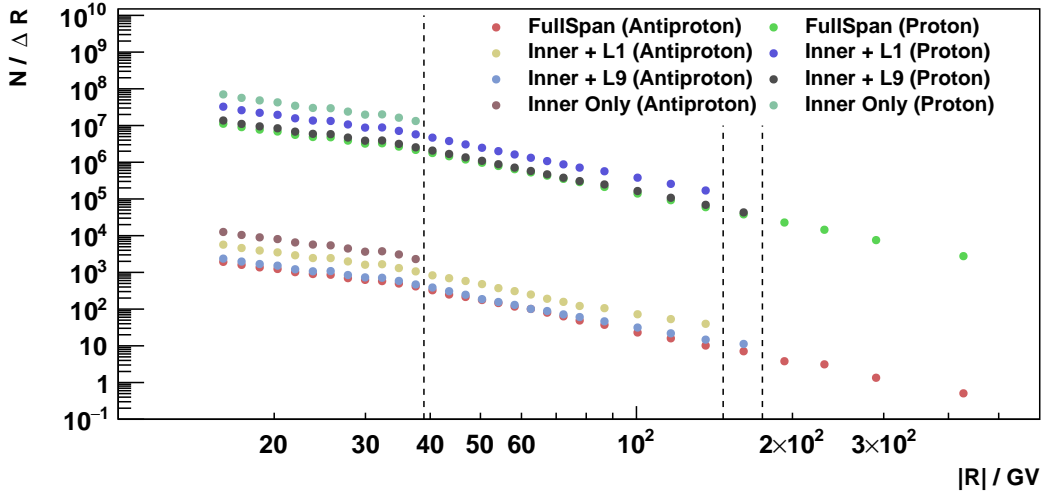


Figure 4.14: The antiproton and proton numbers obtained in the high rigidity range. The dashed vertical lines are the boundary of the usage of different tracker patterns. To avoid the jump due to the merge of rigidity bins from 80.5 GV, the antiproton and proton numbers are divided by the rigidity bin width to have a smooth curve.

Once the template fits in the three rigidity ranges are performed, the antiproton numbers from 1.0 to 525 GV can be obtained. In total, 481959 antiprotons are selected from the template fits.

#### 4.4.2. Time-dependent analysis

For the time-dependent analysis, the template fit strategy is the same as the one used in the time-averaged analysis. The data is divided into time bins with a width equal to the duration of six Bartels Rotations each. In each time bin, a template fit is performed to get the antiproton to proton ratio. Due to the limited statistics in each time bin, the rigidity binning is altered in the following way: every two original neighboring rigidity bins are now merged to form a new bin. In this way, an increase in statistics in each new bin is accomplished.

The template selections are the same as the ones used in the time-averaged analysis. The only difference is the template fit range. To increase the statistics, the signal efficiency is increased from 90% to 95% in the low rigidity range and from 90% to 98% in the intermediate rigidity range.

Since the templates are taken from the ISS data, the shapes of the templates are time-dependent. To visualize the time dependence, all the templates are parameterized in the distribution core range in the following way: In the  $\Lambda_{\text{TRD}}$  dimension, the antiproton, electron and secondaries are parameterized by a Novosibirsk function  $N(x; \mu, \sigma, \tau)$ , and in the  $1/\beta_{\text{TOF}}$  dimension, the antiproton, electron and secondaries are parameterized by a Gaussian function  $G(x; \mu, \sigma)$ :

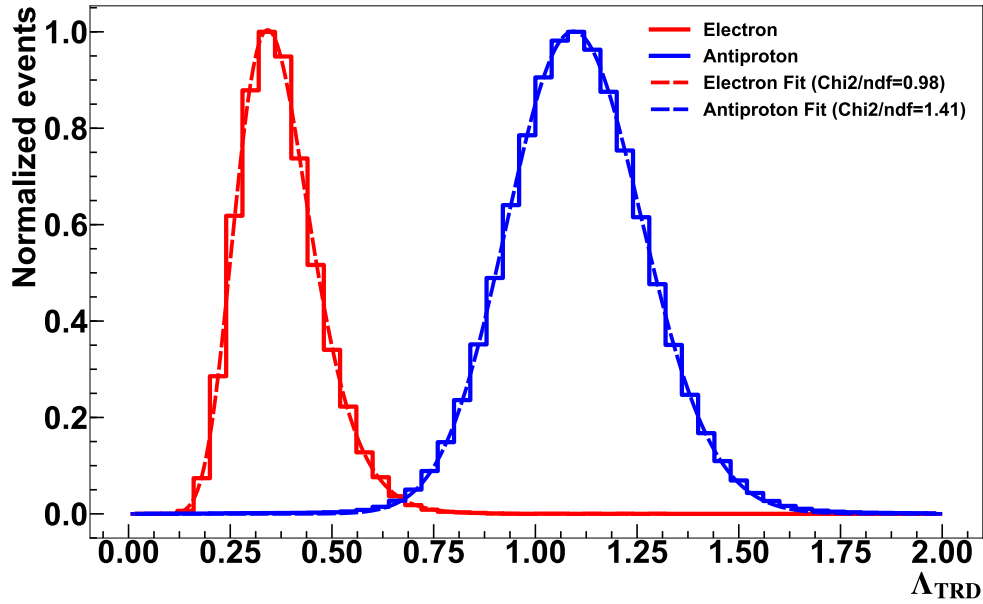


Figure 4.15: The parameterizations of the normalized antiproton and electron templates by Novosibirsk functions in the rigidity range of 6.47 to 7.76 GV with data collected from Feb.18.2017 to Jul.30.2017.

$$\begin{aligned}
G(x; \mu, \sigma) &= \frac{1}{\sqrt{2\pi}\sigma^2} \exp\left(-\frac{(x - \mu)^2}{2\sigma^2}\right), \\
N(x; \mu, \sigma, \tau) &= \exp\left(-\frac{1}{2} \left( \frac{(\ln(\lambda(x; \mu, \sigma, \tau)))^2}{\tau^2} + \tau^2 \right)\right), \text{ where} \\
\lambda(x; \mu, \sigma, \tau) &= 1 + \tau(x - \mu) \frac{\sinh(\tau\sqrt{\ln 4})}{\sigma\tau\sqrt{\ln 4}}
\end{aligned} \tag{4.9}$$

For an illustration of parameterization in the  $\Lambda_{\text{TRD}}$  dimension, the parameterizations of the normalized antiproton and electron templates in the rigidity range of 6.47 to 7.76 GV with data collected from Feb.18.2017 to Jul.30.2017 is shown as an example in figure 4.15.

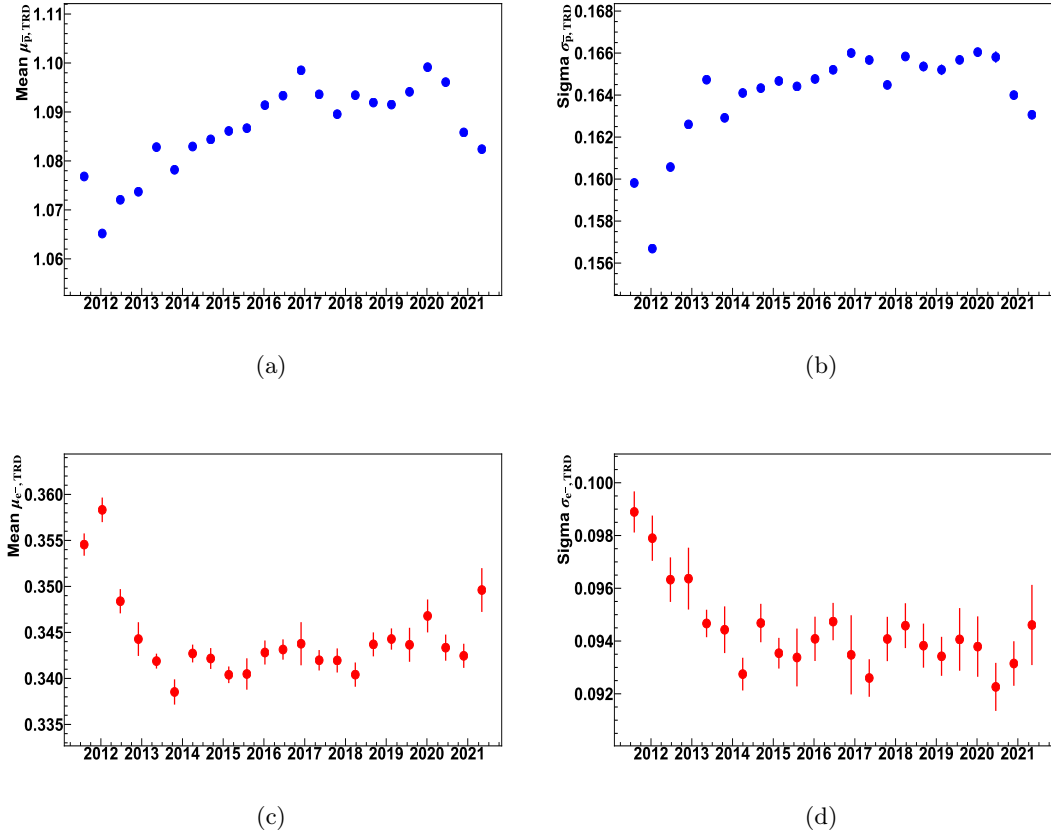


Figure 4.16: Time-dependence of the a)  $\mu_{\bar{p},\text{TRD}}$  b)  $\sigma_{\bar{p},\text{TRD}}$  c)  $\mu_{e^-,\text{TRD}}$  d)  $\sigma_{e^-,\text{TRD}}$  in the rigidity range of 6.47 to 7.76 GV. The parameters of the electron template show significant structures up to the end of 2012, where the TRD gas parameters were being optimized. After that, both parameters of antiproton and electron templates are changing due to the decrease of the Xe partial pressure in the TRD.

For the antiproton template, the time dependence can be described by the mean value

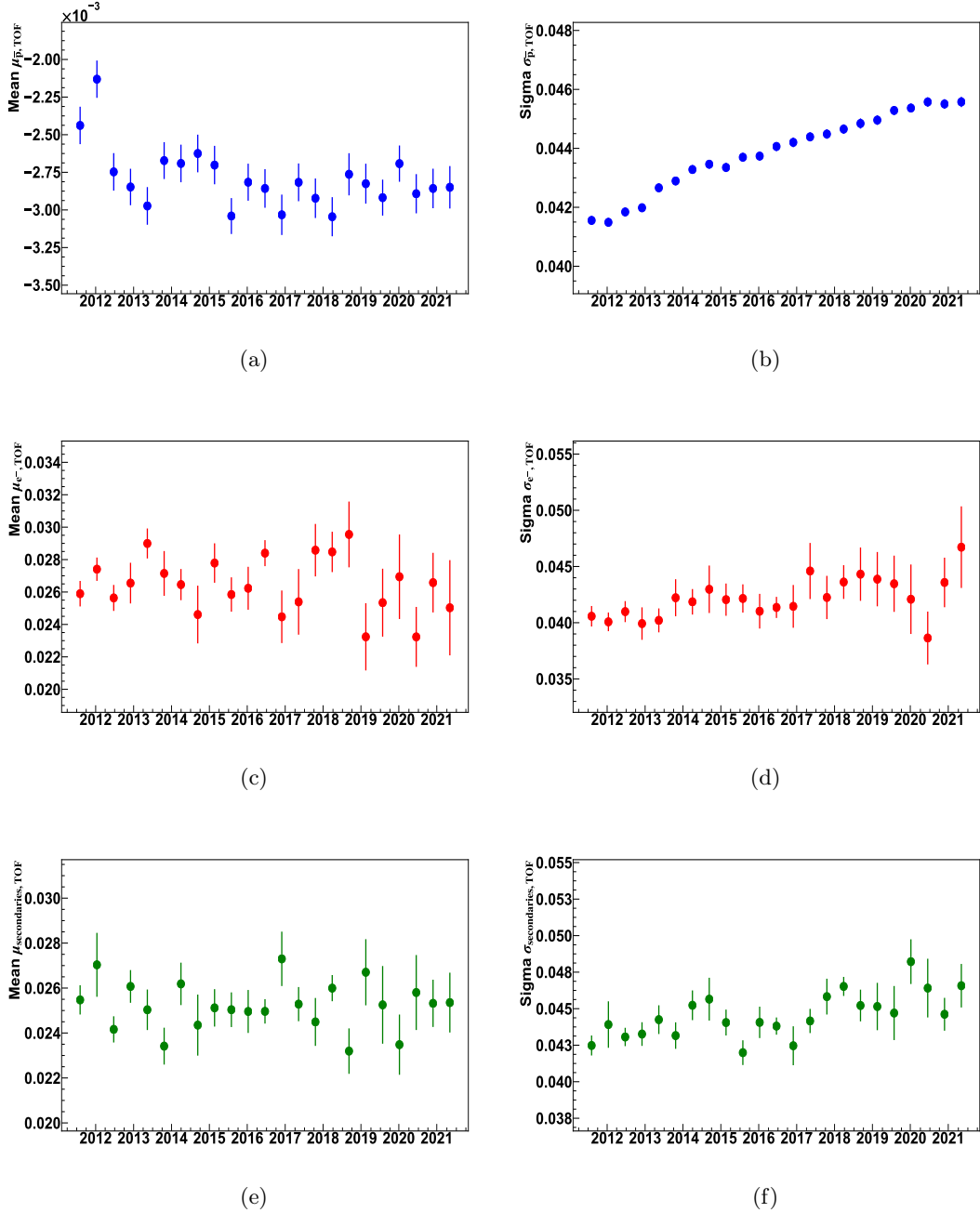


Figure 4.17: Time-dependence of the a)  $\mu_{\bar{p},\text{TOF}}$  b)  $\sigma_{\bar{p},\text{TOF}}$  c)  $\mu_{e^-, \text{TOF}}$  d)  $\sigma_{e^-, \text{TOF}}$  e)  $\mu_{\text{secondaries, TOF}}$  f)  $\sigma_{\text{secondaries, TOF}}$  in the rigidity range of 3.64 to 4.43 GV. No obvious trend is observed in the mean values but the distributions of sigma show rising trends in all three components, this could be due to the aging of the scintillators.

$\mu_{\bar{p},\text{TRD}}$  and width  $\sigma_{\bar{p},\text{TRD}}$ . For the electron template, the time dependence can be described by the mean value  $\mu_{e^-, \text{TRD}}$  and width  $\sigma_{e^-, \text{TRD}}$ . The time dependence of the four parameters in the rigidity range of 6.47 to 7.76 GV is shown in figure 4.16.

For the  $1/\beta_{\text{TOF}}$  dimension, the cores of the normalized antiproton, electron and secondaries templates are parametrized by Gaussian functions. The time dependence of the antiproton template can be described by the mean value  $\mu_{\bar{p},\text{TOF}}$  and width  $\sigma_{\bar{p},\text{TOF}}$ , the time dependence of the electron template can be described by the mean value  $\mu_{e^-, \text{TOF}}$  and width  $\sigma_{e^-, \text{TOF}}$ , the time dependence of the secondaries can be described by the mean value  $\mu_{\text{secondaries}, \text{TOF}}$  and width  $\sigma_{\text{secondaries}, \text{TOF}}$ . The six parameters in an example rigidity range of 3.64 to 4.43 GV are shown in figure 4.17.

An example template fit in the rigidity range of 6.47 to 7.76 GV is given in figure 4.18. The fitted data is six Bartels Rotations data taken from Feb.18.2017 to Jul.30.2017.

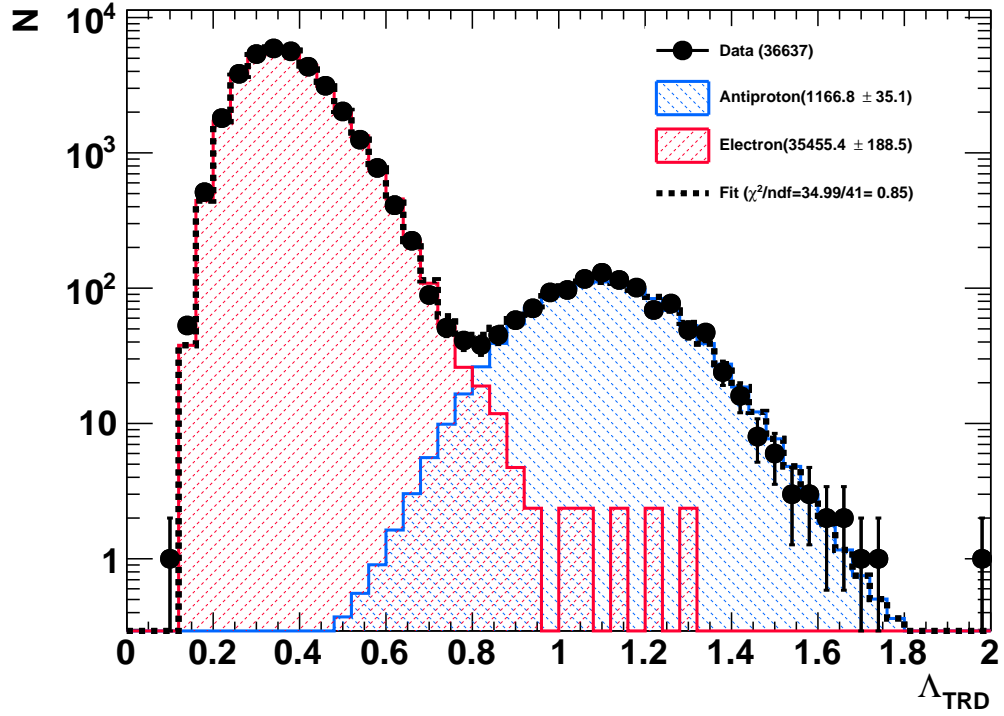


Figure 4.18: Example template fit in the rigidity range of 6.47 to 7.76 GV with data collected from Feb.18.2017 to Jul.30.2017.

The obtained antiproton numbers in 6.47 to 7.76 GV for the 23 groups containing data of six Bartels Rotations each is shown in figure 4.19. The corresponding values of the  $\chi^2/\text{ndf}$  are given in figure 4.20.

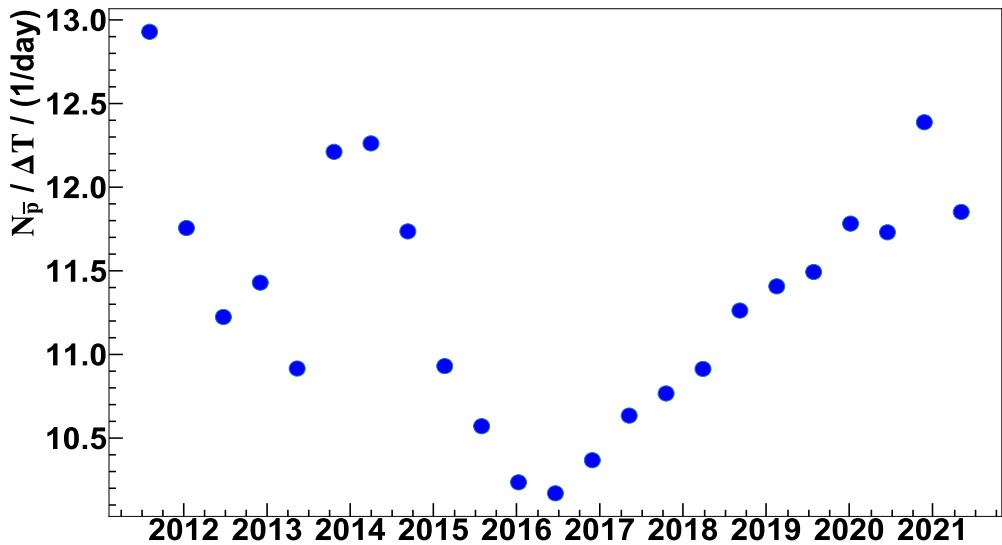


Figure 4.19: The antiproton numbers obtained from the template fit results in the rigidity range of 6.47 to 7.76 GV with six Bartels' Rotation time resolution. To avoid jumps due to the measuring time (see Section 4.6), the numbers are divided by the measuring time in each six Bartels' Rotation time bin.

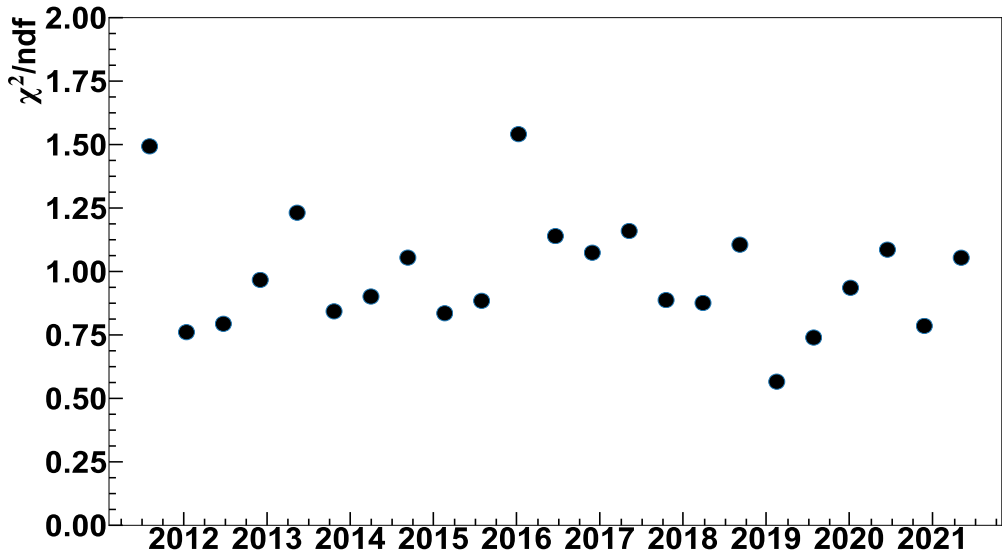


Figure 4.20:  $\chi^2/\text{ndf}$  of the template fits in the rigidity range of 6.47 to 7.76 GV with six Bartel's Rotation time resolution.

## 4.5. Effective Acceptance

After the event number is determined by the template fit, the next important ingredient to calculate the antiproton to proton flux ratio is the effective acceptance.

For a spectrometer, the counting rate of a given particle species depends on the flux intensity and the geometrical acceptance  $A_{\text{geo}}$  [120]. The geometrical acceptance is a fixed value for a certain apparatus, but this assumes no interaction between the traversing particles and the apparatus, while for data analysis, dedicated cuts and selections are applied. Therefore, considering this, the geometrical acceptance is multiplied by the efficiencies of the cuts and the selections  $\epsilon_{\text{cut}}$ . This product is called effective acceptance  $A_{\text{eff}}$ . The larger the effective acceptance, the more events can be collected.

$$A_{\text{eff}} = A_{\text{geo}} \times \epsilon_{\text{cut}} \quad (4.10)$$

Calculating the effective acceptance directly is impossible. The practical way is to use the MC simulation method. In the AMS-02 experiment, different MC production models with the help of Geant4 are widely used. In these models, the whole detector is located inside a cube with an edge length of 3.9 m. To mimic an isotropic flux, the generated artificial particles are continuously emitted on the plane defined by the cube side that lies on the top of the detector, and randomly go down with a solid angle of  $\pi \cdot \text{sr}$ .

According to [120], the acceptance can be calculated with two ingredients: the number of passed events  $N_{\text{pass}}$  and the number of generated events above the top plane  $N_{\text{generated}}$ . The formula is given in equation 4.11. For the calculation of effective acceptance, apart from the geometry of the detectors, the cut efficiency also reduces the number of passed events.

$$A_{\text{eff}} = \pi \cdot A \cdot \frac{N_{\text{passed}}(R_{\text{true}})}{N_{\text{generated}}(R_{\text{true}})} \quad (4.11)$$

where  $A=3.9 \text{ m} \cdot 3.9 \text{ m}$ .

Because the interaction cross sections for proton on carbon and aluminum are different from the cross sections for antiproton on carbon and aluminum especially in the low rigidity range [121, 122, 123, 124], this difference results in different effective acceptance for proton and antiproton in this analysis, and therefore proton effective acceptance  $A_p$  to antiproton effective acceptance  $A_{\bar{p}}$  ratio is not equal to one. In figure 4.21, the effective acceptances of proton and antiproton are given.

The effective acceptance ratio is rigidity-dependent and it is taken from MC first. Due to differences between ISS data and MC simulation, the effective acceptance obtained from MC needs to be corrected with the data/MC efficiency ratio. Since both of the MC determined proton effective acceptance  $A_p^{\text{MC}}$  and antiproton effective acceptance  $A_{\bar{p}}^{\text{MC}}$  need data/MC

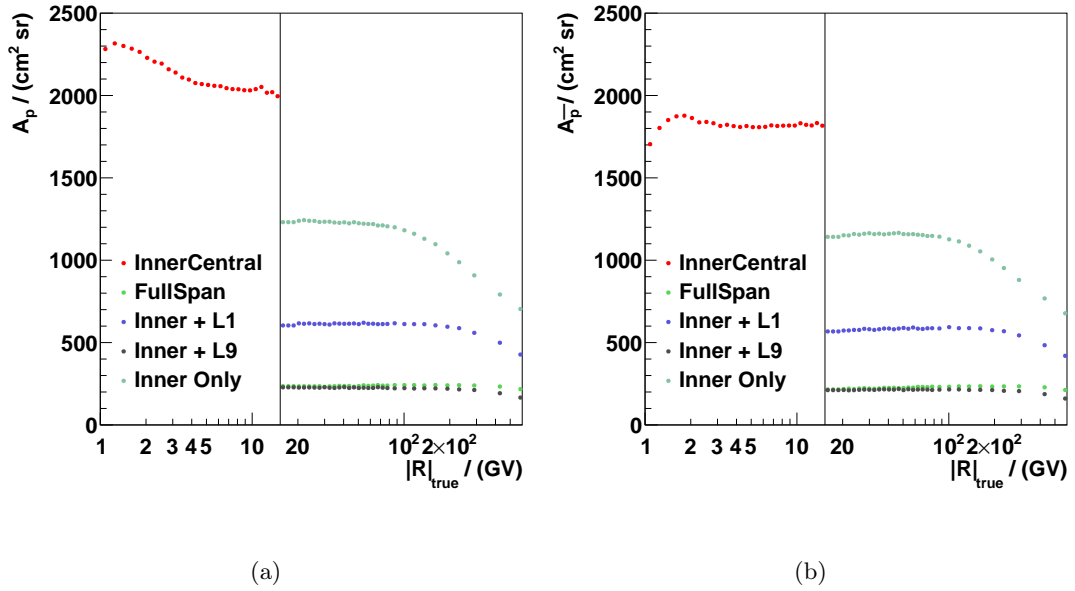


Figure 4.21: Effective acceptance of a) proton and b) antiproton in different rigidity ranges. In the low and intermediate range, the inner central tracker pattern is used. In the high rigidity range, the FullSpan, Inner+L1, Inner+L9 and Inner Only tracker patterns are used. Due to different selections in different rigidity ranges, the effective acceptances are determined individually.

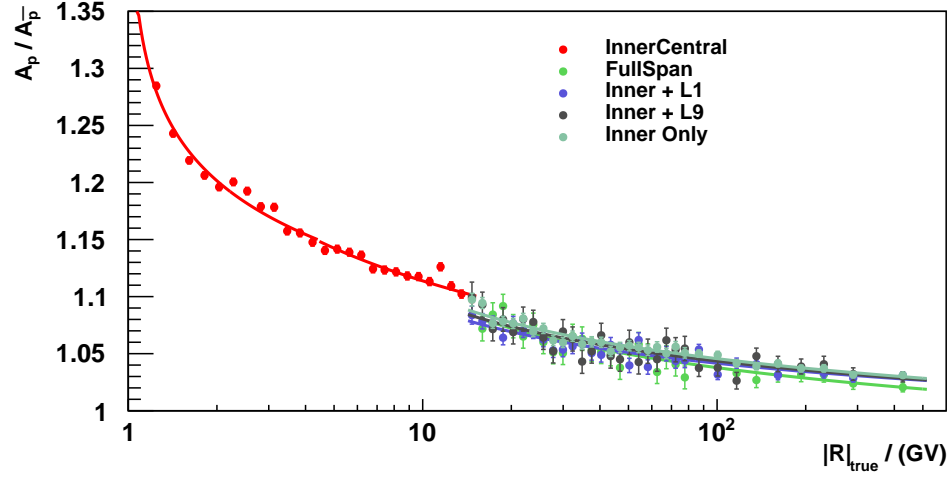


Figure 4.22: Proton to antiproton effective acceptance ratios in different rigidity ranges. Due to the different selections and tracker patterns, the effective acceptance ratios are calculated individually. The uncertainty in this plot is statistical uncertainty only, the uncertainty due to the cross section will be discussed in Section 4.9. To have a smooth curve of the effective acceptance ratio, parameterizations are used.

correction, namely  $\delta_p$  and  $\delta_{\bar{p}}$ . This correction is assumed to be canceled out strictly. The same effect is valid also in the positron/electron ratio analysis [111]. Therefore, the effective acceptances ratio can be purely determined by MC simulations.

$$\frac{A_p}{A_{\bar{p}}} = \frac{A_p^{\text{MC}}}{A_{\bar{p}}^{\text{MC}}} \cdot \frac{1 + \delta_p}{1 + \delta_{\bar{p}}} = \frac{A_p^{\text{MC}}}{A_{\bar{p}}^{\text{MC}}} \quad (4.12)$$

Due to the different selections and different tracker patterns in three rigidity ranges, the proton to antiproton effective acceptance ratios are slightly different and determined individually. In figure 4.22, the antiproton to proton effective acceptance ratio is shown. To avoid fluctuations in the effective acceptance ratios, the parameterizations of the effective acceptance ratios are done in different ranges individually.

## 4.6. Measuring Time

Although the measuring time is canceled in the antiproton to proton flux ratio calculation, it has to be determined due to the rigidity cutoff in the cuts and selections, which explains the low statistics in the low rigidity analysis. Also, in the time-dependent analysis, the measuring time in six Bartels Rotations helps to understand the antiproton number changes. Furthermore, in the MC simulation the rigidity cutoff is not simulated, this effect has to be corrected in unfolding.

The measuring time is the total time that all the sub-detectors are in nominal operation and could record events. Due to the detector's operation cuts and the trigger dead time, which is the time needed for readout, the measuring time is lower than the exposure time, which is the total data-taking time since the start of the experiment.

Because of the trigger dead time, if the event trigger rate goes up and surpasses the threshold, then not all the events can be detected and recorded. Therefore, the live time fraction can be defined as the fraction of a second that the trigger is ready to record. Because the amount of incoming particles depends on the ISS position in the geomagnetic field, the live time fraction is close to one in most areas but less than one in high latitude areas, see figure 4.23. Also, in the SAA, there are plenty of low energy particles going through the detector. Therefore, the trigger rate in this area is very high, and the live time fraction is very low correspondently. In figure 4.24, the measuring time as function of live time fraction is given. For the entire data-taking period, the live time fraction is mostly above 90%.

Due to the Earth's magnetic field, a charged particle can be deflected before it reaches the detectors at low earth orbit, where the AMS-02 is located. The deflection power depends on the particle's rigidity and the particle's relative orientation to the magnetic field lines.

The Earth's magnetic field axis is tilted at an angle of  $11.5^\circ$  with respect to the Earth's rotational axis, as illustrated in figure 4.25. Therefore, the lowest rigidity threshold to

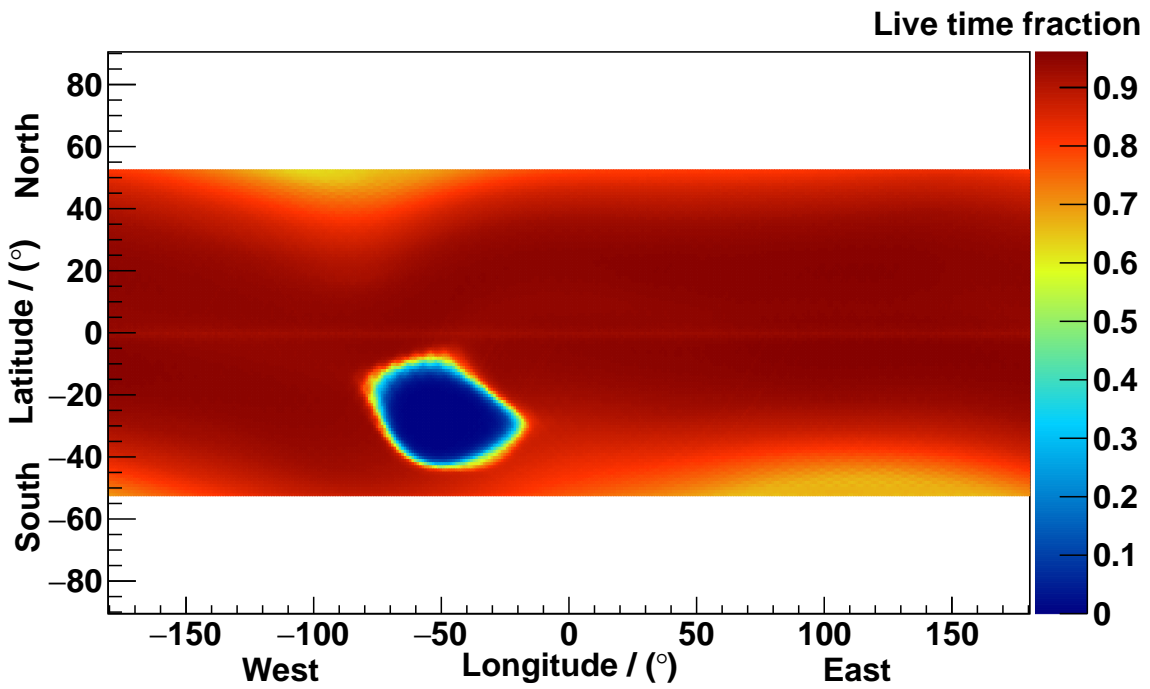


Figure 4.23: Live time fraction vs. ISS position. The live time fraction in the most areas is above 0.9 while in the SAA is extremely low due to plenty of low energy particles.

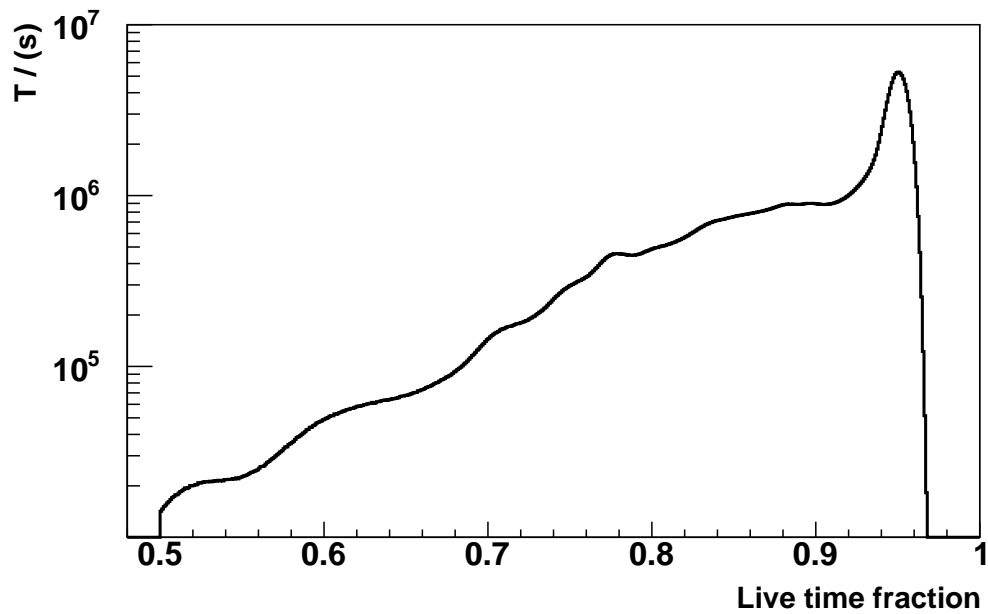


Figure 4.24: Measuring time as a function of the live time fraction. For most of the measuring time, the live time fraction is above 0.9.

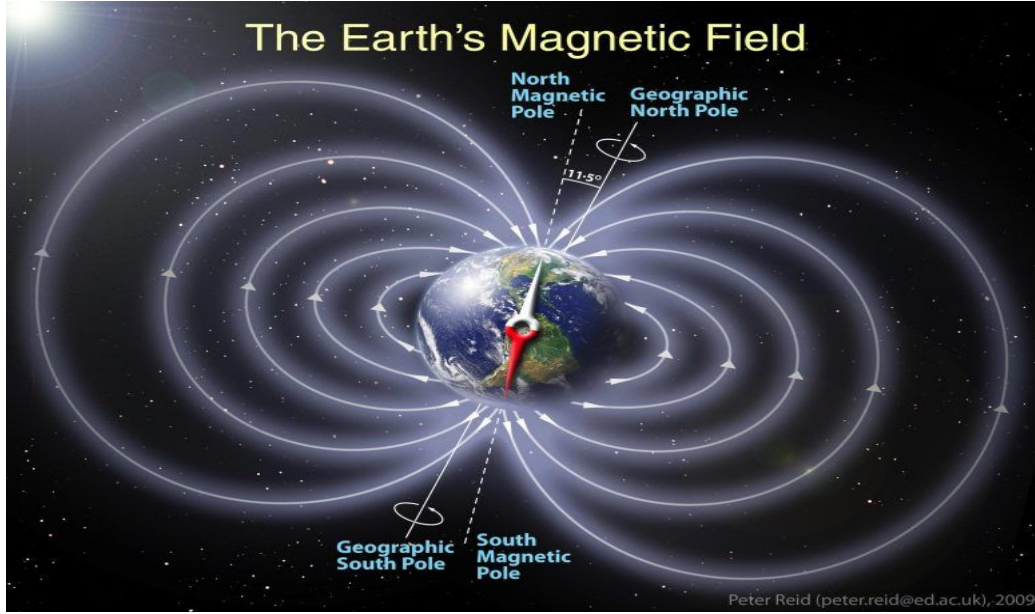


Figure 4.25: Illustration of the Earth’s magnetic field. The angle between the Earth’s magnetic field axis and the Earth’s rotational axis is  $11.5^\circ$ . Credit: Peter Reid, The University of Edinburgh

penetrate the Earth’s magnetic field should be a function of the Earth’s location. The lowest rigidity threshold is called *rigidity cutoff*.

To get rid of these events which are deflected by the Earth’s magnetic field, the following requirement is applied:

$$R_{\text{low}} > R_c \times f \quad (4.13)$$

where  $f$  is the safety factor, which is set to be 1.2 in this analysis,  $R_c$  is the cutoff rigidity, and  $R_{\text{low}}$  is the lower edge of rigidity bin, which in the measured rigidity is classified.

For the rigidity cutoff, there are two kinds of cutoffs used in the AMS-02 collaboration: Størmer cutoff and International Geomagnetic Reference Field (IGRF) cutoff. The Størmer cutoff is only valid for the approximation of a pure dipole field. Since the geomagnetic field deviates from a pure dipole field, the IGRF cutoff takes deformations in the geomagnetic field into account and therefore more accurate. Both of the two cutoffs will be discussed in this section.

For the Størmer rigidity cutoff, the equation 4.14 gives the formula to calculate the cutoff  $R_c$  [125] :

$$R_c = \frac{M \cos^4 \lambda}{r^2 (1 + \sqrt{1 - \sin \epsilon \cdot \sin \delta \cdot \cos^3 \lambda})^2} \quad (4.14)$$

where  $M$  is the geomagnetic dipole moment with a typical value of 58 [126] ,  $\lambda$  is the magnetic latitude,  $r$  is the altitude distance from the dipole center,  $\epsilon$  and  $\delta$  are the zenith and azimuthal angles of the particle, respectively.

With the cuts and selection introduced in Section 4.1, the calculated Størmer rigidity cutoff for events with zenith angle up to  $25^\circ$  as a function of ISS position is given in figure 4.26.

The total measuring time can be obtained by integrating the live time fraction in every second of the whole data-taking period.

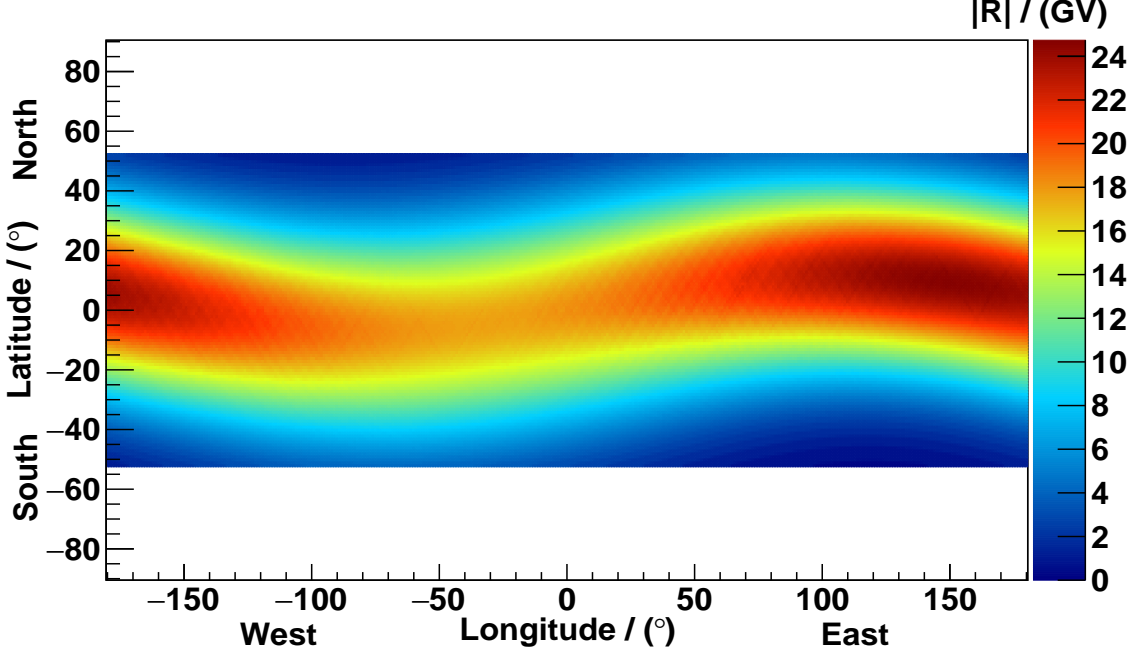


Figure 4.26: The Størmer rigidity cutoff used in this analysis as a function of the ISS Position. The maximum value of the cutoff is less than 26 GV.

After the preselection cuts introduced in Section 4.1 which ensure good operation quality of the sub-detectors, the resulting measuring time as a function of rigidity used in this analysis is shown in figure 4.27. The integrated data-taking time from 20. May 2011 to 03. May 2021 is 3636 days. Due to the ISS position, detector operations like TRD gas refills and the time spent inside the SAA, the actual measuring time is around 68% of the total data taking time. This leads to a measuring time of 2488 days above the geomagnetic cutoff.

Another method used by the AMS-02 collaboration to calculate the rigidity cutoff is the IGRF method. To calculate the track of particle which penetrates the magnetic field, a solution is to consider the backtracing particles. With a given position and a specified rigidity, the back-trajectory of a charged particle can be traced by numerical integration through a mathematical model of the geomagnetic field, IGRF model, until the particle either reaches the interplanetary magnetic field, or intersects the atmosphere. In this way,

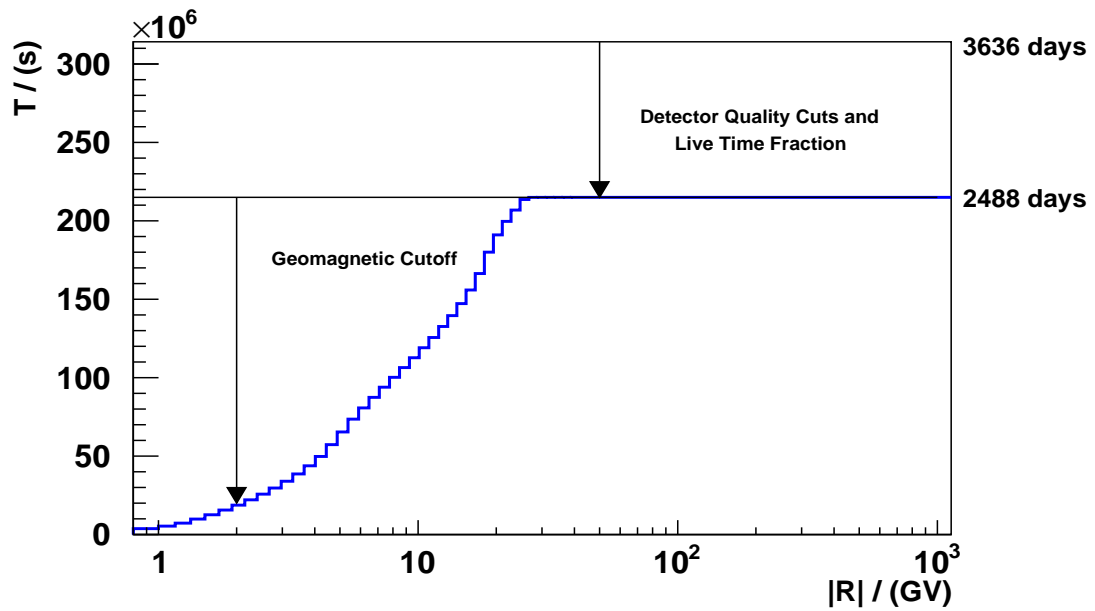


Figure 4.27: The measuring time obtained from the Størmer geomagnetic cutoff. After the quality cuts and live time fraction, the resulting total measuring time is around 2488 days.

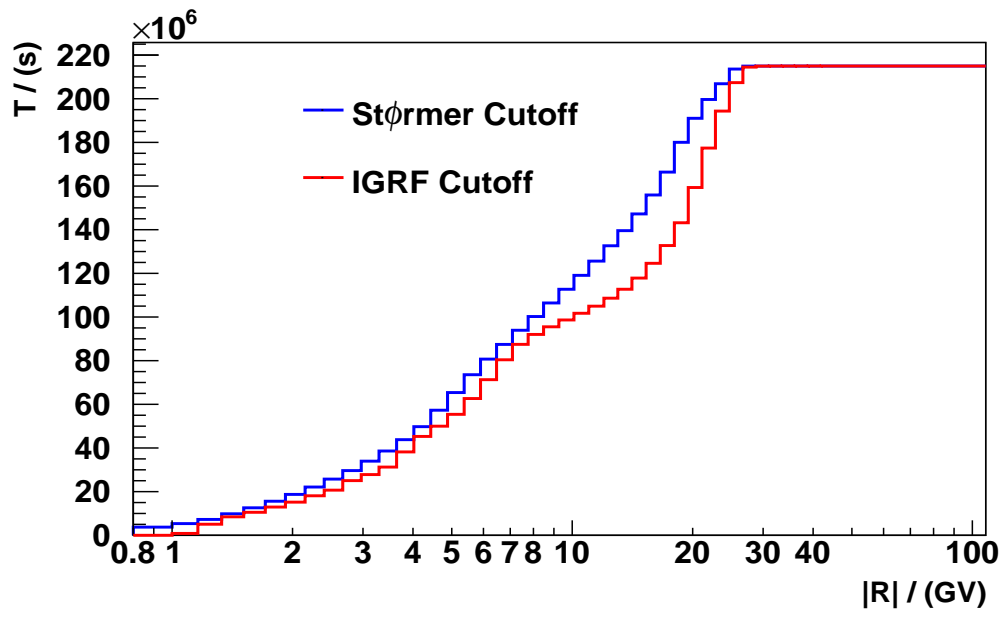


Figure 4.28: The measuring time comparison between the Størmer and IGRF cutoffs. The IGRF cutoff leads to lower measuring time.

the threshold of rigidity is the cutoff rigidity for this position.

Figure 4.28 shows the comparison between the measuring time achieved from the IGRF method and the Størmer cutoff method. As shown in the figure, compared to the IGRF method, using the Størmer cutoff leads to higher statistics in the low rigidity range. This is important for the time-dependent analysis since the statistics in the fine time bin are limited. Also, using the IGRF method leads to almost zero measuring time in the first one to two rigidity bins (less than 1.16 GV). Therefore, the data could only be analyzed in the higher rigidity bins. So in this analysis, the Størmer cutoff is used to determine the measuring time though it is based on the approximation of the dipole field.

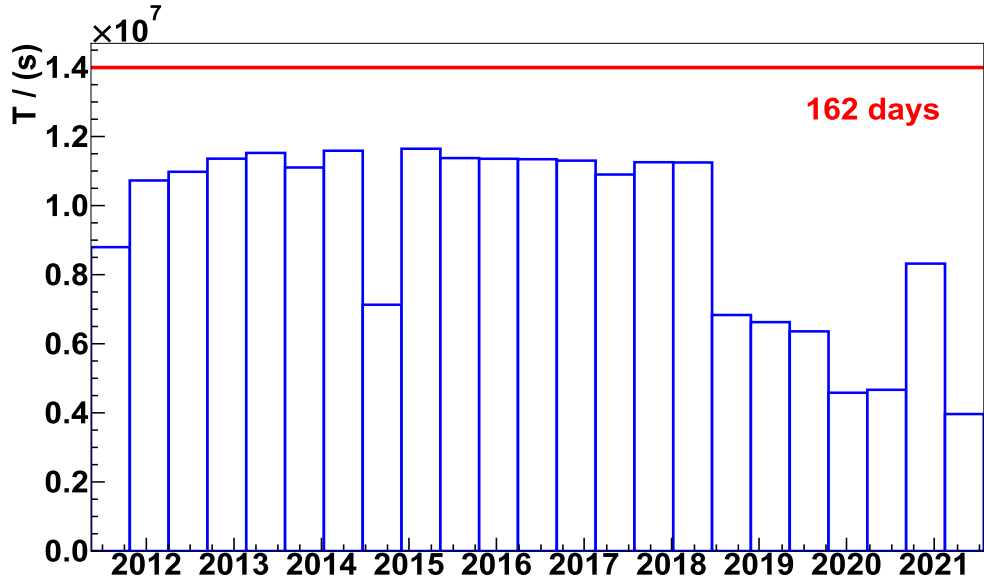


Figure 4.29: The measuring time in each six Bartels Rotations time bin. After the middle of 2018, the measuring time in each time bin decreased due to frequent changes of the pump running status. The red line indicates the exact six Bartels Rotations (162 days).

For the time-dependent analysis, the collected ISS data is divided into every six Bartels Rotations time bin. In each time bin, the total measuring time depends on the detector operation in these individual six Bartels Rotations. In figure 4.29, the measuring time in the 23 six Bartels Rotations time bins is shown.

## 4.7. Unfolding

To calculate the antiproton to proton flux ratio, the number of events should be determined based on the true particle's rigidity. However, the number of events from the template fits is determined based on the reconstructed rigidity. There are differences between these two rigidities because of the limited tracker resolution. Some events may end up in different

rigidity bins, and this effect is called "bin to bin migration". To correct this effect, a procedure called *unfolding* is applied. Due to the different distributions of the number of events for antiproton and proton, this effect is not canceled out in the calculation of antiproton to proton flux ratio.

There are several methods to correct this effect and the easiest way is by matrix inversion of the migration matrix:

$$\hat{n} = M \cdot n \quad (4.15)$$

where  $\hat{n}$  is the unfolded event number which is counted in the true rigidity bin,  $n$  is the raw event number which is counted in the measured rigidity bin, and  $M$  is the migration matrix. The migration matrix is a 2D histogram that is obtained by filling the events in the MC simulation directly. The X axis is the reconstructed rigidity, and the Y axis is the true rigidity generated in the MC.

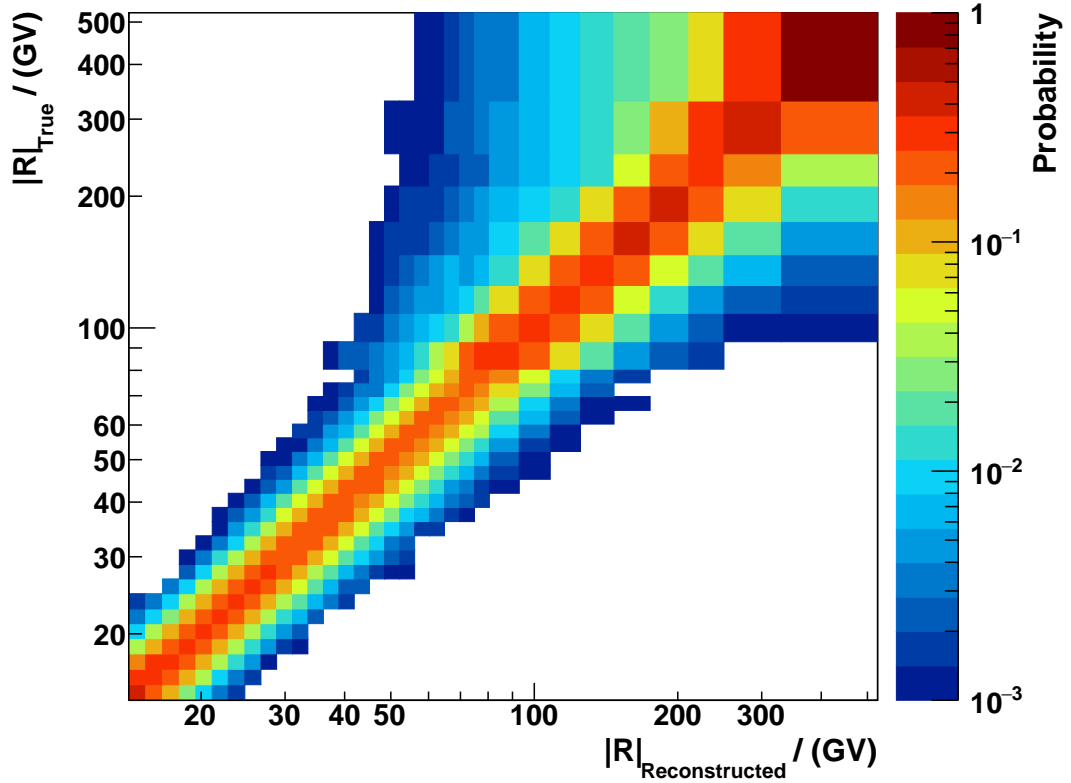


Figure 4.30: The migration matrix for full span at the high rigidity range for proton MC events. The X axis is the reconstructed rigidity from the tracker and the Y axis is the true rigidity from the generated momentum in MC.

This simple inversion method works but it is not recommended, since it gives large bin-bin correlations and magnifies statistical fluctuations. Therefore, a more complicated method called "Bayesian unfolding" is used in this work. The Bayesian unfolding method is implemented in the "RooUnfold" package in ROOT [127] and is also used in the AMS-02 electron and positron analysis [111]. This method applies Bayes' theorem repeatedly to invert the migration matrix and it gives more reliable results [128].

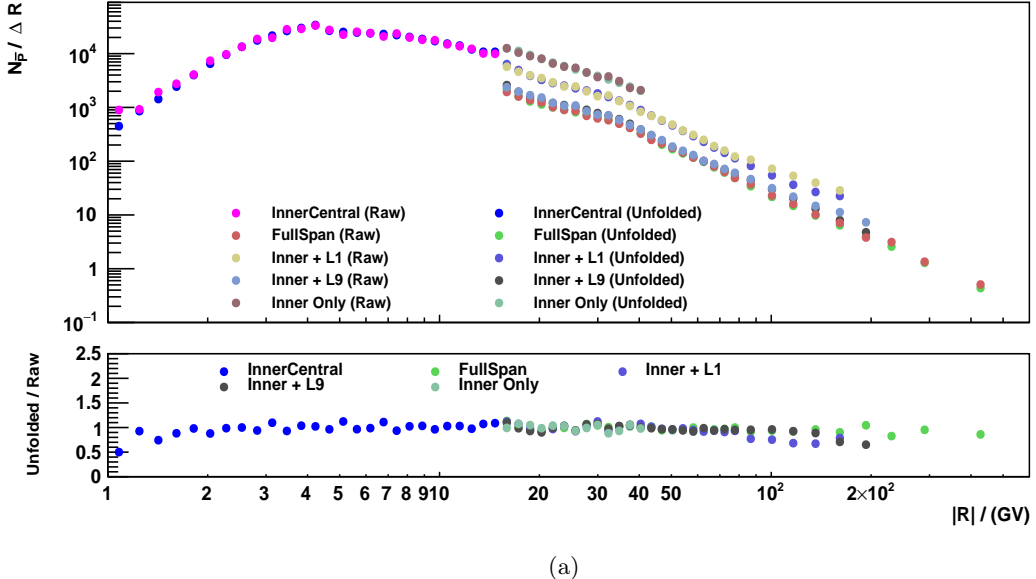
In this analysis, the signals are determined with different selections for different rigidity ranges. Also, for the different tracker patterns, the migration matrices are different due to the different tracker pattern resolutions. In figure 4.30, the migration matrix for full span at the high rigidity range using proton simulated events is given as an example. For illustration, the histogram is normalized by ensuring the sum of probabilities in every projection along the Y axis is 1. From the figure, the diagonal elements of the matrix are the events whose true rigidity matches the reconstructed rigidity, which is the dominant part of the total events. As the rigidity increases, the bin contents of the non-diagonal elements increase too. This is due to the tracker resolution becoming worse in higher rigidity.

As explained in Section 4.6, the collected data fulfill the rigidity cut off condition. This cutoff effect is not simulated in the MC simulation process, so it must be taken into account before we use the migration matrix. Therefore, the shape of the measuring time in figure 4.27 is used as a weight for the events under the rigidity cutoff.

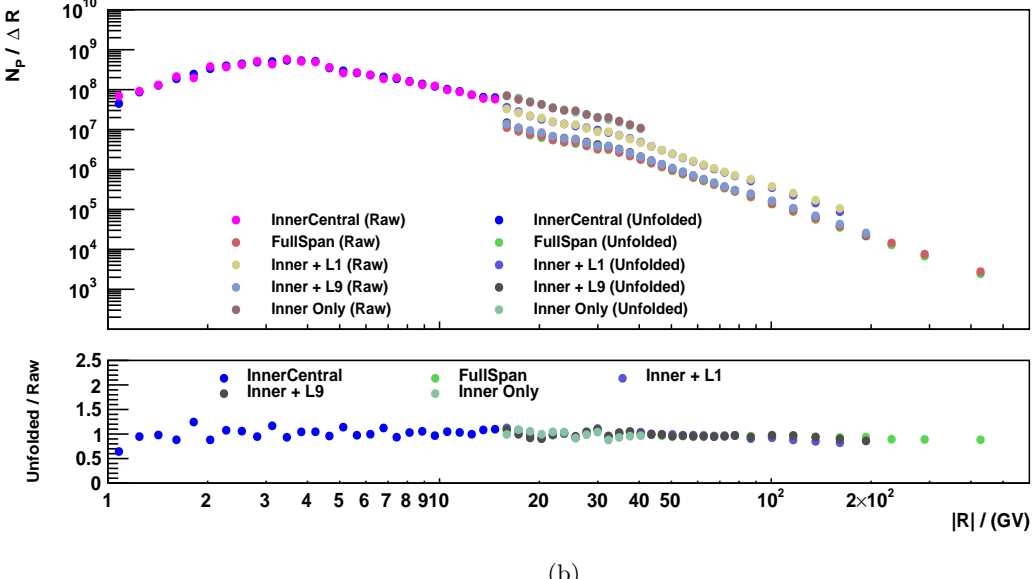
In this analysis, the focus is placed on the antiproton to proton ratio. Therefore, the unfolding process has to be performed for the antiproton raw event counts and the proton raw event counts respectively. The antiproton raw event counts are taken from the template fit results, and the proton raw event counts are the event counts after the cuts and selections. In figure 4.31, the raw and unfolded event counts are given for protons and antiprotons respectively.

## 4.8. Antiproton To Proton Flux Ratio

In this section, the antiproton to proton flux ratio is given with statistical uncertainty only. According to equation 4.3, the calculated time-averaged antiproton to proton flux ratio is given with statistical uncertainty only in figure 4.32. Since the antiprotons are determined from different template fits in three different rigidity ranges, the results in these two overlapping ranges are also given. In the two overlapping ranges, the results are consistent with each other. In figure 4.33, the time-averaged antiproton to proton flux ratio without overlapping is given. The overlapping range is dealt with the best matching results. Below 4.43 GV the result in the low rigidity range is used. From 4.43 to 15.3 GV the result in the intermediate range is used. Above 15.3 GV the result in the high rigidity range is used. In figure 4.34, the relative statistical uncertainty of the antiproton to proton flux ratio is shown. The systematic uncertainty study will be shown in the next section.



(a)



(b)

Figure 4.31: The raw and unfolded events for a) antiproton b) proton over rigidity bin width. Different migration matrices are used for different tracker patterns. Due to the different shapes of the raw event distributions for antiproton and proton, this unfolding effect can not cancel strictly.

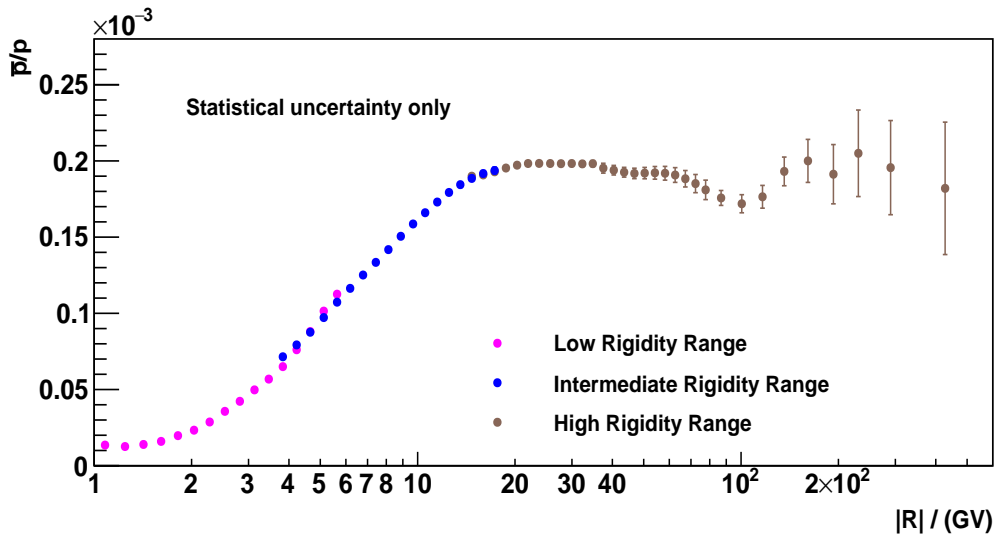


Figure 4.32: The time-averaged antiproton to proton flux ratio in three rigidity ranges. In the two overlapping ranges, the results from different template fit methods are consistent with each other. The error bars are the statistical uncertainty only.

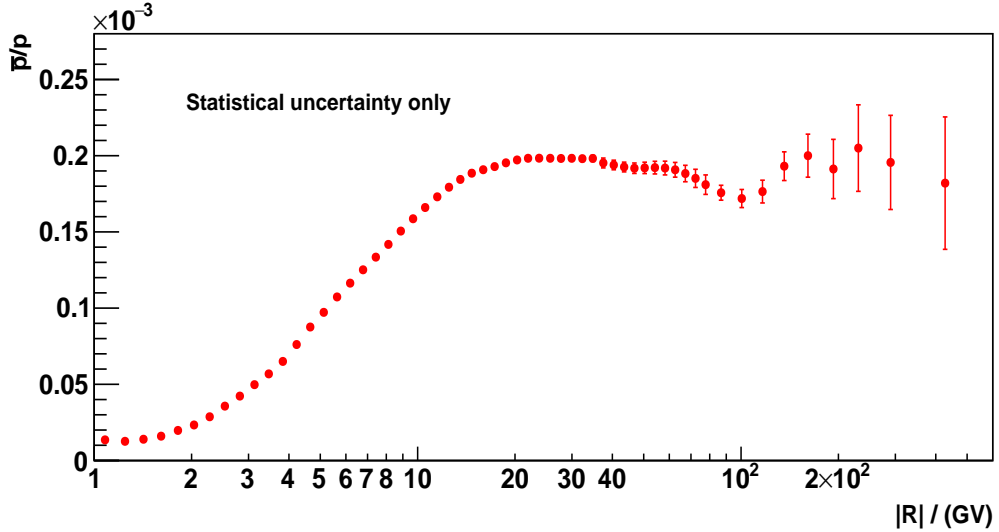


Figure 4.33: The time-averaged antiproton to proton flux ratio with statistical uncertainty only.

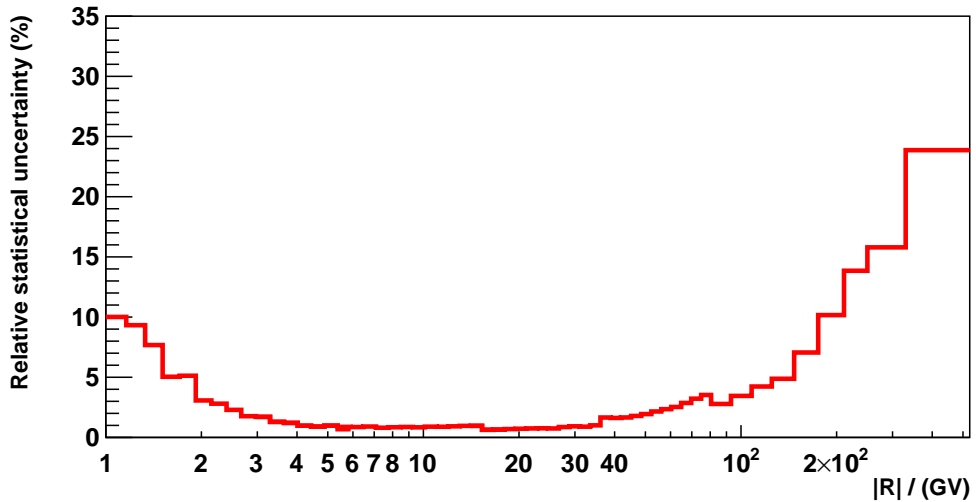


Figure 4.34: The relative statistical uncertainty of the antiproton to proton flux ratio.

For the time-dependent antiproton to proton flux ratio, the calculation is based on equation 4.4. As an example, the antiproton to proton flux ratio with statistical uncertainty only in the rigidity range of 1.92 to 2.4 GV is shown in figure 4.35. The corresponding statistical uncertainty is given in 4.36.

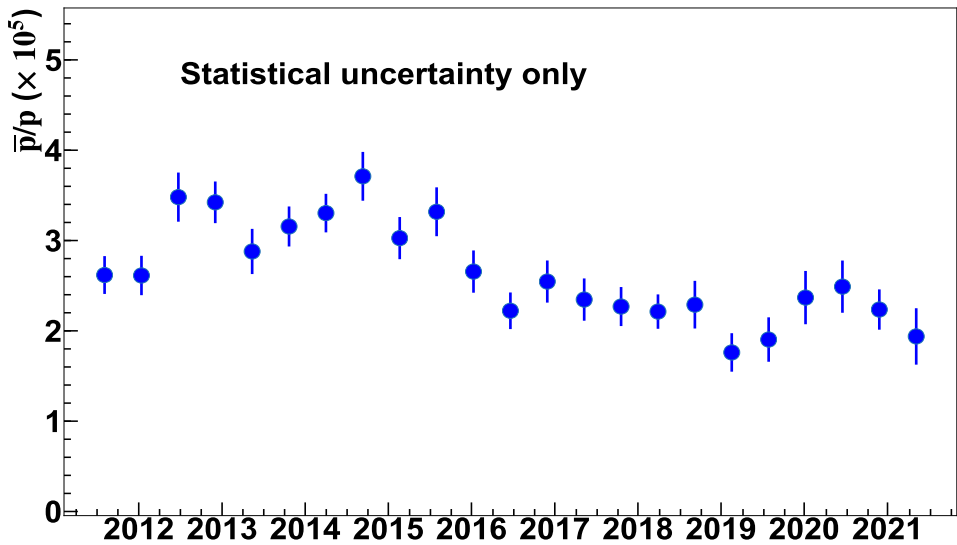


Figure 4.35: The antiproton to proton flux ratio in the rigidity range of 1.92 to 2.4 GV in six Bartels Rotation time bin.

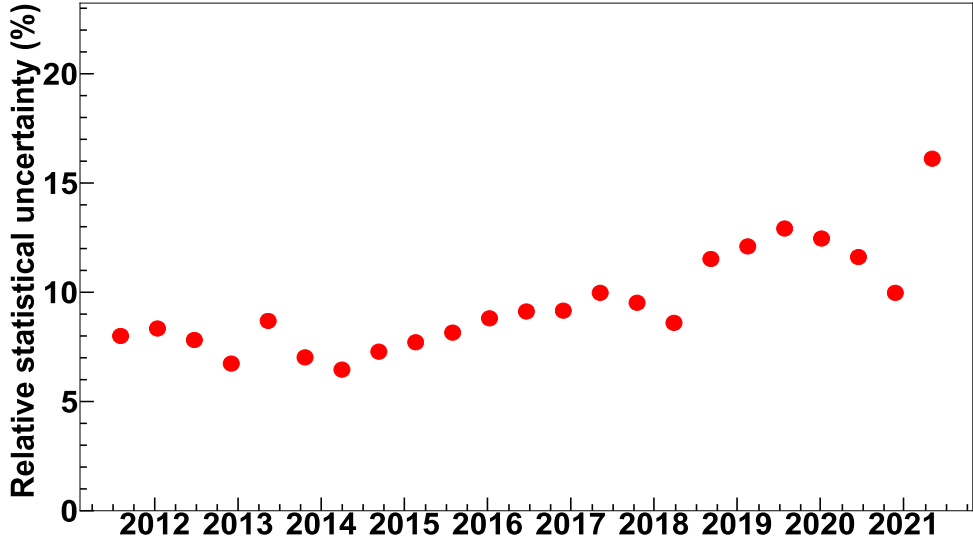


Figure 4.36: The relative statistical uncertainty of the antiproton to proton flux ratio in the rigidity range of 1.92 to 2.4 GV in six Bartels Rotation time bin.

## 4.9. Systematic Uncertainties

In this section, the systematic uncertainties are discussed. Due to the different template fit methods used in the three different rigidity ranges (low, intermediate, high), the systematic uncertainties are discussed separately for each rigidity range.

The antiproton to proton flux ratio is calculated according to equation 4.3. There are two components in this equation: Number of events  $N$  and effective acceptance  $A$ . These components consist the sources of the systematic uncertainties on the flux ratio.

### 4.9.1. Time-averaged analysis

#### Systematic uncertainty from Effective Acceptance

The first source of systematic uncertainty is the effective acceptance. Since the effective acceptance data/MC correction cancels out, this systematic uncertainty is determined completely by the MC simulation. As the interaction cross sections of proton and antiproton are different, their effective acceptances differ too. Since the antiproton cross section measurement has much more uncertainty than proton cross section measurement, therefore is the dominant impact factor in the effective acceptance systematic uncertainty. Two dedicated antiproton MC simulation samples are generated to estimate the asymmetry of the effective

acceptances. In these two antiproton MC samples, the antiproton interaction cross sections are set to nominal  $\pm 10\%$ , which is determined by the antiproton cross section measurements data. In figure 4.37, the uncertainty band shows how the effective acceptance ratio changed by varying 10% of the antiproton cross section. This is the systematic uncertainty of effective acceptance. In figure 4.38, the obtained systematic uncertainty as a function of the rigidity is shown.

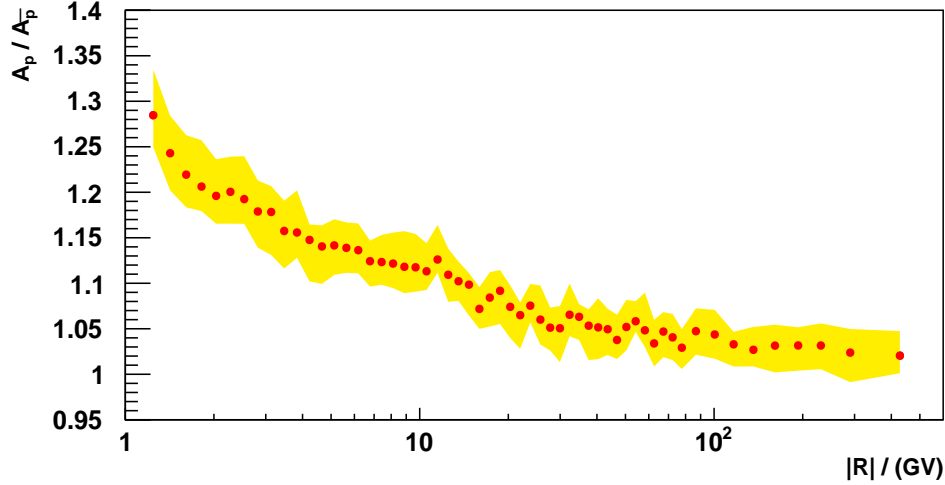


Figure 4.37: Proton over antiproton effective acceptance ratio with antiproton cross sections varied by  $\pm 10\%$ . The red points are the effective acceptance ratio obtained with nominal antiproton cross section, the yellow band shows the uncertainty due to the antiproton cross section uncertainty of 10%.

### Systematic uncertainty from Event Numbers

The second source of systematic uncertainty is the number of events. In the different rigidity ranges, the antiproton number of signal events is determined by different template fit methods given the different kinds of backgrounds relevant to each range. Therefore, the systematic uncertainty on the number of events has to be calculated separately for each rigidity range.

In the low rigidity range, the antiproton signal is derived from a 2D template fit in  $1/\beta_{\text{TOF}}$  and  $\Lambda_{\text{TRD}}$  as shown in figure 4.7(b). A variation of the template fit range is used to estimate the template fit result. As introduced in Section 4.4, the template fit result at 90% signal efficiency is used in the final antiproton to proton flux ratio. To estimate the systematic uncertainty, the template fit is performed 342 times with signal efficiency from 40% to 95%. For the first five rigidity bins, the signal efficiency range starts from 65% due to low statistics. Then the RMS of the results distribution is chosen as the systematic error in each rigidity bin.

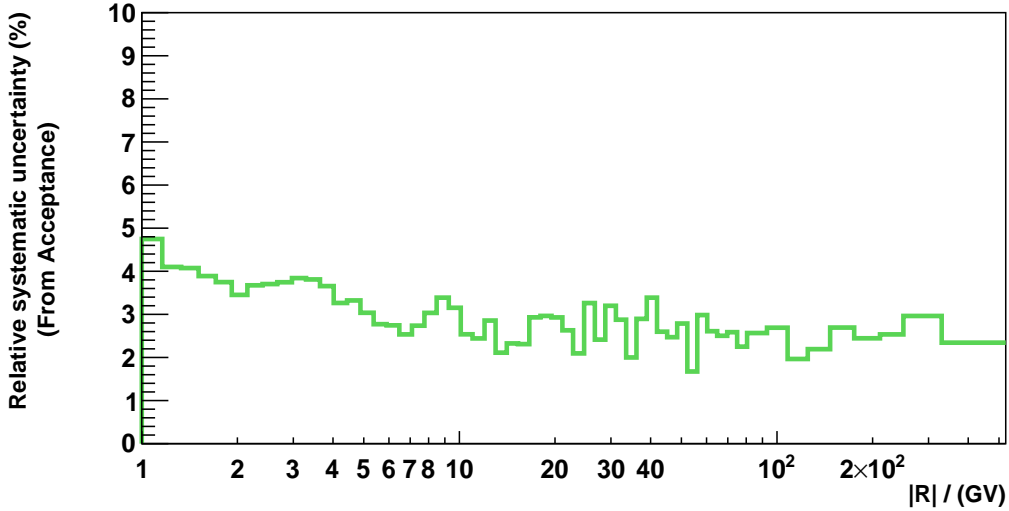


Figure 4.38: The relative systematic uncertainty of the antiproton to proton flux ratio from acceptance.

In the intermediate rigidity range, the same logic to calculate the systematic uncertainty is used, but the difference is that the template fit in this range is a 1D template fit in  $\Lambda_{\text{TRD}}$ . So in this range, the template fit is performed while varying the signal efficiency from 60% to 100%.

In figure 4.39, an example of the template fit results while varying the signal efficiency is shown. The rigidity bin is from 2.15 to 2.4 GV at the low rigidity range, and the RMS of the results is used as the systematic error in this bin.

In figure 4.40, the systematic uncertainty from the template fit range is shown.

In the high rigidity range, the charge confused proton background rises dramatically with increasing rigidity. The template of the charge confused protons, which is obtained from proton MC, becomes the primary source of systematic uncertainty.

To estimate the systematic uncertainty due to the charge confused protons, the charge confusion level (CCLevel) between MC and ISS data is used. The CCLevel is defined as follow:

$$\text{CCLevel} = \frac{N_{\text{CCProtons}}}{N_{\text{CCProtons}} + N_{\text{Protons}}} \quad (4.16)$$

where  $N_{\text{Protons}}$  is the number of charge correct protons and  $N_{\text{CCProtons}}$  is the number of charge confused protons.

In figure 4.41, the calculated CCLevels in the MC and the data are given. Similar to

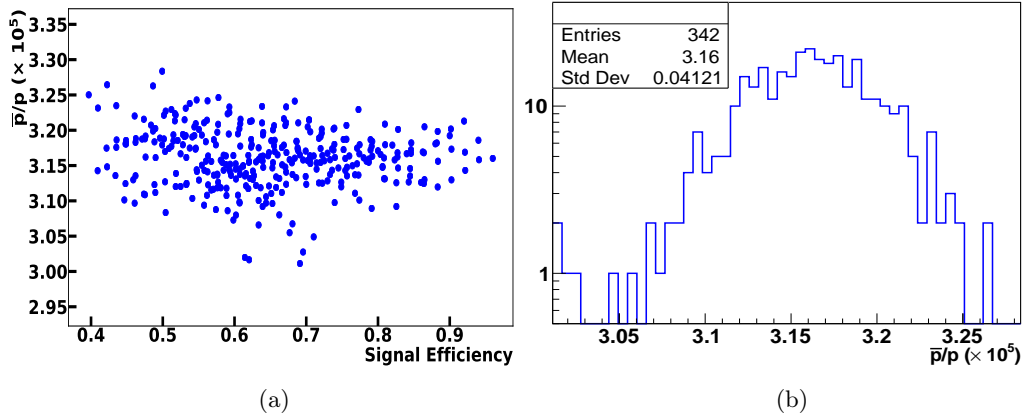


Figure 4.39: The template fit results for the antiproton to proton ratio in the rigidity bin from 2.15 to 2.4 GV while varying the signal efficiency from 40% to 95%. a) The template fit result distribution as a function of signal efficiency. b) The template fit result histogram. The RMS of the histogram is used as the systematic uncertainty.

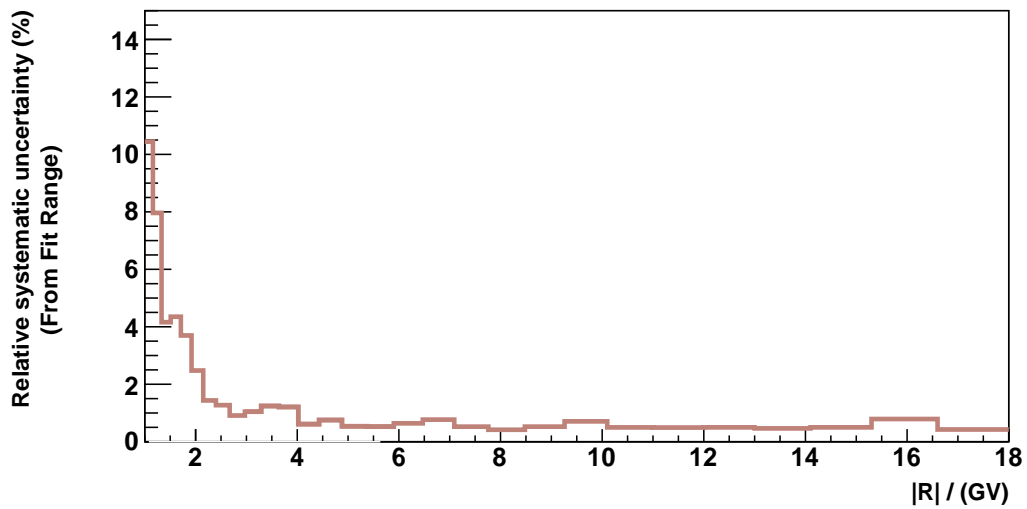


Figure 4.40: The relative systematic uncertainty of the antiproton to proton flux ratio from the template fit range.

performed template fit, an additional cut on  $\Lambda_{CC} = 0.2$  is applied in this plot. The CCLevel in the MC can be calculated directly by selecting the positive and negative rigidity. For CCLevel in the data, since it is impossible to extract charge confused protons from data directly, the number of charge confused protons from the template fit result is used to calculate the CCLevel.

In figure 4.42, the ISS data/MC CCLevel ratio is shown. The uncertainty band is 68% confidence interval with a bump below 240 GV to include more points. According to the definition of the CCLevel and considering that the number of protons is much larger than the number of charge confused protons, the uncertainty in CCLevel can transfer to the uncertainty of the number of charge confused protons. For the template fit at the high rigidity range described in Section 4.4, the number of charge confused protons can be obtained. Then the template fit is repeated again with the fixed number of charge confused protons from the first template fit result plus its uncertainty. The difference between the first template fit result and the second repeated template fit results is used as the systematic uncertainty from the charge confusion.

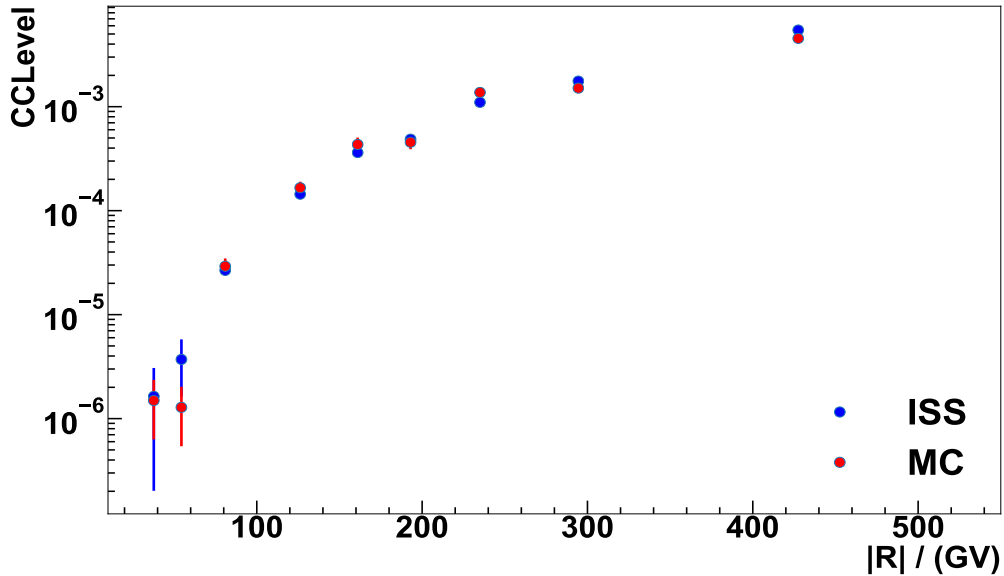


Figure 4.41: Charge confusion level in MC and data.  $\Lambda_{CC} = 0.2$  is applied for this plot.

In figure 4.43 the systematic error due to the charge confusion is shown.

The different systematic uncertainties are added quadratically to arrive at the total systematic uncertainty. In figure 4.44, the total systematic uncertainty of the antiproton to proton flux ratio is presented.

There are some other systematic uncertainties studied in previous AMS-02 antiproton publication [57] but not mentioned in this work, because they only contribute small uncertainties

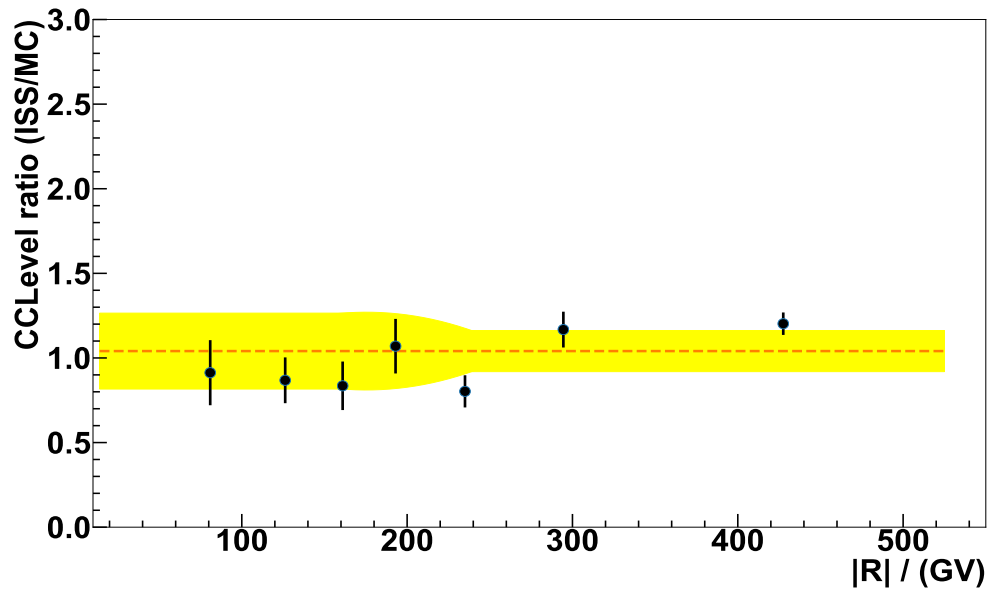


Figure 4.42: ISS data/MC charge confusion level ratio. The uncertainty band is 68% confidence interval with a bump below 240 GV to include more points.

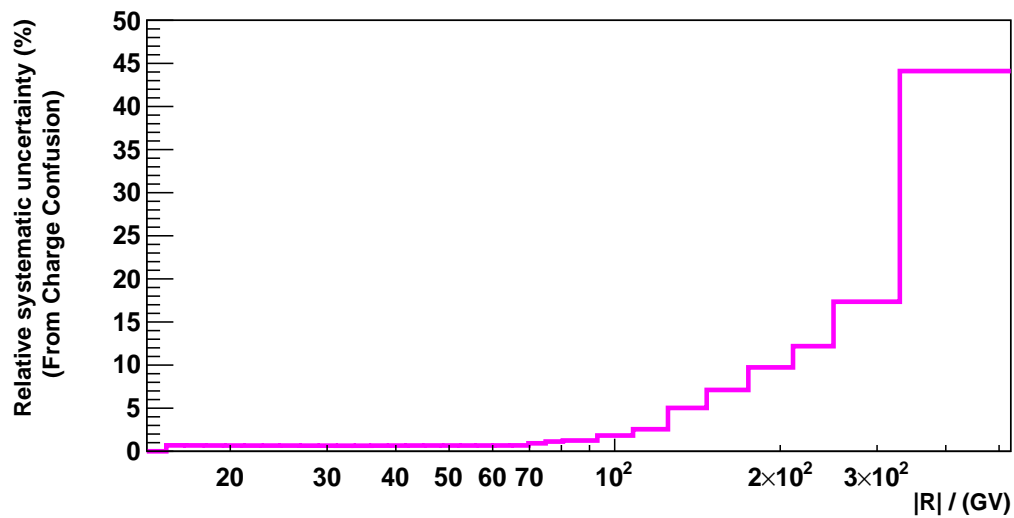


Figure 4.43: The relative systematic uncertainty of the antiproton to proton flux ratio from the charge confusion.

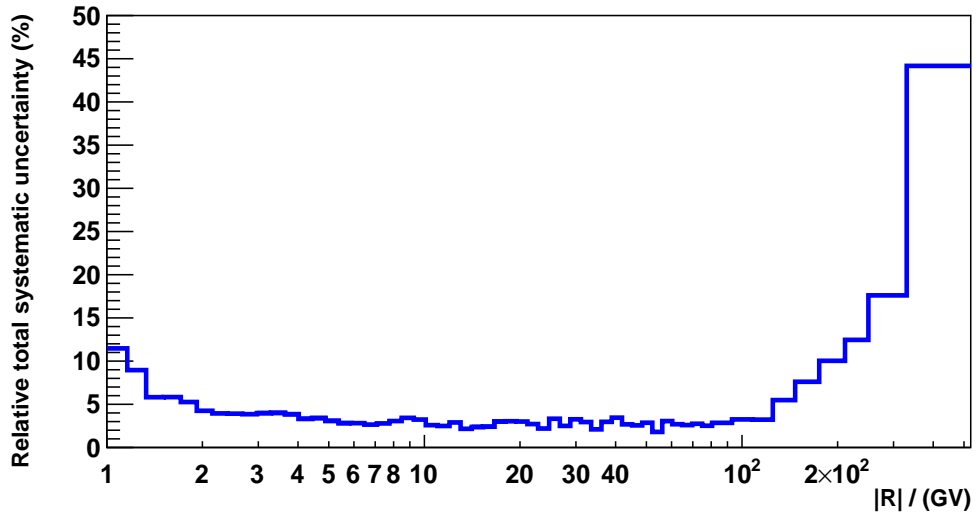


Figure 4.44: The relative total systematic uncertainty of the antiproton to proton flux ratio.

compared to the sources studied in this work. For example, the geomagnetic cutoff safe factor is set to be 1.2 in this work, and varying this value leads to a systematic uncertainty. This effect has been studied in the previous publication and contributes only 1% at 1 GV and becomes negligible above 2 GV. Another systematic uncertainty is from the absolute rigidity scale. Due to the residual misalignment of the tracker planes, the measured rigidity could be shifted. This effect is negligible below 10 GV and gradually up to 2% at the highest rigidity bin.

The statistical uncertainty is directly taken from template fit in different rigidity ranges. The total uncertainty of the antiproton to proton flux ratio is calculated by adding in quadrature the statistical and the total systematic error.

#### 4.9.2. Time-dependent analysis

For the time-dependent analysis, the same procedure is followed. Since the time-dependent analysis is only performed in the rigidity range below 20 GV, the systematic uncertainties are calculated only in the low and intermediate rigidity ranges.

In the low and intermediate rigidity range, the systematic uncertainties are from the acceptance and fit range. Since the acceptance is taken from MC, therefore it is time-independent. The template fit is performed in each six Bartels Rotation time bin so it is time-dependent. In figure 4.45, the systematic error in the rigidity bin from 1.92 to 2.4 GV in six Bartels Rotation time bin is shown as an example.

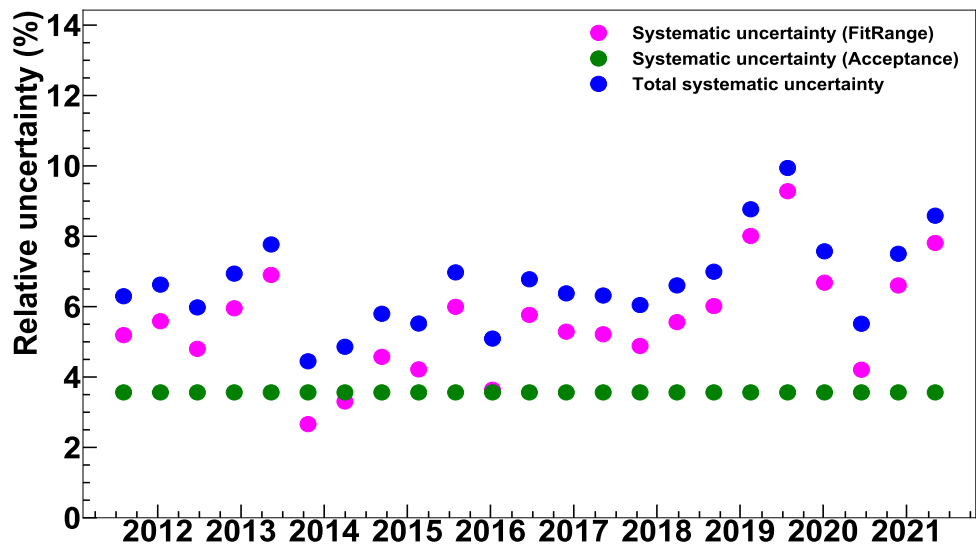


Figure 4.45: The contributions of different sources of the systematic uncertainty and the relative total systematic uncertainty of the antiproton to proton flux ratio in the rigidity bin of 1.92 to 2.4 GV in six Bartels Rotation time bin.

# CHAPTER 5

## RESULTS

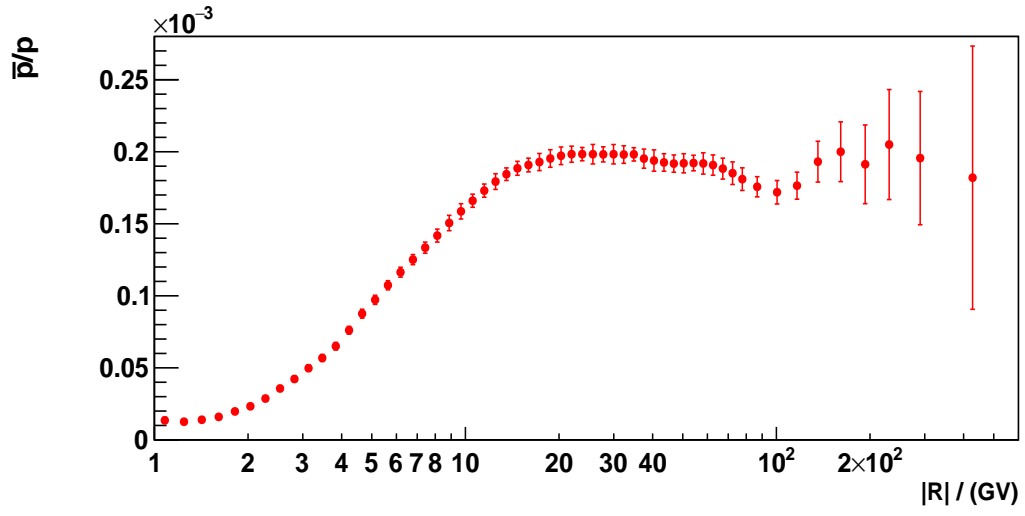
In chapter 4, all the ingredients to calculate the antiproton to proton flux ratio with statistical and systematic uncertainties are given. In this chapter, the measured antiproton to proton flux ratio for the time averaged and the time dependent analysis is shown.

### 5.1. Time Averaged Result

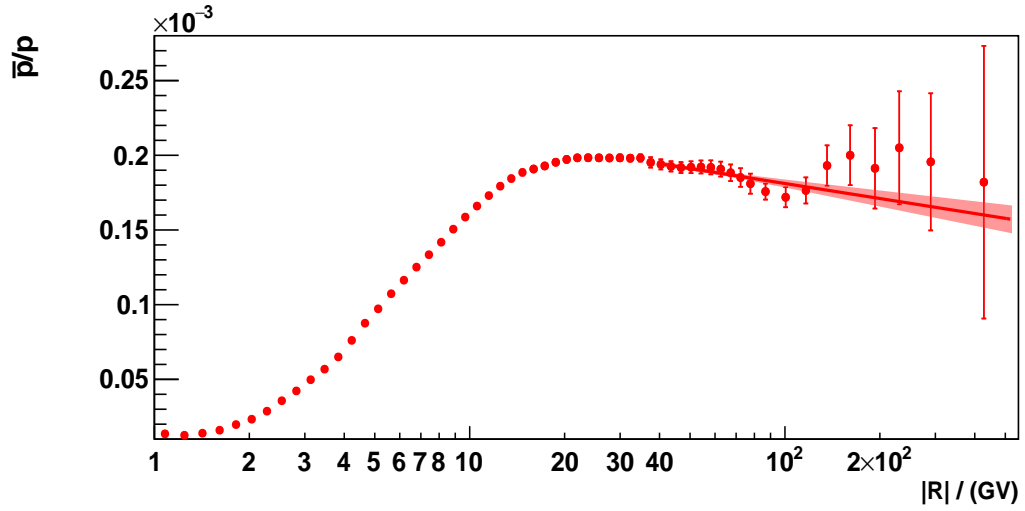
In August 2016, the AMS-02 collaboration published the time-averaged antiproton to proton flux ratio as a function of the rigidity for up to 450 GV, using data collected during the first four years of the experiment’s operation (May 2011 to May 2015) [57] . In Feb 2021, the AMS-02 collaboration published the flux ratio for up to 525 GV using the data accumulated during the first six and a half years of operation [80] . The AMS-02 experiment has been still in operation collecting continuously cosmic data. With more data, the antiproton to proton flux ratio can be updated with higher statistics and improved accuracy. This thesis has used data of the first ten years of operation up to May 2021. In figure 5.1(a), the final antiproton to proton flux ratio of this analysis is shown.

In figure 5.1(b), a linear fit in the antiproton to proton flux ratio with statistical uncertainty and correlated systematic uncertainty only is performed above 40 GV, this leads to a fitted slope  $k = (-1.44 \pm 0.42) \times 10^{-5} \text{ GV}^{-1}$ . Compared to the result in the previous AMS-02 publication [57] , the observed behavior keeps the same. The antiproton to proton ratio is relatively flat in the high rigidity range. No obvious falling trend is observed as is the case for the positron to electron flux ratio shown in the latest paper by the AMS-02 collaboration [80] . In order to study the ratio in even higher rigidity ranges, more data is required and better charge confusion separation is needed.

To check the consistency between the result of this analysis and the one published by the AMS-02 collaboration [80] , the antiproton to proton flux ratio is also determined in this analysis with the same data period, namely from May 2011 to Nov 2017. In figure 5.2, the antiproton to proton flux ratio of this analysis based on six and a half years of data is shown in comparison with the AMS-02 published result in the Physics Report that is obtained for



(a)



(b)

Figure 5.1: The time-averaged antiproton to proton flux ratio with the data collected from May 2011 to May 2021. a). Antiproton to proton flux ratio. The error bars are the total errors calculated from the quadratic sum of the statistical and the systematic errors; b). Linear fit above 40 GV on antiproton to proton flux ratio with statistical uncertainty and correlated systematic uncertainty only. The solid line shows the fit together with the 68% C.L. ranges of the fit parameters (shaded regions).

the same data period. The result of this analysis matches well the AMS-02 published result within the error bars except the first few points. Since the first three points significantly deviate, they are excluded in the time-dependent analysis.

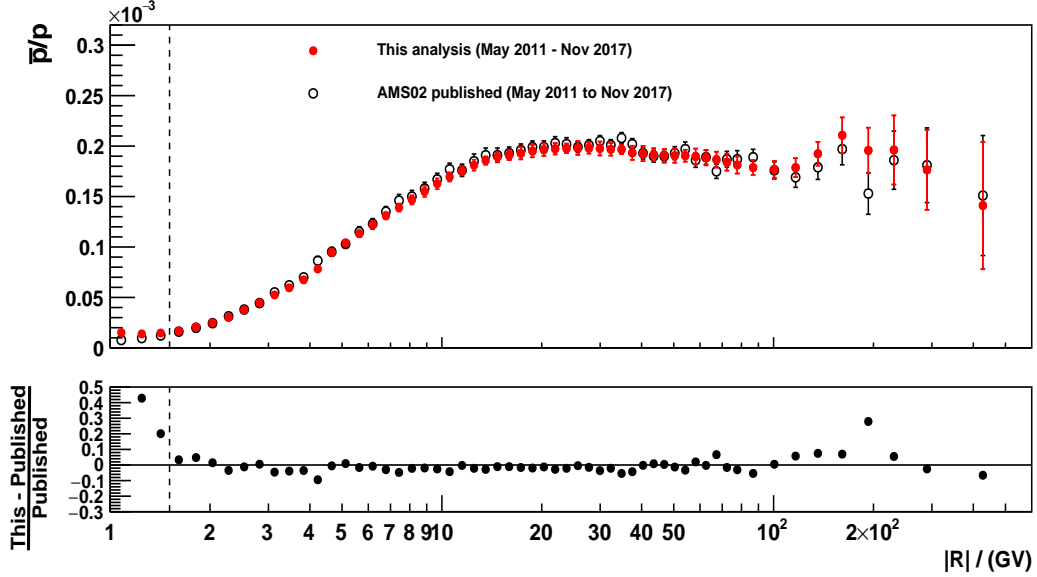


Figure 5.2: Comparison of the antiproton to proton flux ratio of this analysis to the AMS-02 published result in Physics Report [80] , for the same time interval of six and a half years. Both results agree well with each other within the error bars except the first few points. The statistic in the low rigidity range is highly subject to the geomagnetic cutoff as shown in figure 4.28. This could lead to a difference between the results. Therefore, the first three points (on the left of the dashed line) are excluded in the time-dependent analysis.

The breakdown of the total uncertainty into its statistical and systematic components is shown in figure 5.3. In the high rigidity range, the error is mainly dominated by the systematic error due to the background of charge confused protons and the limited separation power. In the intermediate rigidity range, the error is dominated by the systematic error due to the effective acceptance. In the low rigidity below 2 GV, the contributions from the statistical and the systematic uncertainties are at a similar level.

In figure 5.4, the comparison of the total systematic and the statistical uncertainties between this analysis and the result in Physics Report [80] is shown. Although the analyzed data-taking period in this analysis is longer, the statistics do not gain significantly due to the frequent change of the TTCS and the cuts used in this analysis are stricter. Therefore the two independent results give statistical uncertainty at the same level. The systematic uncertainties of the two independent results match in the most rigidity range. But in the high rigidity range, due to the different  $\Lambda_{CC}$ , the systematic uncertainties from the charge confusion, which is dominant in the high rigidity range, are different.

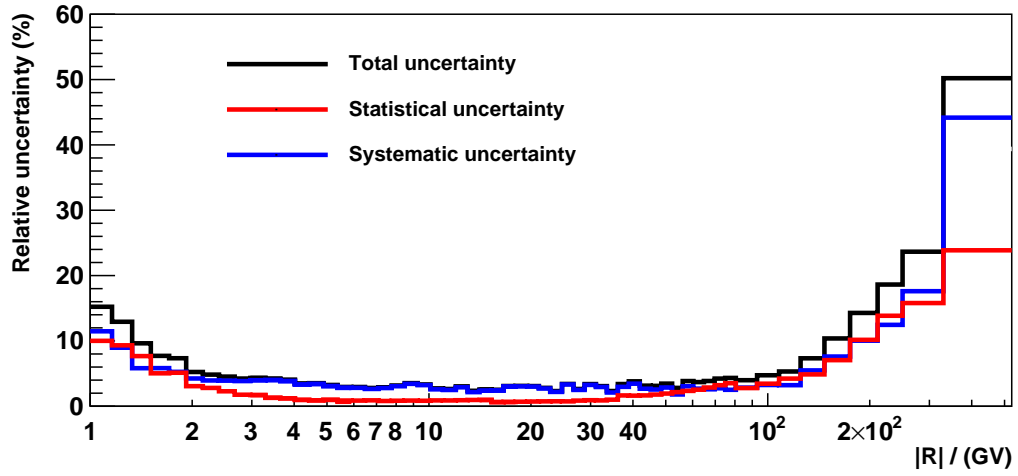


Figure 5.3: The uncertainty breakdown of the time-averaged antiproton to proton flux ratio in this analysis. In the highest rigidity bin, the systematic uncertainty is dominant due to the charge confused protons. In the low rigidity range, the statistical and systematic uncertainties are similar.

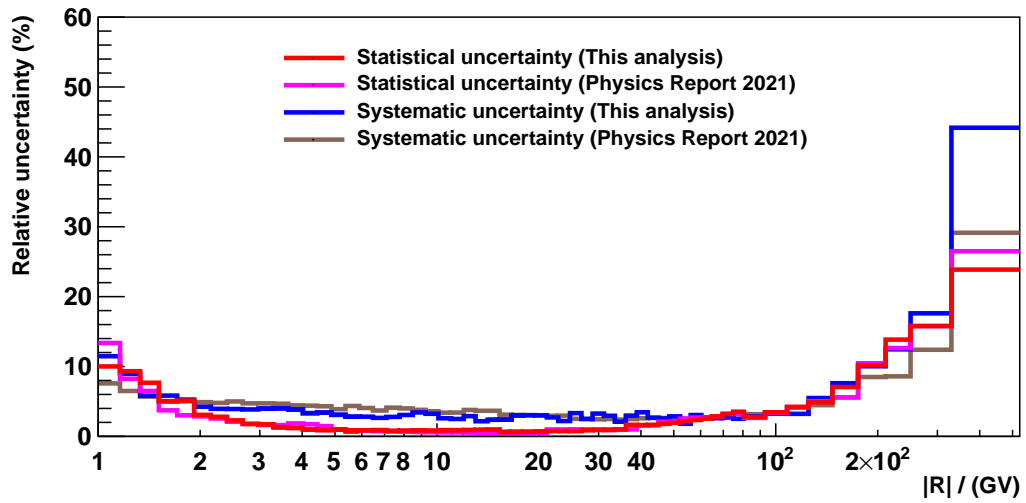


Figure 5.4: The statistical and systematic uncertainty comparison between this analysis and AMS-02 publication in Physics Report [80] .

## 5.2. Time Dependent Result

Apart from the time-averaged antiproton to proton flux ratio, the time-dependent antiproton to proton flux ratio is also calculated with the same strategy. For the time-dependent analysis, the antiproton to proton flux ratio is determined in six Bartels Rotations time bins. In total, 13 time-dependent antiproton to proton flux ratios are obtained from 1.51 GV to 18 GV. The first three rigidity bins from 1.0 to 1.51 GV in the time-averaged analysis are excluded since they deviate from the previous publication. The time-dependent antiproton to proton flux ratios for five out of the 13 rigidity bins are given in figure 5.5. The uncertainty bars in this figure are total time-dependent uncertainties, including the statistical uncertainty and the time-dependent systematic uncertainty. In this figure, the variation caused by the solar modulation is clearly visible.

One important observation is that with increasing rigidity, the solar modulation effect becomes weaker. In the first rigidity bin in figure 5.5, the flux ratio changes by a factor  $\sim 2$  between its minimum and maximum values, while at around 10 GV, the fluctuation only changes by around 20%.

A distinct trend is observed in the antiproton to proton flux ratio from 2011 to 2021. Below 4 GV, the antiproton to proton flux ratio shows a rising trend first and then gradually goes down, at last, relatively stabilized for a few years. The trend of antiproton to proton flux ratio in a complete solar cycle is shown in the solar modulation model [129]. A similar trend is predicted in the corresponding current sheet tile angle period. In figure 5.6, the comparison between this result and the model predicted from [130] is shown in an example rigidity bin of 1.92 to 2.4 GV. The observed behaviors match the solar modulation model in long time trend. Apart from the general trends observed over long periods of time, there are also a few fine time up and down structures. These fine time structures need to be studied in more detail with finer time bins. To achieve this, the cuts and selections in the low rigidity range need to be studied and optimized further dedicatedly.

The averaged relative uncertainty breakdown in time-dependent antiproton to proton flux ratio is shown in figure 5.7. Below 3 GV, the statistical uncertainty is dominant due to the limited statistics in six Bartels Rotations. Above 3 GV, the contributions of statistical and systematic uncertainty are at a similar level. For illustration, the relative total error breakdown in the rigidity bin of 1.92 - 2.4 GV is shown in figure 5.8. The time-dependent systematic uncertainty is relatively stable but with some jumps due to the change in detector configuration. The statistical uncertainty is fluctuating mostly due to the antiproton event counts.

Since the solar modulation affects all kinds of cosmic rays, the obtained time-dependent antiproton to proton flux ratio can be compared with other results. In figure 5.9, the antiproton to proton flux ratio in this analysis is shown together with the electron to positron flux ratio. The electron to positron flux ratio is taken from [111] and the result is consistent with a previous AMS-02 publication [47] but with a data extension. The electron to positron

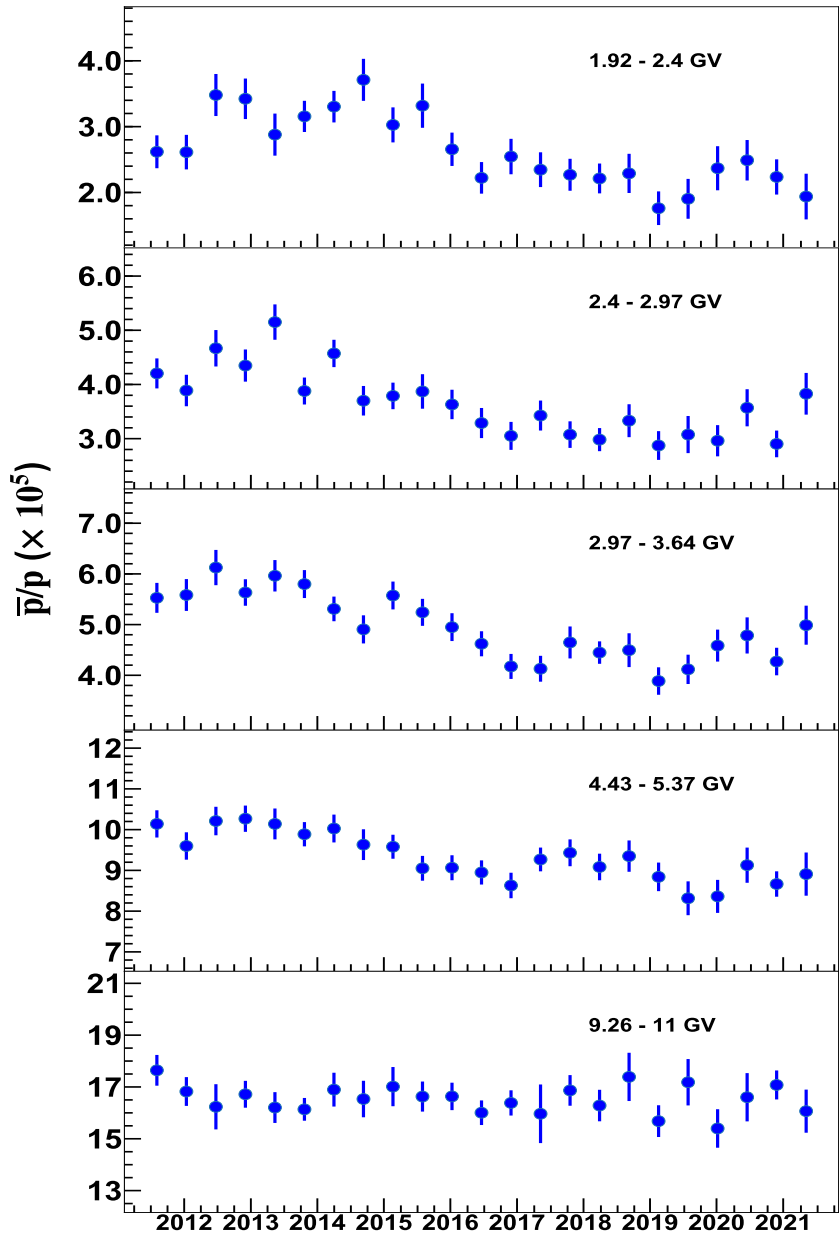


Figure 5.5: Time-dependent antiproton to proton flux ratios for five out of the 13 rigidity bins. The uncertainty bars in this figure are total time-dependent uncertainties, including the statistical uncertainty and the time-dependent systematic uncertainty. Distinct time variation structures are visible in these ratios.

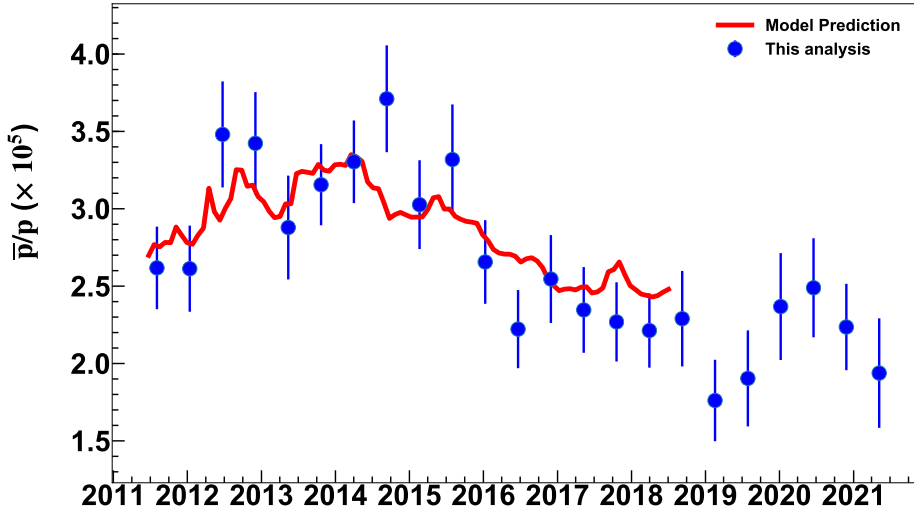


Figure 5.6: Time-dependent antiproton to proton flux ratio in 1.92 to 2.4 GV compared to model prediction. The modulation model is taken from [130] , but the prediction curve in this figure is given in a finer time resolution of one Bartel Rotation. Prediction data provided by O.P.M. Aslam. This work and model prediction show a similar trend, though detailed comparison needs finer time resolution in the measured time-dependent antiproton to proton flux ratio.

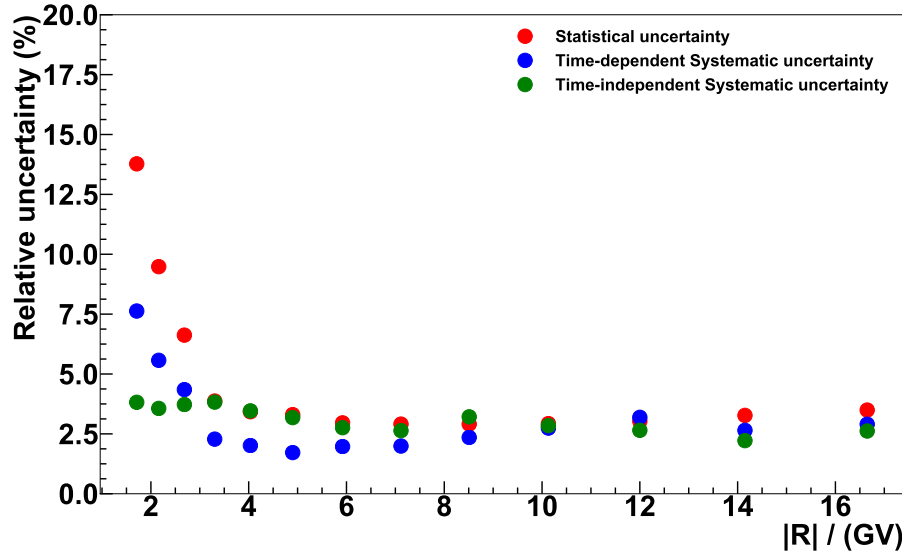


Figure 5.7: Averaged relative statistical and systematic uncertainties of the time-dependent antiproton to proton flux ratio. Below 3 GV, statistical uncertainty is dominant. Above 3 GV, the contributions of statistical and systematic uncertainty are at a similar level.

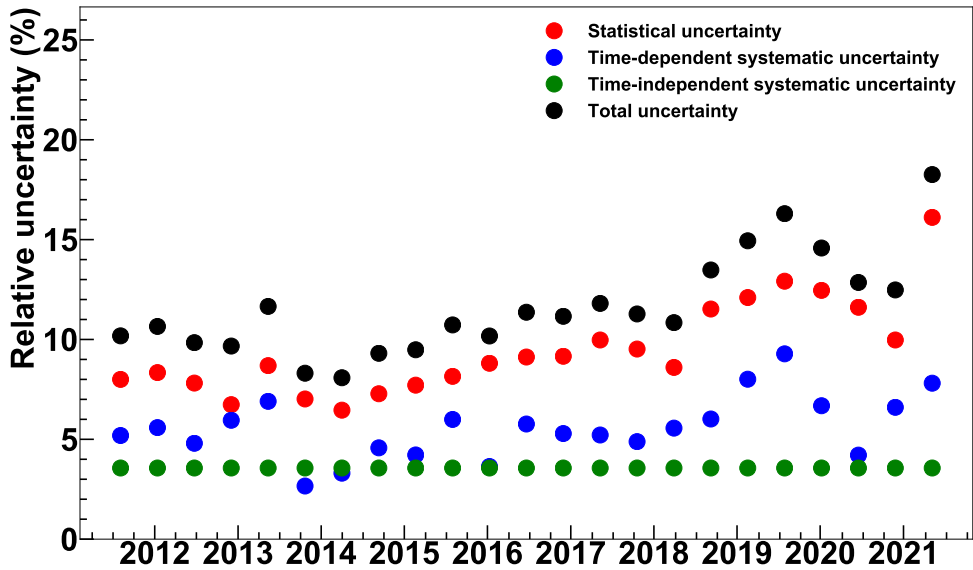


Figure 5.8: Breakdown of the total relative uncertainty of the antiproton to proton flux ratio into its statistical and systematic parts as a function of time for the rigidity bin of 1.92 to 2.4 GV. The statistical uncertainty corresponds to the antiproton events, which are subject to the solar modulation.

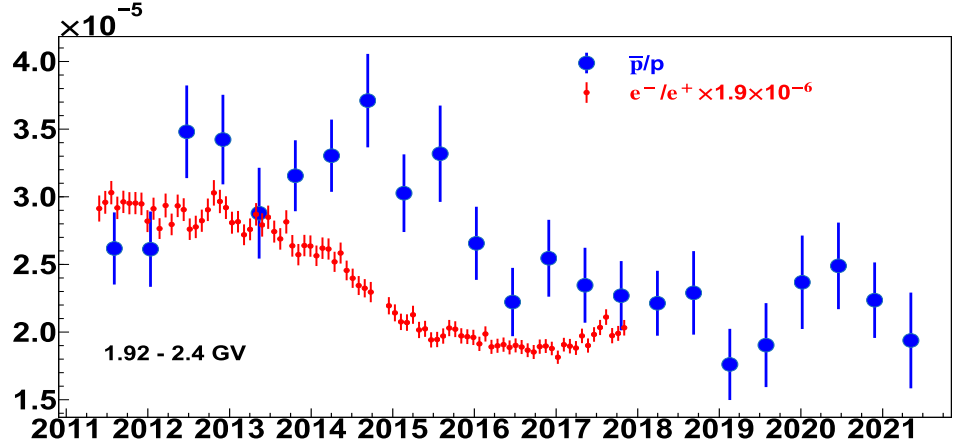
flux ratio is presented in its ECAL energy bins. To compare in the exact same rigidity bin as used for the antiproton to proton flux ratio, the electron and positron fluxes are fitted with a power-law modulated according to the force-field approximation, then integrated over the rigidity bin used for the antiproton to proton flux ratio and finally the electron to positron flux ratio in antiproton to proton flux ratio bins can be obtained. Due to the charge sign difference, the two flux ratios are shown in negatively charged particles over positively charged particles. The normalization of the electron to positron flux ratio is based on the first two years of data to make sure the mean of the electron to positron flux ratio is the same as the mean of the antiproton to proton flux ratio.

By comparing the antiproton to proton flux ratio and the electron to positron flux ratio, the first observation is that the time variation effects in both flux ratios are decreasing with increasing rigidity and this observation is expected.

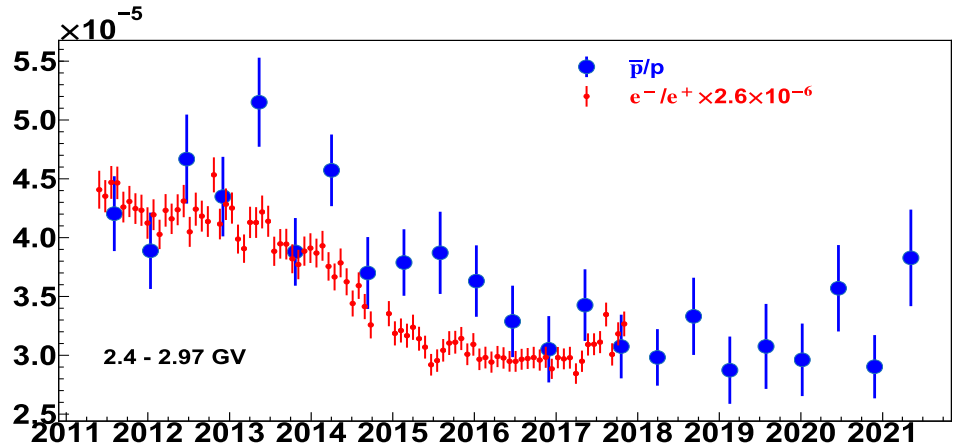
The second observation is that the time variation trend of the antiproton to proton flux ratio is different from the electron to positron flux ratio in the low rigidity range. For example, below 3 GV, the antiproton to proton flux ratio goes up first and then drops down to the minimum, at last gradually rebounds. While the electron to positron flux ratio keeps relatively stable first and then goes down, at last rebounds from 2017. The difference between these two flux ratios gradually disappears as the rigidity increases, and the trend

of these two ratios becomes similar in rigidity ranges higher than 6 GV.

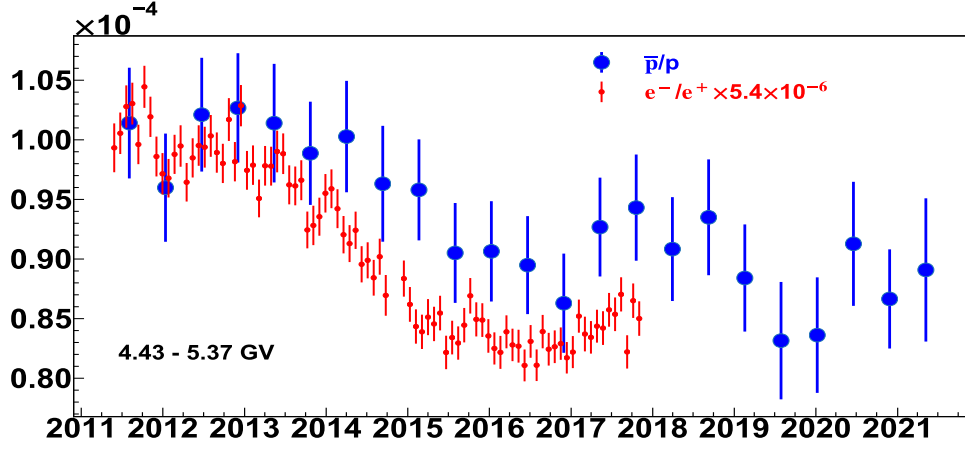
For the solar modulation modeling, the Local Interstellar Spectra (LIS) are important inputs. The LIS for the antiproton are different than the ones for the positron [130] . Therefore, this could lead to a difference between the antiproton to proton flux ratio trend and the electron to positron flux ratio trend. Another important difference is the mass difference. The antiproton and the proton have much larger mass than the electron and the positron. Due to the drift effect, this mass difference has a higher impact in the low rigidity range resulting in differences between the flux ratio of the antiproton to proton and the one of the electron to positron.



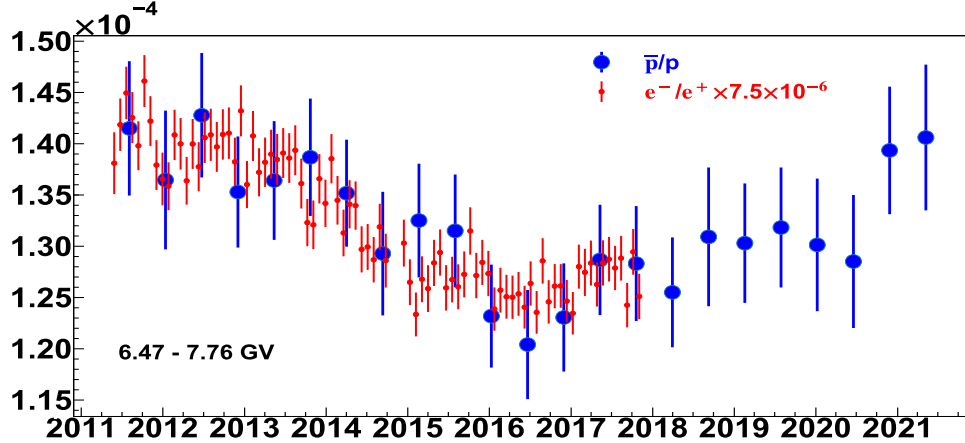
(a)



(b)



(c)



(d)

Figure 5.9: Comparison between the antiproton to proton flux ratio (blue) and the electron to positron flux ratio (red) over time in four rigidity bins: a) 1.92-2.4 GV b) 2.4-2.97 GV c) 4.43-5.37 GV and d) 6.47-7.76 GV. The error bars are the total errors calculated from the quadratic sum of the statistical errors and the total systematic errors. The scaling of the electron to positron flux ratio is based on the first two years of data to make sure the mean of the electron to positron flux ratio is the same as the mean of the antiproton to proton flux ratio.

# CHAPTER 6

## SUMMARY

In this thesis, the time-averaged antiproton to proton flux ratio as a function of rigidity is presented for up to 525 GV using ten years of AMS-02 cosmic ray data providing the most accurate and up to date measurement of this kind. This unprecedented accuracy provides a probe for us to understand the origin of cosmic ray antiprotons. The antiproton to proton flux ratio in the high rigidity range shows a relatively flat trend according to previous AMS-02 publication based on four years of data [57] , instead of a falling trend predicted by the secondary production models [25, 26] . This observation doesn't change in this analysis result with the latest ten years of data. This analysis is an independent result of the AMS-02 Physics Report result in [80] , which also presents the antiproton to proton flux ratio up to 525 GV.

Apart from the time-averaged antiproton to proton flux ratio, the time-dependent antiproton to proton flux ratio in every six Bartels Rotations time bins is presented in this thesis. From 1.51 GV to 18 GV, the time-dependent antiproton to proton flux ratios are given in 13 rigidity bins. The rigidity bins are merged in every two rigidity bins of the time-averaged analysis to increase the statistics.

The first observation in the time-dependent antiproton to proton flux ratio is that with increasing rigidity, the solar modulation effect becomes weaker. The antiproton to proton flux ratio shows a distinct time structure for up to around 10 GV. The data was collected from May 2011 to May 2021, which covers eight years in the solar cycle 24 and two years in the solar cycle 25. During this ten-year period, the behavior of the antiproton to proton flux ratio shows a rising trend first, then goes down reaching a minimum, and finally it gradually rises. The importance of these observations is crucial as they can be used for the evaluation of the solar modulation models [129, 130] .

The second observation in the time-dependent antiproton to proton flux ratio derives from the comparison between the antiproton to proton flux ratio and the electron to positron flux ratio. The antiproton to proton flux ratio is different from the electron to positron flux ratio in the rigidity range below 3 GV. This difference gradually fades away with increasing rigidity and above 6 GV it almost disappears and the two flux ratios show a similar trend.

The different behaviors could be due to the different LIS of antiprotons and positrons in the low rigidity range. In addition, the mass difference between antiproton (proton) and positron (electron) also plays an important role in the low rigidity range.

The AMS-02 will continue to collect data throughout the lifetime of the ISS, which is estimated to last until 2030. The increased statistics will reduce the statistical error further and give a more precise measurement. With the data collected in the future, the time variation effects in a complete 11 years solar cycle can be obtained. Moreover, studies on the antiproton to proton flux ratio in finer than six Bartels Rotations time bins will be made possible providing important insight on possible fine time structures present.

Preparations for the successor of the AMS-02 experiment are in progress. The AMS-100 [131] , a next-generation magnetic spectrometer in space is planned to be placed on the Lagrange point L2 of the Earth-Sun system in around 2039. The AMS-100 can provide  $100\ m^2sr$  acceptance and allow a measurement of the antiproton to proton flux ratio up to 10 TV. For the time-dependent analysis, the AMS-100 can continue the study of the solar modulation on the cosmic antiprotons for decades.

## Appendix A

# Input variables for charge confusion estimator

Apart from the four variables shown in section 4.2, the full list of the remaining twelve input variables used for the training of the charge confusion estimator  $\Lambda_{CC}$  is given in this appendix. Nine of them are constructed from the Tracker, two from the TOF, and one from the TRD.

### 1. TOF Charge

For the TOF subdetector, the charge measurements are used for the training.  $Q_{\text{LowTOF}}$  and  $Q_{\text{UppTOF}}$  are the TOF charge measurements from the lower TOF and the upper TOF. In figure A.1, the distributions of the  $Q_{\text{LowTOF}}$  and  $Q_{\text{UppTOF}}$  are shown.

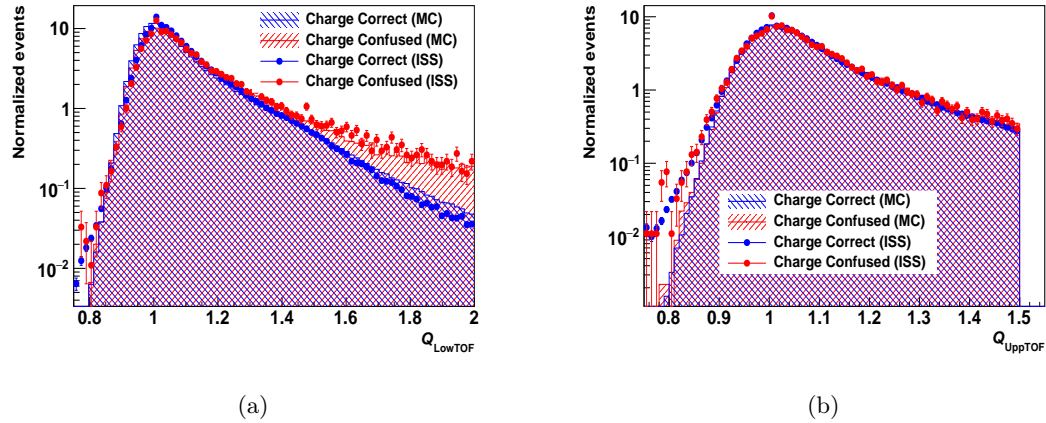


Figure A.1: Distributions for a)  $Q_{\text{LowTOF}}$  and b)  $Q_{\text{UppTOF}}$  in the rigidity bin of 330 to 525 GV in fullspan tracker pattern. The points represent the observed ISS data and the histograms show the expected number of events from MC simulation for the charge correct antiprotons (blue) and the charge confused protons (red).

## 2. Rigidity Asymmetry and Matching

The rigidity is reconstructed from the tracker measurements. Depending on the number of tracker layers used for this reconstruction, different rigidity values are obtained. Therefore, the asymmetry and matching variables can be constructed and used as inputs for the training.  $\delta_{\mathbf{R}_{L9}}$  and  $\Gamma_{\text{Central}}$  their definitions are given below:

$$\delta_{\mathbf{R}_{L9}} = \frac{R_{\text{Inner+L9}} - R_{\text{Inner}}}{R_{\text{Inner+L9}} + R_{\text{Inner}}}$$

$$\Gamma_{\text{Central}} = \left[ \left( \frac{1}{R_{\text{UppInner}}} \right) - \left( \frac{1}{R_{\text{LowInner}}} \right) \right] \cdot 100 \cdot \frac{R}{|R|}$$

where the  $R_{\text{Inner}}$  and  $R_{\text{Inner+L9}}$  are the rigidities constructed from the inner tracker layers and the inner tracker layers plus layer 9 respectively,  $R_{\text{UppInner}}$  and  $R_{\text{LowInner}}$  are constructed from the upper half of the inner tracker layers and the lower half of the inner tracker layers respectively.

In figure A.2, the distributions of the two variables are shown.

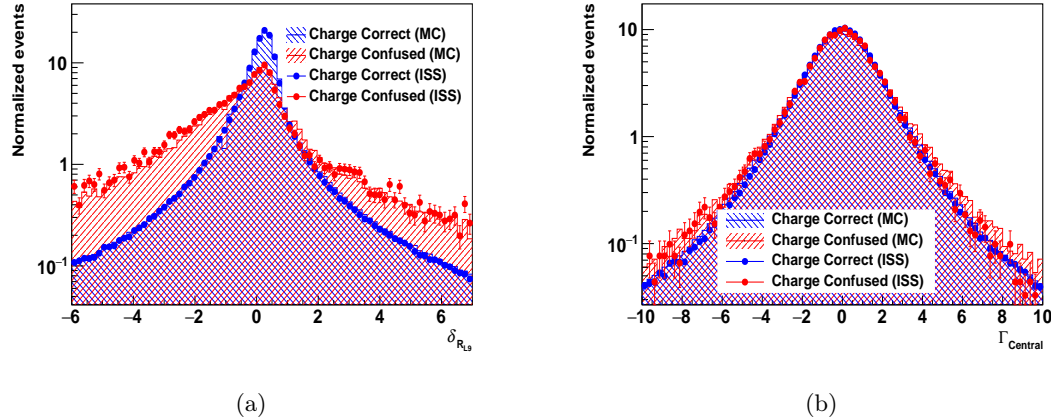


Figure A.2: Distributions for a)  $\delta_{\mathbf{R}_{L9}}$  b)  $\Gamma_{\text{Central}}$  in the rigidity bin of 330 to 525 GV in fullspan tracker pattern. The points represent the observed ISS data and the histograms show the expected number of events from MC simulation for the charge correct antiprotons (blue) and the charge confused protons (red).

### 3. Tracker Fit $\chi^2$

The tracker track fit quality provides important information for the charge confusion estimator. Due to the interaction, the charge confused events have worse tracker fit quality. Therefore, the  $\chi^2$  of the fit can be used as an input for the training. In total, four variables related to  $\chi^2$  are used: the  $\log \chi^2$  of the tracker track fit for both directions X and Y ( $\chi^2_X$  and  $\chi^2_Y$ ) and the  $\log \chi^2$  of the inner tracker track fit for X and Y ( $\chi^2_{X_{\text{Inner}}}$  and  $\chi^2_{Y_{\text{Inner}}}$ ). In figure A.3, the distributions of these four variables are shown.

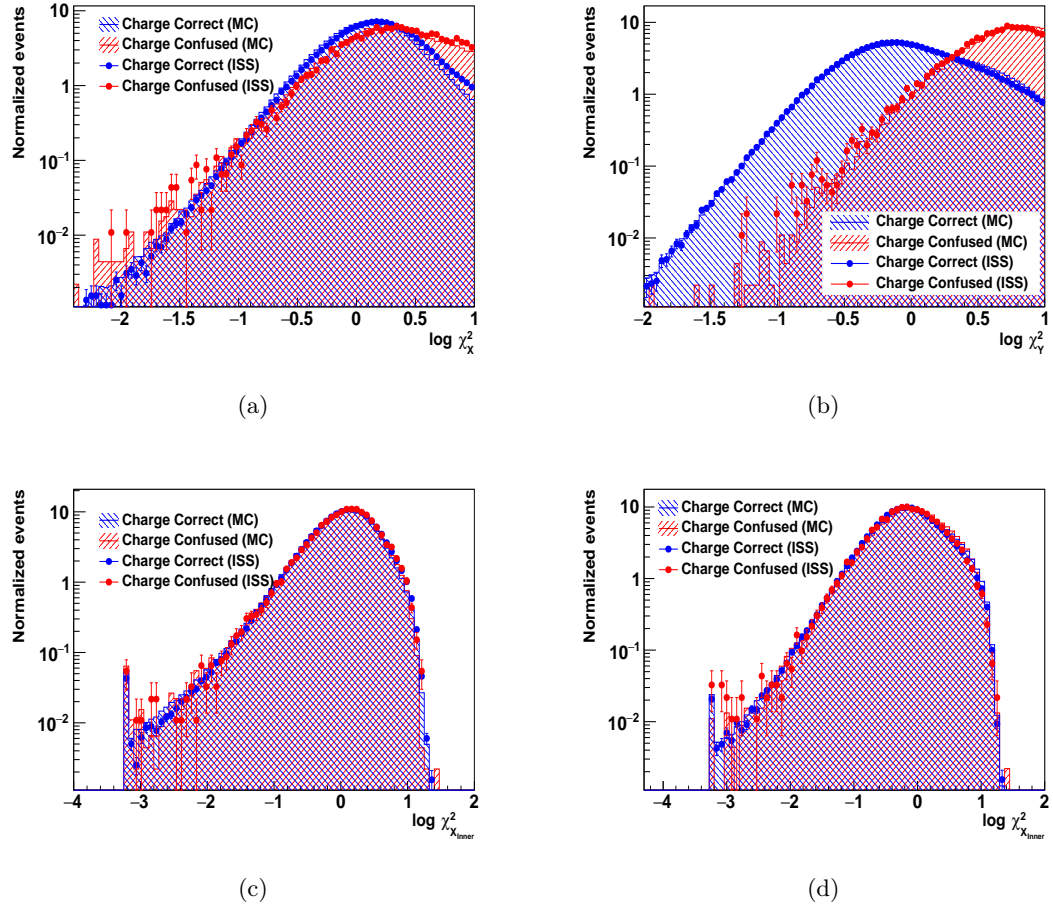


Figure A.3: Distributions for a)  $\log \chi^2_X$  b)  $\log \chi^2_Y$  c)  $\log \chi^2_{X_{\text{Inner}}}$  d)  $\log \chi^2_{Y_{\text{Inner}}}$  in the rigidity bin of 330 to 525 GV in fullspan tracker pattern. The points represent the observed ISS data and the histograms show the expected number of events from MC simulation for the charge correct antiprotons (blue) and the charge confused protons (red).

#### 4. Tracker Charge

Due to the interaction of the incoming particle with the detector material, the tracker charge measurement could contain information of charge confusion. Therefore, this is added to the training variables list. The  $Q_{L9}$  and  $Q_{L78}$  are the two variables relevant to this.  $Q_{L9}$  is the tracker charge measurement from layer 9.  $Q_{L78}$  is the mean value of the tracker charge measurement from layers 7 and 8. In figure A.4, the distributions of the two variables are shown.

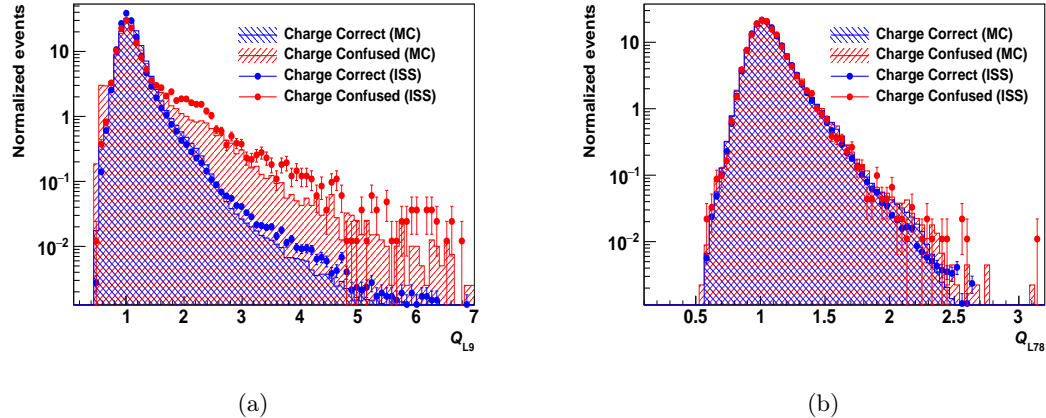


Figure A.4: Distributions for a)  $Q_{L9}$  b)  $Q_{L78}$  in the rigidity bin of 330 to 525 GV in fullspan tracker pattern. The points represent the observed ISS data and the histograms show the expected number of events from MC simulation for the charge correct antiprotons (blue) and the charge confused protons (red).

## 5. Charge Asymmetry

The tracker charge asymmetry also provides information for the charge confusion estimator.  $\delta_Q$  is the asymmetry of the tracker charge measurements and its definition is given below:

$$\delta_Q = \frac{Q_{L58} - Q_{L24}}{Q_{\text{Inner}}}$$

where  $Q_{L58}$  is the mean value of the tracker charge from layers 5 and 8.  $Q_{L24}$  is the mean value of the tracker charge from layers 2 and 4 and finally  $Q_{\text{Inner}}$  is the tracker charge from the inner tracker.

In figure A.5, the distributions of the  $\delta_Q$  is shown. The separation power in this plot is not very obvious but it depends on the rigidity bin and tracker patterns. In other rigidity bin and tracker patterns it is useful, therefore this variable is included.

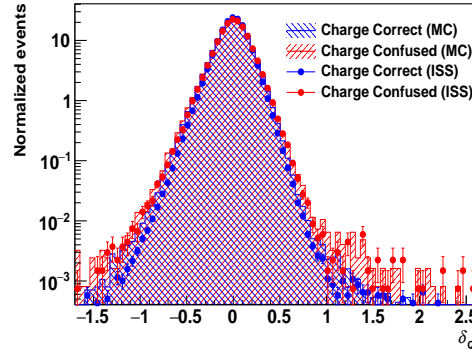


Figure A.5: Distributions for  $\delta_Q$  in the rigidity bin of 330 to 525 GV in Inner+L1 tracker pattern. The points represent the observed ISS data and the histograms show the expected number of events from MC simulation for the charge correct antiprotons (blue) and the charge confused protons (red).

## 6. TRDLikelihood

The last variable is the  $\Lambda_{\text{TRD}}$ . Because of the potential particle interactions in the TRD volume which result in charge confused events, the  $\Lambda_{\text{TRD}}$  provides the separation power between charge correct antiprotons and charge confused protons. In figure A.6, the distribution of the  $\Lambda_{\text{TRD}}$  is shown.

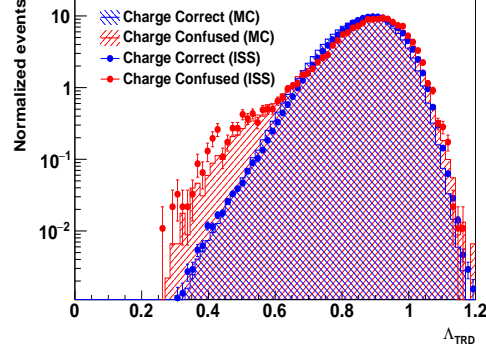


Figure A.6: Distributions for  $\Lambda_{\text{TRD}}$  in the rigidity bin of 330 to 525 GV in fullspan tracker pattern. The points represent the observed ISS data and the histograms show the expected number of events from MC simulation for the charge correct antiprotons (blue) and the charge confused protons (red).

## Appendix B

# Table of Results

In table B.1, the result of the time-averaged antiproton to proton flux ratio is given. Rigidity is the absolute rigidity at the top of the AMS-02 detector,  $N_{\bar{p}}$  is the number of antiprotons observed in each rigidity bin rounded to the nearest integer,  $\frac{\Phi_{\bar{p}}}{\Phi_p}$  is the value of the antiproton to proton flux ratio,  $\sigma_{\text{stat}}$  is the total statistical uncertainty and  $\sigma_{\text{syst}}$  is the total systematic uncertainty.

In tables B.2 to B.24, the results of the time-dependent antiproton to proton flux ratio are shown. These 23 tables show the antiproton to proton flux ratio in 23 six Bartel Rotations time intervals, from Bartels Rotation 2426 to 2564. In these tables, Rigidity is the absolute rigidity at the top of the AMS-02 detector,  $N_{\bar{p}}$  is the number of antiprotons observed in each rigidity bin rounded to the nearest integer,  $\frac{\Phi_{\bar{p}}}{\Phi_p}$  is the value of the antiproton to proton flux ratio,  $\sigma_{\text{stat}}$  is the total statistical uncertainty and  $\sigma_{\text{syst}}$  is the total systematic uncertainty.

Rigidity (GV)	$N_{\bar{p}}$	$\frac{\Phi_{\bar{p}}}{\Phi_p}$	$\sigma_{\text{stat}}$	$\sigma_{\text{syst}}$	Rigidity (GV)	$N_{\bar{p}}$	$\frac{\Phi_{\bar{p}}}{\Phi_p}$	$\sigma_{\text{stat}}$	$\sigma_{\text{syst}}$		
1.00 — 1.16	72	(1.35	0.13	0.15)	$\times 10^{-5}$	1.16 — 1.33	145	(1.26	0.12	0.11)	$\times 10^{-5}$
1.33 — 1.51	257	(1.39	0.11	0.08)	$\times 10^{-5}$	1.51 — 1.71	487	(1.60	0.08	0.09)	$\times 10^{-5}$
1.71 — 1.92	839	(1.97	0.10	0.10)	$\times 10^{-5}$	1.92 — 2.15	1493	(2.33	0.07	0.10)	$\times 10^{-5}$
2.15 — 2.40	2387	(2.86	0.08	0.11)	$\times 10^{-5}$	2.40 — 2.67	3617	(3.56	0.08	0.14)	$\times 10^{-5}$
2.67 — 2.97	5282	(4.22	0.07	0.16)	$\times 10^{-5}$	2.97 — 3.29	6921	(4.97	0.08	0.19)	$\times 10^{-5}$
3.29 — 3.64	9241	(5.68	0.07	0.23)	$\times 10^{-5}$	3.64 — 4.02	11400	(6.50	0.08	0.25)	$\times 10^{-5}$
4.02 — 4.43	13969	(7.61	0.08	0.25)	$\times 10^{-5}$	4.43 — 4.88	10120	(8.75	0.08	0.30)	$\times 10^{-5}$
4.88 — 5.37	10378	(9.72	0.09	0.30)	$\times 10^{-5}$	5.37 — 5.90	11109	(1.07	0.01	0.03)	$\times 10^{-4}$
5.90 — 6.47	11704	(1.16	0.01	0.03)	$\times 10^{-4}$	6.47 — 7.09	12271	(1.25	0.01	0.03)	$\times 10^{-4}$
7.09 — 7.76	12629	(1.33	0.01	0.04)	$\times 10^{-4}$	7.76 — 8.48	12669	(1.42	0.01	0.04)	$\times 10^{-4}$
8.48 — 9.26	12552	(1.50	0.01	0.05)	$\times 10^{-4}$	9.26 — 10.1	12325	(1.59	0.01	0.05)	$\times 10^{-4}$
10.1 — 11.0	11982	(1.66	0.01	0.04)	$\times 10^{-4}$	11.0 — 12.0	11890	(1.73	0.02	0.04)	$\times 10^{-4}$
12.0 — 13.0	10799	(1.79	0.02	0.05)	$\times 10^{-4}$	13.0 — 14.1	10832	(1.84	0.02	0.04)	$\times 10^{-4}$
14.1 — 15.3	10809	(1.88	0.02	0.04)	$\times 10^{-4}$	15.3 — 16.6	30786	(1.91	0.01	0.04)	$\times 10^{-4}$
16.6 — 18.0	27633	(1.93	0.01	0.05)	$\times 10^{-4}$	18.0 — 19.5	24262	(1.95	0.01	0.06)	$\times 10^{-4}$
19.5 — 21.1	21967	(1.97	0.01	0.06)	$\times 10^{-4}$	21.1 — 22.8	20127	(1.98	0.01	0.05)	$\times 10^{-4}$
22.8 — 24.7	19814	(1.98	0.02	0.04)	$\times 10^{-4}$	24.7 — 26.7	18383	(1.98	0.01	0.06)	$\times 10^{-4}$
26.7 — 28.8	17107	(1.98	0.02	0.05)	$\times 10^{-4}$	28.8 — 31.1	16345	(1.98	0.02	0.06)	$\times 10^{-4}$
31.1 — 33.5	14786	(1.98	0.02	0.06)	$\times 10^{-4}$	33.5 — 36.1	13835	(1.98	0.02	0.04)	$\times 10^{-4}$
36.1 — 38.9	5674	(1.95	0.03	0.06)	$\times 10^{-4}$	38.9 — 41.9	4830	(1.93	0.03	0.06)	$\times 10^{-4}$
41.9 — 45.1	4039	(1.92	0.03	0.05)	$\times 10^{-4}$	45.1 — 48.5	3429	(1.91	0.03	0.05)	$\times 10^{-4}$
48.5 — 52.5	2993	(1.92	0.04	0.05)	$\times 10^{-4}$	52.2 — 56.1	2547	(1.92	0.04	0.03)	$\times 10^{-4}$
56.1 — 60.3	2223	(1.92	0.05	0.06)	$\times 10^{-4}$	60.3 — 64.8	1918	(1.91	0.05	0.05)	$\times 10^{-4}$
64.8 — 69.7	1664	(1.88	0.05	0.05)	$\times 10^{-4}$	69.7 — 74.9	1424	(1.85	0.06	0.05)	$\times 10^{-4}$
74.9 — 80.5	1233	(1.81	0.06	0.05)	$\times 10^{-4}$	80.5 — 93.0	2005	(1.76	0.05	0.05)	$\times 10^{-4}$
93.0 — 108	1596	(1.72	0.06	0.05)	$\times 10^{-4}$	108 — 125	1214	(1.76	0.07	0.06)	$\times 10^{-4}$
125 — 147	1091	(1.93	0.09	0.10)	$\times 10^{-4}$	147 — 175	402	(2.00	0.14	0.15)	$\times 10^{-4}$
175 — 211	143	(1.91	0.19	0.19)	$\times 10^{-4}$	211 — 259	100	(2.05	0.28	0.26)	$\times 10^{-4}$
259 — 330	102	(1.96	0.30	0.34)	$\times 10^{-4}$	330 — 525	85	(1.82	0.43	0.80)	$\times 10^{-4}$

Table B.1: The time-averaged antiproton to proton flux ratio for rigidity from 1.0 to 525 GV.

<b>Rigidity (GV)</b>	$N_{\bar{p}}$	$\frac{\Phi_{\bar{p}}}{\Phi_p}$	$\sigma_{\text{stat}}$	$\sigma_{\text{syst}}$	<b>Rigidity (GV)</b>	$N_{\bar{p}}$	$\frac{\Phi_{\bar{p}}}{\Phi_p}$	$\sigma_{\text{stat}}$	$\sigma_{\text{syst}}$
1.51 — 1.92	87	(1.90 0.23 0.20) $\times 10^{-5}$			6.47 — 7.76	1156	(1.41 0.04 0.05) $\times 10^{-4}$		
1.92 — 2.40	226	(2.61 0.21 0.16) $\times 10^{-5}$			7.76 — 9.26	1142	(1.58 0.04 0.06) $\times 10^{-4}$		
2.40 — 2.97	509	(4.20 0.23 0.22) $\times 10^{-5}$			9.26 — 11.0	1148	(1.76 0.05 0.06) $\times 10^{-4}$		
2.97 — 3.64	825	(5.52 0.23 0.28) $\times 10^{-5}$			11.0 — 13.0	996	(1.81 0.05 0.06) $\times 10^{-4}$		
3.64 — 4.43	997	(9.15 0.27 0.35) $\times 10^{-5}$			13.0 — 15.3	864	(1.85 0.06 0.06) $\times 10^{-4}$		
4.43 — 5.37	937	(10.1 0.30 0.35) $\times 10^{-5}$			15.3 — 18.0	744	(1.84 0.06 0.06) $\times 10^{-4}$		
5.37 — 6.47	1152	(1.29 0.04 0.05) $\times 10^{-4}$							

Table B.2: For Bartels Rotations 2426 to 2432 (May 15, 2011 – Oct 24, 2011), the observed antiproton numbers and the antiproton to proton flux ratio with its statistical and systematic uncertainties.

<b>Rigidity (GV)</b>	$N_{\bar{p}}$	$\frac{\Phi_{\bar{p}}}{\Phi_p}$	$\sigma_{\text{stat}}$	$\sigma_{\text{syst}}$	<b>Rigidity (GV)</b>	$N_{\bar{p}}$	$\frac{\Phi_{\bar{p}}}{\Phi_p}$	$\sigma_{\text{stat}}$	$\sigma_{\text{syst}}$
1.51 — 1.92	84	(1.75 0.22 0.16) $\times 10^{-5}$			6.47 — 7.76	1287	(1.36 0.03 0.06) $\times 10^{-4}$		
1.92 — 2.40	234	(2.61 0.22 0.17) $\times 10^{-5}$			7.76 — 9.26	1264	(1.51 0.04 0.07) $\times 10^{-4}$		
2.40 — 2.97	488	(3.89 0.23 0.23) $\times 10^{-5}$			9.26 — 11.0	1275	(1.68 0.04 0.06) $\times 10^{-4}$		
2.97 — 3.64	869	(5.58 0.23 0.30) $\times 10^{-5}$			11.0 — 13.0	1140	(1.76 0.05 0.06) $\times 10^{-4}$		
3.64 — 4.43	948	(8.04 0.25 0.32) $\times 10^{-5}$			13.0 — 15.3	1042	(1.91 0.05 0.09) $\times 10^{-4}$		
4.43 — 5.37	986	(9.59 0.28 0.35) $\times 10^{-5}$			15.3 — 18.0	941	(1.98 0.06 0.07) $\times 10^{-4}$		
5.37 — 6.47	1167	(1.15 0.03 0.04) $\times 10^{-4}$							

Table B.3: For Bartels Rotations 2432 to 2438 (Oct 24, 2011 – Apr 03, 2012), the observed antiproton numbers and the antiproton to proton flux ratio with its statistical and systematic uncertainties.

<b>Rigidity (GV)</b>	$N_{\bar{p}}$	$\frac{\Phi_{\bar{p}}}{\Phi_p}$	$\sigma_{\text{stat}}$	$\sigma_{\text{syst}}$	<b>Rigidity (GV)</b>	$N_{\bar{p}}$	$\frac{\Phi_{\bar{p}}}{\Phi_p}$	$\sigma_{\text{stat}}$	$\sigma_{\text{syst}}$
1.51 — 1.92	92	(2.75 0.31 0.20) $\times 10^{-5}$			6.47 — 7.76	1277	(1.42 0.04 0.05) $\times 10^{-4}$		
1.92 — 2.40	242	(3.48 0.27 0.21) $\times 10^{-5}$			7.76 — 9.26	1265	(1.59 0.04 0.07) $\times 10^{-4}$		
2.40 — 2.97	491	(4.67 0.26 0.27) $\times 10^{-5}$			9.26 — 11.0	1170	(1.62 0.04 0.08) $\times 10^{-4}$		
2.97 — 3.64	841	(6.12 0.25 0.33) $\times 10^{-5}$			11.0 — 13.0	1131	(1.83 0.05 0.07) $\times 10^{-4}$		
3.64 — 4.43	928	(8.22 0.25 0.39) $\times 10^{-5}$			13.0 — 15.3	935	(1.78 0.05 0.05) $\times 10^{-4}$		
4.43 — 5.37	1011	(10.2 0.29 0.37) $\times 10^{-5}$			15.3 — 18.0	940	(2.01 0.06 0.07) $\times 10^{-4}$		
5.37 — 6.47	1184	(1.23 0.03 0.04) $\times 10^{-4}$							

Table B.4: For Bartels Rotations 2438 to 2444 (Apr 03, 2012 – Sep 12, 2012), the observed antiproton numbers and the antiproton to proton flux ratio with its statistical and systematic uncertainties.

<b>Rigidity (GV)</b>	$N_{\bar{p}}$	$\frac{\Phi_{\bar{p}}}{\Phi_p}$	$\sigma_{\text{stat}}$	$\sigma_{\text{syst}}$	<b>Rigidity (GV)</b>	$N_{\bar{p}}$	$\frac{\Phi_{\bar{p}}}{\Phi_p}$	$\sigma_{\text{stat}}$	$\sigma_{\text{syst}}$
1.51 — 1.92	143	(2.77 0.24 0.15) $\times 10^{-5}$			6.47 — 7.76	1355	(1.35 0.03 0.04) $\times 10^{-4}$		
1.92 — 2.40	331	(3.42 0.23 0.23) $\times 10^{-5}$			7.76 — 9.26	1409	(1.60 0.04 0.06) $\times 10^{-4}$		
2.40 — 2.97	592	(4.34 0.22 0.25) $\times 10^{-5}$			9.26 — 11.0	1322	(1.67 0.04 0.06) $\times 10^{-4}$		
2.97 — 3.64	955	(5.63 0.21 0.27) $\times 10^{-5}$			11.0 — 13.0	1213	(1.81 0.05 0.09) $\times 10^{-4}$		
3.64 — 4.43	1121	(8.65 0.24 0.33) $\times 10^{-5}$			13.0 — 15.3	1114	(1.97 0.05 0.09) $\times 10^{-4}$		
4.43 — 5.37	1149	(10.2 0.27 0.36) $\times 10^{-5}$			15.3 — 18.0	951	(1.95 0.06 0.07) $\times 10^{-4}$		
5.37 — 6.47	1302	(1.19 0.03 0.04) $\times 10^{-4}$							

Table B.5: For Bartels Rotations 2444 to 2450 (Sep 12, 2012 – Feb 21, 2013), the observed antiproton numbers and the antiproton to proton flux ratio with its statistical and systematic uncertainties.

<b>Rigidity (GV)</b>	$N_{\bar{p}}$	$\frac{\Phi_{\bar{p}}}{\Phi_p}$	$\sigma_{\text{stat}}$	$\sigma_{\text{syst}}$	<b>Rigidity (GV)</b>	$N_{\bar{p}}$	$\frac{\Phi_{\bar{p}}}{\Phi_p}$	$\sigma_{\text{stat}}$	$\sigma_{\text{syst}}$
1.51 — 1.92	86	(2.64 0.31 0.20) $\times 10^{-5}$			6.47 — 7.76	1308	(1.36 0.03 0.05) $\times 10^{-4}$		
1.92 — 2.40	203	(2.88 0.25 0.22) $\times 10^{-5}$			7.76 — 9.26	1269	(1.49 0.04 0.05) $\times 10^{-4}$		
2.40 — 2.97	561	(5.15 0.26 0.27) $\times 10^{-5}$			9.26 — 11.0	1247	(1.62 0.04 0.06) $\times 10^{-4}$		
2.97 — 3.64	857	(5.96 0.25 0.29) $\times 10^{-5}$			11.0 — 13.0	1184	(1.81 0.05 0.09) $\times 10^{-4}$		
3.64 — 4.43	972	(8.17 0.24 0.32) $\times 10^{-5}$			13.0 — 15.3	1010	(1.82 0.05 0.08) $\times 10^{-4}$		
4.43 — 5.37	1063	(10.1 0.28 0.40) $\times 10^{-5}$			15.3 — 18.0	960	(2.00 0.06 0.06) $\times 10^{-4}$		
5.37 — 6.47	1200	(1.16 0.03 0.04) $\times 10^{-4}$							

Table B.6: For Bartels Rotations 2450 to 2456 (Feb 21, 2013 – Aug 02, 2013), the observed antiproton numbers and the antiproton to proton flux ratio with its statistical and systematic uncertainties.

<b>Rigidity (GV)</b>	$N_{\bar{p}}$	$\frac{\Phi_{\bar{p}}}{\Phi_p}$	$\sigma_{\text{stat}}$	$\sigma_{\text{syst}}$	<b>Rigidity (GV)</b>	$N_{\bar{p}}$	$\frac{\Phi_{\bar{p}}}{\Phi_p}$	$\sigma_{\text{stat}}$	$\sigma_{\text{syst}}$
1.51 — 1.92	130	(2.84 0.27 0.21) $\times 10^{-5}$			6.47 — 7.76	1419	(1.38 0.03 0.05) $\times 10^{-4}$		
1.92 — 2.40	293	(3.15 0.22 0.14) $\times 10^{-5}$			7.76 — 9.26	1336	(1.48 0.04 0.05) $\times 10^{-4}$		
2.40 — 2.97	527	(3.88 0.21 0.19) $\times 10^{-5}$			9.26 — 11.0	1297	(1.61 0.04 0.05) $\times 10^{-4}$		
2.97 — 3.64	1002	(5.79 0.22 0.27) $\times 10^{-5}$			11.0 — 13.0	1248	(1.84 0.05 0.08) $\times 10^{-4}$		
3.64 — 4.43	1141	(8.66 0.23 0.33) $\times 10^{-5}$			13.0 — 15.3	1063	(1.86 0.05 0.06) $\times 10^{-4}$		
4.43 — 5.37	1130	(9.88 0.27 0.34) $\times 10^{-5}$			15.3 — 18.0	977	(1.99 0.06 0.06) $\times 10^{-4}$		
5.37 — 6.47	1283	(1.15 0.03 0.03) $\times 10^{-4}$							

Table B.7: For Bartels Rotations 2456 to 2462 (Aug 02, 2013 – Jan 11, 2014), the observed antiproton numbers and the antiproton to proton flux ratio with its statistical and systematic uncertainties.

<b>Rigidity (GV)</b>	$N_{\bar{p}}$	$\frac{\Phi_{\bar{p}}}{\Phi_p}$	$\sigma_{\text{stat}}$	$\sigma_{\text{syst}}$	<b>Rigidity (GV)</b>	$N_{\bar{p}}$	$\frac{\Phi_{\bar{p}}}{\Phi_p}$	$\sigma_{\text{stat}}$	$\sigma_{\text{syst}}$
1.51 — 1.92	152	(2.76 0.24 0.18) $\times 10^{-5}$			6.47 — 7.76	1500	(1.35 0.03 0.04) $\times 10^{-4}$		
1.92 — 2.40	358	(3.30 0.21 0.16) $\times 10^{-5}$			7.76 — 9.26	1458	(1.50 0.04 0.05) $\times 10^{-4}$		
2.40 — 2.97	711	(4.57 0.21 0.22) $\times 10^{-5}$			9.26 — 11.0	1469	(1.69 0.04 0.07) $\times 10^{-4}$		
2.97 — 3.64	1038	(5.31 0.20 0.25) $\times 10^{-5}$			11.0 — 13.0	1306	(1.78 0.04 0.07) $\times 10^{-4}$		
3.64 — 4.43	1207	(8.29 0.22 0.32) $\times 10^{-5}$			13.0 — 15.3	1161	(1.88 0.05 0.05) $\times 10^{-4}$		
4.43 — 5.37	1254	(10.0 0.26 0.39) $\times 10^{-5}$			15.3 — 18.0	1042	(1.96 0.06 0.06) $\times 10^{-4}$		
5.37 — 6.47	1442	(1.19 0.03 0.03) $\times 10^{-4}$							

Table B.8: For Bartels Rotations 2462 to 2468 (Jan 11, 2014 – Jun 22, 2014), the observed antiproton numbers and the antiproton to proton flux ratio with its statistical and systematic uncertainties.

<b>Rigidity (GV)</b>	$N_{\bar{p}}$	$\frac{\Phi_{\bar{p}}}{\Phi_p}$	$\sigma_{\text{stat}}$	$\sigma_{\text{syst}}$	<b>Rigidity (GV)</b>	$N_{\bar{p}}$	$\frac{\Phi_{\bar{p}}}{\Phi_p}$	$\sigma_{\text{stat}}$	$\sigma_{\text{syst}}$
1.51 — 1.92	85	(2.38 0.26 0.16) $\times 10^{-5}$			6.47 — 7.76	885	(1.29 0.04 0.04) $\times 10^{-4}$		
1.92 — 2.40	258	(3.71 0.27 0.21) $\times 10^{-5}$			7.76 — 9.26	828	(1.38 0.04 0.06) $\times 10^{-4}$		
2.40 — 2.97	367	(3.70 0.23 0.20) $\times 10^{-5}$			9.26 — 11.0	881	(1.65 0.05 0.07) $\times 10^{-4}$		
2.97 — 3.64	605	(4.90 0.23 0.24) $\times 10^{-5}$			11.0 — 13.0	803	(1.78 0.06 0.09) $\times 10^{-4}$		
3.64 — 4.43	779	(8.62 0.28 0.31) $\times 10^{-5}$			13.0 — 15.3	747	(1.98 0.06 0.07) $\times 10^{-4}$		
4.43 — 5.37	746	(9.63 0.32 0.36) $\times 10^{-5}$			15.3 — 18.0	614	(1.90 0.07 0.08) $\times 10^{-4}$		
5.37 — 6.47	886	(1.18 0.04 0.03) $\times 10^{-4}$							

Table B.9: For Bartels Rotations 2468 to 2474 (Jun 22, 2014 – Dec 01, 2014), the observed antiproton numbers and the antiproton to proton flux ratio with its statistical and systematic uncertainties.

<b>Rigidity (GV)</b>	$N_{\bar{p}}$	$\frac{\Phi_{\bar{p}}}{\Phi_p}$	$\sigma_{\text{stat}}$	$\sigma_{\text{syst}}$	<b>Rigidity (GV)</b>	$N_{\bar{p}}$	$\frac{\Phi_{\bar{p}}}{\Phi_p}$	$\sigma_{\text{stat}}$	$\sigma_{\text{syst}}$
1.51 — 1.92	110	(2.76 0.29 0.23) $\times 10^{-5}$			6.47 — 7.76	1322	(1.32 0.03 0.04) $\times 10^{-4}$		
1.92 — 2.40	244	(3.02 0.23 0.17) $\times 10^{-5}$			7.76 — 9.26	1300	(1.47 0.04 0.05) $\times 10^{-4}$		
2.40 — 2.97	458	(3.78 0.22 0.17) $\times 10^{-5}$			9.26 — 11.0	1358	(1.70 0.04 0.08) $\times 10^{-4}$		
2.97 — 3.64	870	(5.57 0.22 0.26) $\times 10^{-5}$			11.0 — 13.0	1257	(1.85 0.05 0.06) $\times 10^{-4}$		
3.64 — 4.43	984	(7.72 0.23 0.30) $\times 10^{-5}$			13.0 — 15.3	1134	(1.97 0.05 0.05) $\times 10^{-4}$		
4.43 — 5.37	1065	(9.58 0.27 0.33) $\times 10^{-5}$			15.3 — 18.0	925	(1.85 0.06 0.08) $\times 10^{-4}$		
5.37 — 6.47	1247	(1.15 0.03 0.03) $\times 10^{-4}$							

Table B.10: For Bartels Rotations 2474 to 2480 (Dec 01, 2014 – May 12, 2015), the observed antiproton numbers and the antiproton to proton flux ratio with its statistical and systematic uncertainties.

<b>Rigidity (GV)</b>	$N_{\bar{p}}$	$\frac{\Phi_{\bar{p}}}{\Phi_p}$	$\sigma_{\text{stat}}$	$\sigma_{\text{syst}}$	<b>Rigidity (GV)</b>	$N_{\bar{p}}$	$\frac{\Phi_{\bar{p}}}{\Phi_p}$	$\sigma_{\text{stat}}$	$\sigma_{\text{syst}}$
1.51 — 1.92	85	(2.91 0.34 0.17) $\times 10^{-5}$			6.47 — 7.76	1242	(1.31 0.03 0.04) $\times 10^{-4}$		
1.92 — 2.40	213	(3.31 0.27 0.23) $\times 10^{-5}$			7.76 — 9.26	1236	(1.48 0.04 0.06) $\times 10^{-4}$		
2.40 — 2.97	392	(3.87 0.25 0.24) $\times 10^{-5}$			9.26 — 11.0	1262	(1.66 0.04 0.06) $\times 10^{-4}$		
2.97 — 3.64	708	(5.24 0.23 0.24) $\times 10^{-5}$			11.0 — 13.0	1141	(1.76 0.05 0.07) $\times 10^{-4}$		
3.64 — 4.43	878	(7.44 0.23 0.31) $\times 10^{-5}$			13.0 — 15.3	1083	(1.97 0.05 0.08) $\times 10^{-4}$		
4.43 — 5.37	947	(9.05 0.27 0.32) $\times 10^{-5}$			15.3 — 18.0	947	(1.97 0.06 0.07) $\times 10^{-4}$		
5.37 — 6.47	1133	(1.11 0.03 0.04) $\times 10^{-4}$							

Table B.11: For Bartels Rotations 2480 to 2486 (May 12, 2015 – Oct 21, 2015), the observed antiproton numbers and the antiproton to proton flux ratio with its statistical and systematic uncertainties.

<b>Rigidity (GV)</b>	$N_{\bar{p}}$	$\frac{\Phi_{\bar{p}}}{\Phi_p}$	$\sigma_{\text{stat}}$	$\sigma_{\text{syst}}$	<b>Rigidity (GV)</b>	$N_{\bar{p}}$	$\frac{\Phi_{\bar{p}}}{\Phi_p}$	$\sigma_{\text{stat}}$	$\sigma_{\text{syst}}$
1.51 — 1.92	59	(1.81 0.26 0.12) $\times 10^{-5}$			6.47 — 7.76	1191	(1.23 0.03 0.04) $\times 10^{-4}$		
1.92 — 2.40	189	(2.65 0.23 0.14) $\times 10^{-5}$			7.76 — 9.26	1195	(1.41 0.04 0.05) $\times 10^{-4}$		
2.40 — 2.97	404	(3.63 0.22 0.21) $\times 10^{-5}$			9.26 — 11.0	1274	(1.66 0.04 0.06) $\times 10^{-4}$		
2.97 — 3.64	726	(4.94 0.22 0.25) $\times 10^{-5}$			11.0 — 13.0	1180	(1.81 0.05 0.09) $\times 10^{-4}$		
3.64 — 4.43	931	(7.62 0.23 0.28) $\times 10^{-5}$			13.0 — 15.3	1047	(1.90 0.05 0.07) $\times 10^{-4}$		
4.43 — 5.37	981	(9.06 0.26 0.33) $\times 10^{-5}$			15.3 — 18.0	917	(1.91 0.06 0.10) $\times 10^{-4}$		
5.37 — 6.47	1188	(1.13 0.03 0.04) $\times 10^{-4}$							

Table B.12: For Bartels Rotations 2486 to 2492 (Oct 21, 2015 – Mar 31, 2016), the observed antiproton numbers and the antiproton to proton flux ratio with its statistical and systematic uncertainties.

<b>Rigidity (GV)</b>	$N_{\bar{p}}$	$\frac{\Phi_{\bar{p}}}{\Phi_p}$	$\sigma_{\text{stat}}$	$\sigma_{\text{syst}}$	<b>Rigidity (GV)</b>	$N_{\bar{p}}$	$\frac{\Phi_{\bar{p}}}{\Phi_p}$	$\sigma_{\text{stat}}$	$\sigma_{\text{syst}}$
1.51 — 1.92	84	(2.43 0.29 0.15) $\times 10^{-5}$			6.47 — 7.76	1178	(1.20 0.03 0.04) $\times 10^{-4}$		
1.92 — 2.40	173	(2.22 0.20 0.15) $\times 10^{-5}$			7.76 — 9.26	1185	(1.39 0.04 0.05) $\times 10^{-4}$		
2.40 — 2.97	394	(3.29 0.21 0.22) $\times 10^{-5}$			9.26 — 11.0	1230	(1.60 0.04 0.05) $\times 10^{-4}$		
2.97 — 3.64	721	(4.62 0.20 0.22) $\times 10^{-5}$			11.0 — 13.0	1148	(1.76 0.05 0.09) $\times 10^{-4}$		
3.64 — 4.43	883	(7.03 0.22 0.25) $\times 10^{-5}$			13.0 — 15.3	996	(1.81 0.05 0.05) $\times 10^{-4}$		
4.43 — 5.37	989	(8.94 0.26 0.32) $\times 10^{-5}$			15.3 — 18.0	939	(1.96 0.06 0.06) $\times 10^{-4}$		
5.37 — 6.47	1127	(1.05 0.03 0.04) $\times 10^{-4}$							

Table B.13: For Bartels Rotations 2492 to 2498 (Mar 31, 2016 – Sep 09, 2016), the observed antiproton numbers and the antiproton to proton flux ratio with its statistical and systematic uncertainties.

<b>Rigidity (GV)</b>	$N_{\bar{p}}$	$\frac{\Phi_{\bar{p}}}{\Phi_p}$	$\sigma_{\text{stat}}$	$\sigma_{\text{syst}}$	<b>Rigidity (GV)</b>	$N_{\bar{p}}$	$\frac{\Phi_{\bar{p}}}{\Phi_p}$	$\sigma_{\text{stat}}$	$\sigma_{\text{syst}}$
1.51 — 1.92	41	(1.36 0.23 0.10) $\times 10^{-5}$			6.47 — 7.76	1189	(1.23 0.03 0.04) $\times 10^{-4}$		
1.92 — 2.40	182	(2.54 0.23 0.16) $\times 10^{-5}$			7.76 — 9.26	1295	(1.53 0.04 0.06) $\times 10^{-4}$		
2.40 — 2.97	344	(3.05 0.21 0.19) $\times 10^{-5}$			9.26 — 11.0	1249	(1.63 0.04 0.05) $\times 10^{-4}$		
2.97 — 3.64	622	(4.17 0.20 0.21) $\times 10^{-5}$			11.0 — 13.0	1179	(1.82 0.05 0.07) $\times 10^{-4}$		
3.64 — 4.43	849	(7.05 0.22 0.26) $\times 10^{-5}$			13.0 — 15.3	997	(1.82 0.05 0.06) $\times 10^{-4}$		
4.43 — 5.37	926	(8.63 0.26 0.32) $\times 10^{-5}$			15.3 — 18.0	946	(1.98 0.06 0.10) $\times 10^{-4}$		
5.37 — 6.47	1153	(1.09 0.03 0.04) $\times 10^{-4}$							

Table B.14: For Bartels Rotations 2498 to 2504 (Sep 09, 2016 – Feb 18, 2017), the observed antiproton numbers and the antiproton to proton flux ratio with its statistical and systematic uncertainties.

<b>Rigidity (GV)</b>	$N_{\bar{p}}$	$\frac{\Phi_{\bar{p}}}{\Phi_p}$	$\sigma_{\text{stat}}$	$\sigma_{\text{syst}}$	<b>Rigidity (GV)</b>	$N_{\bar{p}}$	$\frac{\Phi_{\bar{p}}}{\Phi_p}$	$\sigma_{\text{stat}}$	$\sigma_{\text{syst}}$
1.51 — 1.92	46	(1.62 0.28 0.22) $\times 10^{-5}$			6.47 — 7.76	1170	(1.28 0.03 0.04) $\times 10^{-4}$		
1.92 — 2.40	150	(2.34 0.23 0.15) $\times 10^{-5}$			7.76 — 9.26	1155	(1.44 0.04 0.07) $\times 10^{-4}$		
2.40 — 2.97	347	(3.42 0.22 0.21) $\times 10^{-5}$			9.26 — 11.0	1154	(1.60 0.04 0.11) $\times 10^{-4}$		
2.97 — 3.64	558	(4.13 0.21 0.22) $\times 10^{-5}$			11.0 — 13.0	1038	(1.69 0.05 0.09) $\times 10^{-4}$		
3.64 — 4.43	809	(7.34 0.23 0.32) $\times 10^{-5}$			13.0 — 15.3	1008	(1.94 0.06 0.06) $\times 10^{-4}$		
4.43 — 5.37	920	(9.27 0.28 0.31) $\times 10^{-5}$			15.3 — 18.0	869	(1.91 0.06 0.06) $\times 10^{-4}$		
5.37 — 6.47	1137	(1.14 0.03 0.04) $\times 10^{-4}$							

Table B.15: For Bartels Rotations 2504 to 2510 (Feb 18, 2017 – Jul 30, 2017), the observed antiproton numbers and the antiproton to proton flux ratio with its statistical and systematic uncertainties.

<b>Rigidity (GV)</b>	$N_{\bar{p}}$	$\frac{\Phi_{\bar{p}}}{\Phi_p}$	$\sigma_{\text{stat}}$	$\sigma_{\text{syst}}$	<b>Rigidity (GV)</b>	$N_{\bar{p}}$	$\frac{\Phi_{\bar{p}}}{\Phi_p}$	$\sigma_{\text{stat}}$	$\sigma_{\text{syst}}$
1.51 — 1.92	60	(1.91 0.28 0.15) $\times 10^{-5}$			6.47 — 7.76	1224	(1.28 0.03 0.04) $\times 10^{-4}$		
1.92 — 2.40	152	(2.27 0.22 0.14) $\times 10^{-5}$			7.76 — 9.26	1251	(1.48 0.04 0.06) $\times 10^{-4}$		
2.40 — 2.97	319	(3.07 0.22 0.16) $\times 10^{-5}$			9.26 — 11.0	1292	(1.69 0.04 0.06) $\times 10^{-4}$		
2.97 — 3.64	632	(4.64 0.22 0.29) $\times 10^{-5}$			11.0 — 13.0	1095	(1.67 0.05 0.11) $\times 10^{-4}$		
3.64 — 4.43	759	(6.78 0.23 0.27) $\times 10^{-5}$			13.0 — 15.3	1030	(1.84 0.05 0.05) $\times 10^{-4}$		
4.43 — 5.37	967	(9.43 0.28 0.34) $\times 10^{-5}$			15.3 — 18.0	928	(1.91 0.06 0.11) $\times 10^{-4}$		
5.37 — 6.47	1101	(1.06 0.03 0.03) $\times 10^{-4}$							

Table B.16: For Bartels Rotations 2510 to 2516 (Jul 30, 2017 – Jan 08, 2018), the observed antiproton numbers and the antiproton to proton flux ratio with its statistical and systematic uncertainties.

<b>Rigidity (GV)</b>	$N_{\bar{p}}$	$\frac{\Phi_{\bar{p}}}{\Phi_p}$	$\sigma_{\text{stat}}$	$\sigma_{\text{syst}}$	<b>Rigidity (GV)</b>	$N_{\bar{p}}$	$\frac{\Phi_{\bar{p}}}{\Phi_p}$	$\sigma_{\text{stat}}$	$\sigma_{\text{syst}}$
1.51 — 1.92	75	(1.80 0.24 0.14) $\times 10^{-5}$			6.47 — 7.76	1245	(1.25 0.03 0.04) $\times 10^{-4}$		
1.92 — 2.40	190	(2.21 0.19 0.15) $\times 10^{-5}$			7.76 — 9.26	1289	(1.49 0.04 0.07) $\times 10^{-4}$		
2.40 — 2.97	374	(2.98 0.19 0.15) $\times 10^{-5}$			9.26 — 11.0	1269	(1.63 0.04 0.06) $\times 10^{-4}$		
2.97 — 3.64	709	(4.44 0.20 0.20) $\times 10^{-5}$			11.0 — 13.0	1203	(1.82 0.05 0.05) $\times 10^{-4}$		
3.64 — 4.43	870	(7.15 0.22 0.30) $\times 10^{-5}$			13.0 — 15.3	1015	(1.82 0.05 0.05) $\times 10^{-4}$		
4.43 — 5.37	986	(9.08 0.27 0.34) $\times 10^{-5}$			15.3 — 18.0	938	(1.93 0.06 0.12) $\times 10^{-4}$		
5.37 — 6.47	1263	(1.16 0.03 0.04) $\times 10^{-4}$							

Table B.17: For Bartels Rotations 2516 to 2522 (Jan 08, 2018 – Jun 19, 2018), the observed antiproton numbers and the antiproton to proton flux ratio with its statistical and systematic uncertainties.

<b>Rigidity (GV)</b>	$N_{\bar{p}}$	$\frac{\Phi_{\bar{p}}}{\Phi_p}$	$\sigma_{\text{stat}}$	$\sigma_{\text{syst}}$	<b>Rigidity (GV)</b>	$N_{\bar{p}}$	$\frac{\Phi_{\bar{p}}}{\Phi_p}$	$\sigma_{\text{stat}}$	$\sigma_{\text{syst}}$
1.51 — 1.92	40	(1.89 0.32 0.30) $\times 10^{-5}$			6.47 — 7.76	777	(1.31 0.04 0.05) $\times 10^{-4}$		
1.92 — 2.40	104	(2.29 0.26 0.16) $\times 10^{-5}$			7.76 — 9.26	768	(1.48 0.05 0.07) $\times 10^{-4}$		
2.40 — 2.97	230	(3.33 0.26 0.20) $\times 10^{-5}$			9.26 — 11.0	816	(1.74 0.05 0.09) $\times 10^{-4}$		
2.97 — 3.64	401	(4.49 0.26 0.26) $\times 10^{-5}$			11.0 — 13.0	713	(1.79 0.06 0.07) $\times 10^{-4}$		
3.64 — 4.43	517	(7.28 0.29 0.26) $\times 10^{-5}$			13.0 — 15.3	669	(1.98 0.07 0.07) $\times 10^{-4}$		
4.43 — 5.37	601	(9.35 0.35 0.33) $\times 10^{-5}$			15.3 — 18.0	574	(1.95 0.07 0.12) $\times 10^{-4}$		
5.37 — 6.47	758	(1.17 0.04 0.05) $\times 10^{-4}$							

Table B.18: For Bartels Rotations 2522 to 2528 (Jun 19, 2018 – Nov 28, 2018), the observed antiproton numbers and the antiproton to proton flux ratio with its statistical and systematic uncertainties.

<b>Rigidity (GV)</b>	$N_{\bar{p}}$	$\frac{\Phi_{\bar{p}}}{\Phi_p}$	$\sigma_{\text{stat}}$	$\sigma_{\text{syst}}$	<b>Rigidity (GV)</b>	$N_{\bar{p}}$	$\frac{\Phi_{\bar{p}}}{\Phi_p}$	$\sigma_{\text{stat}}$	$\sigma_{\text{syst}}$
1.51 — 1.92	45	(1.59 0.26 0.17) $\times 10^{-5}$			6.47 — 7.76	767	(1.30 0.04 0.04) $\times 10^{-4}$		
1.92 — 2.40	97	(1.76 0.21 0.15) $\times 10^{-5}$			7.76 — 9.26	819	(1.60 0.05 0.06) $\times 10^{-4}$		
2.40 — 2.97	224	(2.87 0.23 0.17) $\times 10^{-5}$			9.26 — 11.0	719	(1.57 0.05 0.05) $\times 10^{-4}$		
2.97 — 3.64	380	(3.88 0.22 0.21) $\times 10^{-5}$			11.0 — 13.0	736	(1.90 0.06 0.05) $\times 10^{-4}$		
3.64 — 4.43	564	(7.76 0.30 0.32) $\times 10^{-5}$			13.0 — 15.3	593	(1.82 0.07 0.07) $\times 10^{-4}$		
4.43 — 5.37	572	(8.84 0.33 0.30) $\times 10^{-5}$			15.3 — 18.0	556	(1.96 0.08 0.07) $\times 10^{-4}$		
5.37 — 6.47	680	(1.05 0.04 0.04) $\times 10^{-4}$							

Table B.19: For Bartels Rotations 2528 to 2534 (Nov 28, 2018 – May 09, 2019), the observed antiproton numbers and the antiproton to proton flux ratio with its statistical and systematic uncertainties.

<b>Rigidity (GV)</b>	$N_{\bar{p}}$	$\frac{\Phi_{\bar{p}}}{\Phi_p}$	$\sigma_{\text{stat}}$	$\sigma_{\text{syst}}$	<b>Rigidity (GV)</b>	$N_{\bar{p}}$	$\frac{\Phi_{\bar{p}}}{\Phi_p}$	$\sigma_{\text{stat}}$	$\sigma_{\text{syst}}$
1.51 — 1.92	42	(2.00 0.33 0.17)×10 <sup>-5</sup>			6.47 — 7.76	741	(1.32 0.04 0.04)×10 <sup>-4</sup>		
1.92 — 2.40	85	(1.90 0.24 0.19)×10 <sup>-5</sup>			7.76 — 9.26	711	(1.45 0.05 0.05)×10 <sup>-4</sup>		
2.40 — 2.97	207	(3.07 0.25 0.25)×10 <sup>-5</sup>			9.26 — 11.0	757	(1.72 0.06 0.08)×10 <sup>-4</sup>		
2.97 — 3.64	359	(4.11 0.25 0.21)×10 <sup>-5</sup>			11.0 — 13.0	725	(1.95 0.06 0.08)×10 <sup>-4</sup>		
3.64 — 4.43	514	(7.59 0.31 0.33)×10 <sup>-5</sup>			13.0 — 15.3	585	(1.86 0.07 0.06)×10 <sup>-4</sup>		
4.43 — 5.37	508	(8.31 0.34 0.35)×10 <sup>-5</sup>			15.3 — 18.0	529	(1.93 0.08 0.11)×10 <sup>-4</sup>		
5.37 — 6.47	715	(1.16 0.04 0.04)×10 <sup>-4</sup>							

Table B.20: For Bartels Rotations 2534 to 2540 (May 09, 2019 – Oct 18, 2019), the observed antiproton numbers and the antiproton to proton flux ratio with its statistical and systematic uncertainties.

<b>Rigidity (GV)</b>	$N_{\bar{p}}$	$\frac{\Phi_{\bar{p}}}{\Phi_p}$	$\sigma_{\text{stat}}$	$\sigma_{\text{syst}}$	<b>Rigidity (GV)</b>	$N_{\bar{p}}$	$\frac{\Phi_{\bar{p}}}{\Phi_p}$	$\sigma_{\text{stat}}$	$\sigma_{\text{syst}}$
1.51 — 1.92	34	(2.01 0.35 0.16)×10 <sup>-5</sup>			6.47 — 7.76	545	(1.30 0.05 0.04)×10 <sup>-4</sup>		
1.92 — 2.40	83	(2.36 0.30 0.18)×10 <sup>-5</sup>			7.76 — 9.26	541	(1.48 0.06 0.05)×10 <sup>-4</sup>		
2.40 — 2.97	152	(2.96 0.27 0.15)×10 <sup>-5</sup>			9.26 — 11.0	503	(1.54 0.06 0.06)×10 <sup>-4</sup>		
2.97 — 3.64	304	(4.58 0.28 0.23)×10 <sup>-5</sup>			11.0 — 13.0	483	(1.75 0.07 0.07)×10 <sup>-4</sup>		
3.64 — 4.43	331	(6.70 0.34 0.27)×10 <sup>-5</sup>			13.0 — 15.3	435	(1.87 0.08 0.07)×10 <sup>-4</sup>		
4.43 — 5.37	375	(8.36 0.40 0.27)×10 <sup>-5</sup>			15.3 — 18.0	385	(1.91 0.09 0.06)×10 <sup>-4</sup>		
5.37 — 6.47	503	(1.10 0.04 0.03)×10 <sup>-4</sup>							

Table B.21: For Bartels Rotations 2540 to 2546 (Oct 18, 2019 – Mar 28, 2020), the observed antiproton numbers and the antiproton to proton flux ratio with its statistical and systematic uncertainties.

<b>Rigidity (GV)</b>	$N_{\bar{p}}$	$\frac{\Phi_{\bar{p}}}{\Phi_p}$	$\sigma_{\text{stat}}$	$\sigma_{\text{syst}}$	<b>Rigidity (GV)</b>	$N_{\bar{p}}$	$\frac{\Phi_{\bar{p}}}{\Phi_p}$	$\sigma_{\text{stat}}$	$\sigma_{\text{syst}}$
1.51 — 1.92	49	(2.76 0.40 0.25)×10 <sup>-5</sup>			6.47 — 7.76	549	(1.28 0.05 0.04)×10 <sup>-4</sup>		
1.92 — 2.40	89	(2.48 0.29 0.14)×10 <sup>-5</sup>			7.76 — 9.26	565	(1.52 0.06 0.07)×10 <sup>-4</sup>		
2.40 — 2.97	187	(3.56 0.28 0.23)×10 <sup>-5</sup>			9.26 — 11.0	553	(1.66 0.06 0.08)×10 <sup>-4</sup>		
2.97 — 3.64	321	(4.78 0.29 0.27)×10 <sup>-5</sup>			11.0 — 13.0	521	(1.85 0.07 0.05)×10 <sup>-4</sup>		
3.64 — 4.43	374	(7.48 0.35 0.36)×10 <sup>-5</sup>			13.0 — 15.3	436	(1.84 0.08 0.05)×10 <sup>-4</sup>		
4.43 — 5.37	415	(9.12 0.40 0.32)×10 <sup>-5</sup>			15.3 — 18.0	423	(2.06 0.09 0.06)×10 <sup>-4</sup>		
5.37 — 6.47	553	(1.18 0.04 0.04)×10 <sup>-4</sup>							

Table B.22: For Bartels Rotations 2546 to 2552 (Mar 28, 2020 – Sep 06, 2020), the observed antiproton numbers and the antiproton to proton flux ratio with its statistical and systematic uncertainties.

<b>Rigidity (GV)</b>	$N_{\bar{p}}$	$\frac{\Phi_{\bar{p}}}{\Phi_p}$	$\sigma_{\text{stat}}$	$\sigma_{\text{syst}}$	<b>Rigidity (GV)</b>	$N_{\bar{p}}$	$\frac{\Phi_{\bar{p}}}{\Phi_p}$	$\sigma_{\text{stat}}$	$\sigma_{\text{syst}}$
1.51 — 1.92	52	(1.82 0.29 0.18)×10 <sup>-5</sup>			6.47 — 7.76	1036	(1.39 0.04 0.04)×10 <sup>-4</sup>		
1.92 — 2.40	136	(2.23 0.22 0.17)×10 <sup>-5</sup>			7.76 — 9.26	987	(1.52 0.05 0.06)×10 <sup>-4</sup>		
2.40 — 2.97	265	(2.90 0.22 0.16)×10 <sup>-5</sup>			9.26 — 11.0	993	(1.71 0.05 0.05)×10 <sup>-4</sup>		
2.97 — 3.64	504	(4.27 0.22 0.23)×10 <sup>-5</sup>			11.0 — 13.0	904	(1.84 0.06 0.08)×10 <sup>-4</sup>		
3.64 — 4.43	689	(7.79 0.27 0.35)×10 <sup>-5</sup>			13.0 — 15.3	786	(1.89 0.06 0.10)×10 <sup>-4</sup>		
4.43 — 5.37	697	(8.66 0.30 0.29)×10 <sup>-5</sup>			15.3 — 18.0	703	(1.95 0.07 0.06)×10 <sup>-4</sup>		
5.37 — 6.47	911	(1.12 0.03 0.04)×10 <sup>-4</sup>							

Table B.23: For Bartels Rotations 2552 to 2558 (Sep 06, 2020 – Feb 15, 2021), the observed antiproton numbers and the antiproton to proton flux ratio with its statistical and systematic uncertainties.

<b>Rigidity (GV)</b>	$N_{\bar{p}}$	$\frac{\Phi_{\bar{p}}}{\Phi_p}$	$\sigma_{\text{stat}}$	$\sigma_{\text{syst}}$	<b>Rigidity (GV)</b>	$N_{\bar{p}}$	$\frac{\Phi_{\bar{p}}}{\Phi_p}$	$\sigma_{\text{stat}}$	$\sigma_{\text{syst}}$
1.51 — 1.92	22	(2.55 0.54 0.23)×10 <sup>-5</sup>			6.47 — 7.76	470	(1.40 0.06 0.04)×10 <sup>-4</sup>		
1.92 — 2.40	42	(1.94 0.31 0.16)×10 <sup>-5</sup>			7.76 — 9.26	473	(1.62 0.07 0.06)×10 <sup>-4</sup>		
2.40 — 2.97	139	(3.83 0.36 0.19)×10 <sup>-5</sup>			9.26 — 11.0	423	(1.61 0.07 0.06)×10 <sup>-4</sup>		
2.97 — 3.64	245	(4.98 0.35 0.26)×10 <sup>-5</sup>			11.0 — 13.0	422	(1.89 0.08 0.09)×10 <sup>-4</sup>		
3.64 — 4.43	288	(7.39 0.39 0.31)×10 <sup>-5</sup>			13.0 — 15.3	372	(1.96 0.09 0.05)×10 <sup>-4</sup>		
4.43 — 5.37	321	(8.90 0.45 0.39)×10 <sup>-5</sup>			15.3 — 18.0	308	(1.87 0.10 0.06)×10 <sup>-4</sup>		
5.37 — 6.47	446	(1.22 0.05 0.05)×10 <sup>-4</sup>							

Table B.24: For Bartels Rotations 2558 to 2564 (Feb 15, 2021 – Jul 27, 2021), the observed antiproton numbers and the antiproton to proton flux ratio with its statistical and systematic uncertainties.

## Appendix C

### Acronyms

<b>ACC</b>	.....	Anti-Coincidence Counters
<b>AMS</b>	.....	Alpha Magnetic Spectrometer
<b>BDT</b>	.....	Boosted Decision Tree
<b>CALT</b>	.....	China Academy of Launch Vehicle Technology
<b>CC</b>	.....	Charge Confusion
<b>CR</b>	.....	Cosmic Rays
<b>ECAL</b>	.....	Electromagnetic Calorimeter
<b>GCR</b>	.....	Galactic Cosmic Rays
<b>GTB</b>	.....	Gradient Tree Boosting
<b>HCS</b>	.....	Heliospheric Current Sheet
<b>HMF</b>	.....	Heliospheric Magnetic Field
<b>HT</b>	.....	High Threshold
<b>IGRF</b>	.....	International Geomagnetic Reference Field
<b>ISM</b>	.....	Interstellar Medium

<b>ISS</b>	.....	International Space Station
<b>LIS</b>	.....	Local Interstellar Spectra
<b>MDR</b>	.....	Maximum Detectable Rigidity
<b>MHD</b>	.....	Magneto-Hydrodynamic
<b>MIP</b>	.....	Minimum Ionizing Particle
<b>MSFC</b>	.....	Marshall Space Flight Center
<b>NM</b>	.....	Neutron Monitor
<b>POCC</b>	.....	Payload Operations Control Centre
<b>PWN</b>	.....	Pulsar Wind Nebula
<b>RICH</b>	.....	Ring-Imaging Cherenkov detector
<b>SAA</b>	.....	South Atlantic Anomaly
<b>SHT</b>	.....	Super High Threshold
<b>SNRs</b>	.....	Supernova Remnants
<b>SSN</b>	.....	Sunspot Number
<b>SVM</b>	.....	Support Vector Machine
<b>TAS</b>	.....	Tracker Alignment System
<b>TDRS</b>	.....	Tracking and Data Relay Satellites
<b>TOF</b>	.....	Time Of Flight
<b>TRD</b>	.....	Transition Radiation Detector
<b>TTCS</b>	.....	Tracker Thermal Cooling System
<b>WSGT</b>	.....	White Sands Ground Terminal

# LIST OF FIGURES

Figure 2.1	Cosmic ray spectrum and components . . . . .	4
Figure 2.2	Element abundances between the GCR and the solar system . . . . .	5
Figure 2.3	Heliosphere and Particle rate detected by Voyager 1. . . . .	9
Figure 2.4	Cosmic rays intensity and Monthly mean sunspot numbers. . . . .	10
Figure 2.5	The measured antiproton flux. . . . .	12
Figure 3.1	The AMS-01 detector. . . . .	14
Figure 3.2	The AMS-02 detector on the ISS. . . . .	14
Figure 3.3	Schematic view of the AMS-02 experiment. . . . .	15
Figure 3.4	The TRD and its support structure during construction. . . . .	16
Figure 3.5	Illustration of the TRD separation between electrons and protons. .	17
Figure 3.6	Preparing for test of the permanent magnet. . . . .	18
Figure 3.7	A silicon tracker inner plane fully equipped with ladders. . . . .	18
Figure 3.8	Principle of operation of the double-sided silicon micro-strip sensors.	19
Figure 3.9	Tracker resolution measured with 400 GeV protons at the test beam and MC. . . . .	20
Figure 3.10	Tracker resolution from MC simulation for protons. . . . .	21
Figure 3.11	The TOF planes arrangement in the AMS-02 experiment. . . . .	22
Figure 3.12	The TOF $\beta$ resolution and charge distribution. . . . .	23
Figure 3.13	The RICH PMT plane, its expansion volume and two radiators. .	24
Figure 3.14	The RICH $\beta$ and charge resolution. . . . .	24
Figure 3.15	The ECAL superlayer structure. . . . .	25
Figure 3.16	The ECAL rejection power and energy resolution. . . . .	26
Figure 3.17	The ACC scintillator panels pair and PMTs. . . . .	27
Figure 4.1	The antiproton statistics comparison between MC and ISS data. .	31
Figure 4.2	Comparison of the lower TOF charge distributions for ISS and pro- ton MC. . . . .	36
Figure 4.3	Four most important input variables for charge confusion. . . . .	38
Figure 4.4	The charge confusion estimator. . . . .	40

Figure 4.5	The background rejection power of charge confusion estimator. . . . .	40
Figure 4.6	Separation between the electrons and protons in $\Lambda_{\text{TRD}}$ estimator. .	42
Figure 4.7	Negative ISS data and Fit result in 2.97 to 3.29 GV . . . . .	45
Figure 4.8	Example template fit in the low rigidity range of 2.97 to 3.29 GV. . .	46
Figure 4.9	The number of antiproton and proton events obtained in the low rigidity range. . . . .	47
Figure 4.10	Example template fit in the intermediate rigidity range of 5.9 to 6.47 GV. . . . .	48
Figure 4.11	The number of antiproton and proton events obtained in the intermediate rigidity range. . . . .	49
Figure 4.12	Negative rigidity ISS data and fit result in the rigidity range of 175 to 211 GV in $\Lambda_{\text{CC}}$ and $\Lambda_{\text{TRD}}$ space. . . . .	50
Figure 4.13	Example template fit in the high rigidity range of 175 to 211 GV. .	51
Figure 4.14	The antiproton and proton numbers obtained in the high rigidity range. . . . .	52
Figure 4.15	The parameterizations of the normalized antiproton and electron templates. . . . .	53
Figure 4.16	Time-dependence of the a) $\mu_{\bar{p},\text{TRD}}$ b) $\sigma_{\bar{p},\text{TRD}}$ c) $\mu_{e^-, \text{TRD}}$ d) $\sigma_{e^-, \text{TRD}}$ in 6.47 to 7.76 GV. . . . .	54
Figure 4.17	Time-dependence of the a) $\mu_{\bar{p},\text{TOF}}$ b) $\sigma_{\bar{p},\text{TOF}}$ c) $\mu_{e^-, \text{TOF}}$ d) $\sigma_{e^-, \text{TOF}}$ e) $\mu_{\text{secondaries,TOF}}$ f) $\sigma_{\text{secondaries,TOF}}$ in 3.64 to 4.43 GV. . . . .	55
Figure 4.18	Example template fit in 6.47 to 7.76 GV with data from Feb.2017 to Jul.2017. . . . .	56
Figure 4.19	Antiproton numbers in 6.47 to 7.76 GV with six Bartels' Rotation. .	57
Figure 4.20	$\chi^2/\text{ndf}$ of the fits in 6.47 to 7.76 GV with six Bartel's Rotation. .	57
Figure 4.21	Effective acceptance of protons and antiprotons. . . . .	59
Figure 4.22	Proton to antiproton effective acceptance ratios. . . . .	59
Figure 4.23	Live time fraction vs. ISS position. . . . .	61
Figure 4.24	Measuring time as a function of the live time fraction. . . . .	61
Figure 4.25	Illustration of the Earth's magnetic field. . . . .	62
Figure 4.26	The Størmer rigidity cutoff as a function of the ISS Position. . . . .	63
Figure 4.27	The measuring time from the Størmer geomagnetic cutoff. . . . .	64
Figure 4.28	The measuring time comparison between the Størmer and IGRF cutoffs. .	64
Figure 4.29	The measuring time in each six Bartels Rotations time bin. . . . .	65

Figure 4.30	The migration matrix for full span at the high rigidity range for proton MC. . . . .	66
Figure 4.31	The raw and unfolded events for antiproton and proton. . . . .	68
Figure 4.32	The time-averaged antiproton to proton flux ratio in three rigidity ranges. . . . .	69
Figure 4.33	The time-averaged antiproton to proton flux ratio with statistical uncertainty only. . . . .	69
Figure 4.34	The relative statistical uncertainty of the antiproton to proton flux ratio. . . . .	70
Figure 4.35	The antiproton to proton flux ratio in 1.92 to 2.4 GV in six Bartels Rotation. . . . .	70
Figure 4.36	The relative statistical uncertainty of the antiproton to proton flux ratio in 1.92 to 2.4 GV in six Bartels Rotation. . . . .	71
Figure 4.37	Effective acceptance ratio with antiproton cross sections varied by $\pm 10\%$ . . . . .	72
Figure 4.38	The systematic uncertainty from acceptance. . . . .	73
Figure 4.39	The template fit results in 2.15 to 2.4 GV while varying the signal efficiency. . . . .	74
Figure 4.40	The systematic uncertainty of the antiproton to proton flux ratio from the template fit range. . . . .	74
Figure 4.41	Charge confusion level in MC and data. . . . .	75
Figure 4.42	Data/MC charge confusion level ratio. . . . .	76
Figure 4.43	The relative systematic uncertainty from the charge confusion. . . . .	76
Figure 4.44	The relative total systematic error of the antiproton to proton flux ratio. . . . .	77
Figure 4.45	The systematic uncertainty in 1.92 to 2.4 GV in six Bartels Rotation. . . . .	78
Figure 5.1	The time-averaged antiproton to proton flux ratio. . . . .	80
Figure 5.2	Comparison between the antiproton to proton flux ratio in this analysis and in the Physics Report. . . . .	81
Figure 5.3	Uncertainty breakdown of the time-averaged antiproton to proton flux ratio. . . . .	82
Figure 5.4	The statistical and systematic uncertainty comparison between this analysis and in Physics Report. . . . .	82
Figure 5.5	Time-dependent antiproton to proton flux ratios for five bins. . . . .	84
Figure 5.6	Time-dependent antiproton to proton flux ratio compared with model. . . . .	85

Figure 5.7	Averaged relative statistical and systematic uncertainties of the time-dependent antiproton to proton flux ratio. . . . .	85
Figure 5.8	Breakdown of the total relative uncertainty in 1.92 to 2.4 GV. . . . .	86
Figure 5.9	Comparison between the antiproton to proton flux ratio and the electron to positron flux ratio over time in four rigidity bins. . . . .	88
Figure A.1	Distributions for $Q_{\text{LowTOF}}$ and $Q_{\text{UppTOF}}$ in 330 to 525 GV. . . . .	91
Figure A.2	Distributions for $\delta_{R_{L9}}$ and $\Gamma_{\text{Central}}$ in 330 to 525 GV. . . . .	92
Figure A.3	Distributions for $\log\chi^2_X$ , $\log\chi^2_Y$ , $\log\chi^2_{X_{\text{Inner}}}$ and $\log\chi^2_{Y_{\text{Inner}}}$ in 330 to 525 GV. . . . .	93
Figure A.4	Distributions for $Q_{L9}$ and $Q_{L78}$ in 330 to 525 GV. . . . .	94
Figure A.5	Distributions for $\delta_Q$ in 330 to 525 GV. . . . .	95
Figure A.6	Distributions for $\Lambda_{\text{TRD}}$ in 330 to 525 GV. . . . .	96

# LIST OF TABLES

TABLE 3.1	Table of the tracker pattern definitions.	20
TABLE 4.1	List of data taking quality cuts and their pass ratios	33
TABLE 4.2	List of analysis data quality cuts and their pass ratios	34
TABLE 4.3	List of selection cuts and their pass ratios	35
TABLE 4.4	List of selections to get all the templates and select further for the ISS data in the low rigidity range.	44
TABLE 4.5	List of selections to get all the templates and select further for the ISS data in the intermediate rigidity range.	48
TABLE B.1	The time-averaged antiproton to proton flux ratio for rigidity from 1.0 to 525 GV.	98
TABLE B.2	Antiproton to proton flux ratio for Bartels Rotations 2426 to 2432	99
TABLE B.3	Antiproton to proton flux ratio for Bartels Rotations 2432 to 2438	99
TABLE B.4	Antiproton to proton flux ratio for Bartels Rotations 2438 to 2444	99
TABLE B.5	Antiproton to proton flux ratio for Bartels Rotations 2444 to 2450	100
TABLE B.6	Antiproton to proton flux ratio for Bartels Rotations 2450 to 2456	100
TABLE B.7	Antiproton to proton flux ratio for Bartels Rotations 2456 to 2462	100
TABLE B.8	Antiproton to proton flux ratio for Bartels Rotations 2462 to 2468	101
TABLE B.9	Antiproton to proton flux ratio for Bartels Rotations 2468 to 2474	101
TABLE B.10	Antiproton to proton flux ratio for Bartels Rotations 2474 to 2480	101
TABLE B.11	Antiproton to proton flux ratio for Bartels Rotations 2480 to 2486	102
TABLE B.12	Antiproton to proton flux ratio for Bartels Rotations 2486 to 2492	102
TABLE B.13	Antiproton to proton flux ratio for Bartels Rotations 2492 to 2498	102
TABLE B.14	Antiproton to proton flux ratio for Bartels Rotations 2498 to 2504	103
TABLE B.15	Antiproton to proton flux ratio for Bartels Rotations 2504 to 2510	103
TABLE B.16	Antiproton to proton flux ratio for Bartels Rotations 2510 to 2516	103
TABLE B.17	Antiproton to proton flux ratio for Bartels Rotations 2516 to 2522	104
TABLE B.18	Antiproton to proton flux ratio for Bartels Rotations 2522 to 2528	104
TABLE B.19	Antiproton to proton flux ratio for Bartels Rotations 2528 to 2534	104

TABLE B.20 Antiproton to proton flux ratio for Bartels Rotations 2534 to 2540 . .	105
TABLE B.21 Antiproton to proton flux ratio for Bartels Rotations 2540 to 2546 . .	105
TABLE B.22 Antiproton to proton flux ratio for Bartels Rotations 2546 to 2552 . .	105
TABLE B.23 Antiproton to proton flux ratio for Bartels Rotations 2552 to 2558 . .	106
TABLE B.24 Antiproton to proton flux ratio for Bartels Rotations 2558 to 2564 . .	106

## BIBLIOGRAPHY

- [1] NobelPrize.org (Nobel Media AB). Victor F. Hess - Facts, 2022. URL: <https://www.nobelprize.org/prizes/physics/1936/hess/facts>.
- [2] C. D. Anderson. The Positive Electron. *Phys. Rev.*, 43:491–494, Mar 1933. DOI: [10.1103/PhysRev.43.491](https://doi.org/10.1103/PhysRev.43.491).
- [3] O. Chamberlain, E. Segre, and C. Wiegand. Antiprotons. *Technical Report*, Nov 1955. DOI: [10.2172/915070](https://doi.org/10.2172/915070).
- [4] E. A. Bogomolov et al. A Stratospheric Magnetic Spectrometer Investigation of the Singly Charged Component Spectra and Composition of the Primary and Secondary Cosmic Radiation. In *International Cosmic Ray Conference*, volume 1, page 330, 1979. URL: <https://articles.adsabs.harvard.edu/pdf/1979ICRC...16a.330B>.
- [5] R. L. Golden et al. Evidence for the Existence of Cosmic-Ray Antiprotons. *Phys. Rev. Lett.*, 43:1196–1199, Oct 1979. DOI: [10.1103/PhysRevLett.43.1196](https://doi.org/10.1103/PhysRevLett.43.1196).
- [6] O. Adriani et al. Measurement of the flux of primary cosmic ray antiprotons with energies of 60-MeV to 350-GeV in the PAMELA experiment. *JETP Letters*, 96:621–627, 2013. DOI: [10.1134/S002136401222002X](https://doi.org/10.1134/S002136401222002X).
- [7] K. Greisen. End to the Cosmic-Ray Spectrum? *Phys. Rev. Lett.*, 16:748–750, Apr 1966. DOI: [10.1103/PhysRevLett.16.748](https://doi.org/10.1103/PhysRevLett.16.748).
- [8] G. T. Zatsepin and V. A. Kuzmin. Upper Limit of the Spectrum of Cosmic Rays. *Soviet Journal of Experimental and Theoretical Physics Letters*, 4:78, Aug 1966. URL: <https://www.osti.gov/biblio/4515382>.
- [9] D. J. Bird et al. Detection of a Cosmic Ray with Measured Energy Well beyond the Expected Spectral Cutoff due to Cosmic Microwave Radiation. *Astrophysical Journal*, 441:144, Mar 1995. DOI: [10.1086/175344](https://doi.org/10.1086/175344).
- [10] R. Abbasi et al. Indications of Intermediate-Scale Anisotropy of Cosmic Rays with Energy Greater Than 57 EeV in the Northern Sky Measured with the Surface Detector of the Telescope Array Experiment. *The Astrophysical Journal*, 790(2):L21, Jul 2014. DOI: [10.1088/2041-8205/790/2/l21](https://doi.org/10.1088/2041-8205/790/2/l21).
- [11] H. William. Cosmic Ray Spectra of Various Experiments. URL: <https://web.physics.utah.edu/whanlon/spectrum.html>.
- [12] R. L. Workman et al. (Particle Data Group). Review of Particle Physics. *Prog. Theor. Exp. Phys.*, 2022:p.083C01, 2022. DOI: [10.1093/ptep/ptac097](https://doi.org/10.1093/ptep/ptac097).

- [13] M. Israel et al. An Overview of Cosmic-Ray Elemental Composition. *ACE News*, Oct 2004. URL: <https://izw1.caltech.edu/ACE/ACENews/ACENews83.html>.
- [14] W. Baade and F. Zwicky. Cosmic Rays from Super-novae. *Proceedings of the National Academy of Sciences of the United States of America*, 20(5):259–263, 1934. URL: <http://www.jstor.org/stable/86841>.
- [15] M. Turatto. Classification of Supernovae, pages 21–36. Springer Berlin Heidelberg, Berlin, Heidelberg, 2003. DOI: [10.1007/3-540-45863-8\\_3](https://doi.org/10.1007/3-540-45863-8_3).
- [16] S. P. Reynolds. Supernova Remnants at High Energy. *Annual Review of Astronomy and Astrophysics*, 46(1):89–126, 2008. DOI: [10.1146/annurev.astro.46.060407.145237](https://doi.org/10.1146/annurev.astro.46.060407.145237).
- [17] M. S. Longair. High Energy Astrophysics. UK: Cambridge University Press, 2011. URL: <https://ui.adsabs.harvard.edu/abs/2011hea..book....L>.
- [18] E. Fermi. On the Origin of the Cosmic Radiation. *Phys. Rev.*, 75:1169–1174, Apr 1949. DOI: [10.1103/PhysRev.75.1169](https://doi.org/10.1103/PhysRev.75.1169).
- [19] T. Gold, F. G. Smith, and A. W. Wolfendale. Pulsars and the Origin of Cosmic Rays and Discussion. *Philosophical Transactions of the Royal Society of London. Series A, Mathematical and Physical Sciences*, 277(1270):453–461, 1975. URL: <http://www.jstor.org/stable/74493>.
- [20] W. Bednarek and M. Bartosik. Cosmic rays from Galactic pulsars. *Astronomy & Astrophysics*, 423(2):405–413, 2004. DOI: [10.1051/0004-6361:20047005](https://doi.org/10.1051/0004-6361:20047005).
- [21] J. Arons. Pulsar wind nebulae as cosmic pevatrons: A current sheet’s tale. *Space Science Reviews*, 173:341–367, 2012. DOI: [10.1007/s11214-012-9885-1](https://doi.org/10.1007/s11214-012-9885-1).
- [22] A. R. Bell. Cosmic ray acceleration in pulsar-driven supernova remnants. *Monthly Notices of the Royal Astronomical Society*, 257(3):493–500, Aug 1992. DOI: [10.1093/mnras/257.3.493](https://doi.org/10.1093/mnras/257.3.493).
- [23] D. Hooper, P. Blasi, and P. D. Serpico. Pulsars as the sources of high energy cosmic ray positrons. *Journal of Cosmology and Astroparticle Physics*, 2009(01):025, Jan 2009. DOI: [10.1088/1475-7516/2009/01/025](https://doi.org/10.1088/1475-7516/2009/01/025).
- [24] R. Cowsik. Positrons and Antiprotons in Galactic Cosmic Rays. *Annual Review of Nuclear and Particle Science*, 66(1):297–319, 2016. DOI: [10.1146/annurev-nucl-102115-044851](https://doi.org/10.1146/annurev-nucl-102115-044851).
- [25] V. Bresci et al. Effects of re-acceleration and source grammage on secondary cosmic rays spectra. *Monthly Notices of the Royal Astronomical Society*, 488(2):2068–2078, 07 2019. DOI: [10.1093/mnras/stz1806](https://doi.org/10.1093/mnras/stz1806).

- [26] I. Cholis, T. Linden, and D. Hooper. A robust excess in the cosmic-ray antiproton spectrum: Implications for annihilating dark matter. *Phys. Rev. D*, 99:103026, May 2019. DOI: [10.1103/PhysRevD.99.103026](https://doi.org/10.1103/PhysRevD.99.103026).
- [27] J. Heisig. Cosmic-ray antiprotons in the AMS-02 era: A sensitive probe of dark matter. *Modern Physics Letters A*, 36(05):2130003, 2021. DOI: [10.1142/S0217732321300032](https://doi.org/10.1142/S0217732321300032).
- [28] M. W. Winkler. Cosmic ray antiprotons at high energies. *Journal of Cosmology and Astroparticle Physics*, 2017(02):048, Feb 2017. DOI: [10.1088/1475-7516/2017/02/048](https://doi.org/10.1088/1475-7516/2017/02/048).
- [29] R. Kappl and M. W. Winkler. The cosmic ray antiproton background for AMS-02. *Journal of Cosmology and Astroparticle Physics*, 2014(09):051–051, Sep 2014. DOI: [10.1088/1475-7516/2014/09/051](https://doi.org/10.1088/1475-7516/2014/09/051).
- [30] M. Cui et al. Possible dark matter annihilation signal in the ams-02 antiproton data. *Phys. Rev. Lett.*, 118:191101, May 2017. DOI: [10.1103/PhysRevLett.118.191101](https://doi.org/10.1103/PhysRevLett.118.191101).
- [31] A. W. Strong, I. V. Moskalenko, and V. S. Ptuskin. Cosmic-Ray Propagation and Interactions in the Galaxy. *Annual Review of Nuclear and Particle Science*, 57(1):285–327, 2007. DOI: [10.1146/annurev.nucl.57.090506.123011](https://doi.org/10.1146/annurev.nucl.57.090506.123011).
- [32] I. V. Moskalenko. Galprop: modeling cosmic ray propagation and associated interstellar emissions, 2011. DOI: [10.48550/ARXIV.1105.4921](https://doi.org/10.48550/ARXIV.1105.4921).
- [33] D. Maurin. USINE: Semi-analytical models for Galactic cosmic-ray propagation. *Computer Physics Communications*, 247:106942, 2020. DOI: [10.1016/j.cpc.2019.106942](https://doi.org/10.1016/j.cpc.2019.106942).
- [34] C. Evoli et al. Cosmic-ray propagation with DRAGON2: I. numerical solver and astrophysical ingredients. *Journal of Cosmology and Astroparticle Physics*, 2017(02):015–015, Feb 2017. DOI: [10.1088/1475-7516/2017/02/015](https://doi.org/10.1088/1475-7516/2017/02/015).
- [35] V. S. Ptuskin, O. N. Strelnikova, and L. G. Sveshnikova. On leaky-box approximation to GALPROP. *Astroparticle Physics*, 31:284–289, 2009. DOI: [10.1016/j.astropartphys.2009.02.004](https://doi.org/10.1016/j.astropartphys.2009.02.004).
- [36] E. N. Parker. Dynamics of the Interplanetary Gas and Magnetic Fields. *Astrophysical Journal*, 128:664, Nov 1958. DOI: [10.1086/146579](https://doi.org/10.1086/146579).
- [37] C. T. Russell. The Solar Wind and Magnetospheric Dynamics. In *Correlated Interplanetary and Magnetospheric Observations*, pages 3–47. Springer Netherlands, 1974. DOI: [10.1007/978-94-010-2172-2\\_1](https://doi.org/10.1007/978-94-010-2172-2_1).
- [38] M. J. Owens and R. J. Forsyth. The Heliospheric Magnetic Field. *Living Reviews in Solar Physics*, 10, Nov 2013. DOI: [10.12942/lrsp-2013-5](https://doi.org/10.12942/lrsp-2013-5).

- [39] A. J. Dessler. Solar wind and interplanetary magnetic field. *Reviews of Geophysics*, 5(1):1–41, 1967. DOI: [10.1029/RG005i001p00001](https://doi.org/10.1029/RG005i001p00001).
- [40] R. Cowen. Voyager 1 has reached interstellar space. *Nature*, 2013. DOI: [10.1038/nature.2013.13735](https://doi.org/10.1038/nature.2013.13735).
- [41] NASA. Solar wind at voyager 1, 2012. Retrieved 16:20, July 20, 2022 from: [https://commons.wikimedia.org/wiki/File:Solar\\_wind\\_at\\_Voyager\\_1.png](https://commons.wikimedia.org/wiki/File:Solar_wind_at_Voyager_1.png).
- [42] D. H. Hathaway. The Solar Cycle. *Living Reviews in Solar Physics*, 7(1):1, Dec 2010. DOI: [10.12942/lrsp-2010-1](https://doi.org/10.12942/lrsp-2010-1).
- [43] C. Jorgensen et al. Christian Horrebow’s Sunspot Observations – I. Life and Published Writings. *Solar Physics*, 294:77, Jun 2019. DOI: [10.1007/s11207-019-1465-z](https://doi.org/10.1007/s11207-019-1465-z).
- [44] K. Christoffer et al. Christian Horrebow’s Sunspot Observations – II. Construction of a Record of Sunspot Positions. *Solar Physics*, 294:78, Jun 2019. DOI: [10.1007/s11207-019-1466-y](https://doi.org/10.1007/s11207-019-1466-y).
- [45] L. Gleeson and W. Axford. Solar Modulation of Galactic Cosmic Rays. *Astrophysical Journal*, 154:1011, Dec 1968. DOI: [10.1086/149822](https://doi.org/10.1086/149822).
- [46] E. Ross and W. J. Chaplin. The behaviour of galactic cosmic ray intensity during solar activity cycle 24. *Solar Physics*, 294(1):8, Jan 2019. DOI: [10.1007/s11207-019-1397-7](https://doi.org/10.1007/s11207-019-1397-7).
- [47] M. Aguilar et al. (AMS Collaboration). Observation of complex time structures in the cosmic-ray electron and positron fluxes with the alpha magnetic spectrometer on the international space station. *Phys. Rev. Lett.*, 121:051102, Jul 2018. DOI: [10.1103/PhysRevLett.121.051102](https://doi.org/10.1103/PhysRevLett.121.051102).
- [48] NobelPrize.org (Nobel Media AB). The Nobel Prize in Physics 1959, 2022. URL: <https://www.nobelprize.org/prizes/physics/1959/summary>.
- [49] K. Anraku et al. (BESS Collaboration). Balloon borne experiment using a superconducting solenoidal magnet spectrometer. In *KEK-PREPRINT-94-40*, 6 1994. URL: <https://lib-extopc.kek.jp/preprints/PDF/1994/9427/9427040.pdf>.
- [50] M. Nozaki for the BESS-Polar Collaboration. BESS-Polar. *Nuclear Instruments and Methods in Physics Research Section B: Beam Interactions with Materials and Atoms*, 214:110–115, 2004. DOI: [10.1016/j.nimb.2003.08.005](https://doi.org/10.1016/j.nimb.2003.08.005).
- [51] T. Yoshida et al. Bess-polar experiment. *Life sciences and space research*, 33(10):1755–1762, 2004. DOI: [10.1016/j.asr.2003.05.017](https://doi.org/10.1016/j.asr.2003.05.017).
- [52] K. Abe et al. (BESS Collaboration). Measurement of the cosmic-ray low-energy

- antiproton spectrum with the first BESS-Polar Antarctic flight. *Physics Letters B*, 670(2):103–108, 2008. DOI: [10.1016/j.physletb.2008.10.053](https://doi.org/10.1016/j.physletb.2008.10.053).
- [53] K. Abe et al. (BESS Collaboration). Measurement of the Cosmic-Ray Antiproton Spectrum at Solar Minimum with a Long-Duration Balloon Flight over Antarctica. *Phys. Rev. Lett.*, 108:051102, Jan 2012. DOI: [10.1103/PhysRevLett.108.051102](https://doi.org/10.1103/PhysRevLett.108.051102).
  - [54] A. M. Galper et al. The PAMELA experiment: a decade of Cosmic Ray Physics in space. *Journal of Physics: Conference Series*, 798:012033, Jan 2017. DOI: [10.1088/1742-6596/798/1/012033](https://doi.org/10.1088/1742-6596/798/1/012033).
  - [55] O. Adriani et al. (PAMELA Collaboration). New Measurement of the Antiproton-to-Proton Flux Ratio up to 100 GeV in the Cosmic Radiation. *Phys. Rev. Lett.*, 102:051101, Feb 2009. DOI: [10.1103/PhysRevLett.102.051101](https://doi.org/10.1103/PhysRevLett.102.051101).
  - [56] O. Adriani et al. (PAMELA Collaboration). PAMELA Results on the Cosmic-Ray Antiproton Flux from 60 MeV to 180 GeV in Kinetic Energy. *Phys. Rev. Lett.*, 105:121101, Sep 2010. DOI: [10.1103/PhysRevLett.105.121101](https://doi.org/10.1103/PhysRevLett.105.121101).
  - [57] M. Aguilar et al. (AMS Collaboration). Antiproton Flux, Antiproton-to-Proton Flux Ratio, and Properties of Elementary Particle Fluxes in Primary Cosmic Rays Measured with the Alpha Magnetic Spectrometer on the International Space Station. *Phys. Rev. Lett.*, 117:091103, Aug 2016. DOI: [10.1103/PhysRevLett.117.091103](https://doi.org/10.1103/PhysRevLett.117.091103).
  - [58] S. Haino et al. Measurement of cosmic-ray antiproton spectrum with BESS-2002. In *29th International Cosmic Ray Conference*, volume 3, page 13, Jan 2005. URL: <https://ui.adsabs.harvard.edu/abs/2005ICRC....3...13H>.
  - [59] Y. Asaoka et al. Measurements of Cosmic-Ray Low-Energy Antiproton and Proton Spectra in a Transient Period of Solar Field Reversal. *PhysRevLett*, 88(5):051101, Feb 2002. DOI: [10.1103/PhysRevLett.88.051101](https://doi.org/10.1103/PhysRevLett.88.051101).
  - [60] A. Moiseev et al. Cosmic-Ray Antiproton Flux in the Energy Range from 200 to 600 MeV. *The Astrophysical Journal*, 474(1):479–489, Jan 1997. DOI: [10.1086/303463](https://doi.org/10.1086/303463).
  - [61] H. Matsunaga et al. Measurement of Low-Energy Cosmic-Ray Antiprotons at Solar Minimum. *PhysRevLett*, 81(19):4052–4055, Nov 1998. DOI: [10.1103/PhysRevLett.81.4052](https://doi.org/10.1103/PhysRevLett.81.4052).
  - [62] S. Orito et al. Precision Measurement of Cosmic-Ray Antiproton Spectrum. *Phys-RevLett*, 84(6):1078–1081, Feb 2000. DOI: [10.1103/PhysRevLett.84.1078](https://doi.org/10.1103/PhysRevLett.84.1078).
  - [63] T. Maeno et al. Successive measurements of cosmic-ray antiproton spectrum in a positive phase of the solar cycle. *Astroparticle Physics*, 16(2):121–128, Nov 2001. DOI: [10.1016/S0927-6505\(01\)00107-4](https://doi.org/10.1016/S0927-6505(01)00107-4).

- [64] M. Boezio et al. The Cosmic-Ray Antiproton Flux between 0.62 and 3.19 GeV Measured Near Solar Minimum Activity. *The Astrophysical Journal*, 487(1):415–423, Sep 1997. DOI: [10.1086/304593](https://doi.org/10.1086/304593).
- [65] M. Boezio et al. The Cosmic-Ray Antiproton Flux between 3 and 49 GeV. *The Astrophysical Journal*, 561(2):787–799, Nov 2001. DOI: [10.1086/323366](https://doi.org/10.1086/323366).
- [66] J. Mitchell et al. Measurement of 0.25-3.2 GeV Antiprotons in the Cosmic Radiation. *PhysRevLett*, 76(17):3057–3060, Apr 1996. DOI: [10.1103/PhysRevLett.76.3057](https://doi.org/10.1103/PhysRevLett.76.3057).
- [67] G. Basini. The Flux of Cosmic Ray Antiprotons from 3.7 to 24 GeV. In *26th International Cosmic Ray Conference*, volume 3, page 77, Aug 1999. URL: <https://ui.adsabs.harvard.edu/abs/1999ICRC....3...77B>.
- [68] M. Aguilar et al. (AMS Collaboration). Precision Measurement of the Proton Flux in Primary Cosmic Rays from Rigidity 1 GV to 1.8 TV with the Alpha Magnetic Spectrometer on the International Space Station. *Phys. Rev. Lett.*, 114:171103, Apr 2015. DOI: [10.1103/PhysRevLett.114.171103](https://doi.org/10.1103/PhysRevLett.114.171103).
- [69] Q. An et al. Measurement of the cosmic-ray proton spectrum from 40 GeV to 100 TeV with the DAMPE satellite. *Science Advances*, 5(9):eaax3793, 2019. DOI: [10.1126/sci-adv.aax3793](https://doi.org/10.1126/sci-adv.aax3793).
- [70] O. Adriani et al. PAMELA Measurements of Cosmic-Ray Proton and Helium Spectra. *Science*, 332(6025):69–72, 2011. DOI: [10.1126/science.1199172](https://doi.org/10.1126/science.1199172).
- [71] A. D. Panov et al. Energy Spectra of Abundant Nuclei of Primary Cosmic Rays from the Data of ATIC-2 Experiment: Final Results. *Bulletin of the Russian Academy of Sciences: Physics*, 73(5):564–567, 2009. DOI: [10.3103/S1062873809050098](https://doi.org/10.3103/S1062873809050098).
- [72] Y. S. Yoon et al. Proton and Helium Spectra from the CREAM-III Flight. *The Astrophysical Journal*, 839(1):5, 2017. DOI: [10.3847/1538-4357/aa68e4](https://doi.org/10.3847/1538-4357/aa68e4).
- [73] E. Atkin et al. New Universal Cosmic-Ray Knee near a Magnetic Rigidity of 10 TV with the NUCLEON Space Observatory. *Jetp Lett*, 108:5–12, 2018. DOI: [10.1134/S0021364018130015](https://doi.org/10.1134/S0021364018130015).
- [74] S. Ahlen et al. An antimatter spectrometer in space. *Nuclear Instruments and Methods in Physics Research Section A: Accelerators, Spectrometers, Detectors and Associated Equipment*, 350(1):351–367, 1994. DOI: [10.1016/0168-9002\(94\)91184-3](https://doi.org/10.1016/0168-9002(94)91184-3).
- [75] R. Battiston. The antimatter spectrometer (AMS-02): A particle physics detector in space. *Nuclear Instruments and Methods in Physics Research Section A: Accelerators, Spectrometers, Detectors and Associated Equipment*, 588(1):227–234, 2008. DOI: [10.1016/j.nima.2008.01.044](https://doi.org/10.1016/j.nima.2008.01.044).

- [76] M. Aguilar et al. (AMS Collaboration). The Alpha Magnetic Spectrometer (AMS) on the International Space Station: Part I - results from the test flight on the space shuttle. *Physics Reports*, 366(6):331–405, 2002. DOI: [10.1016/S0370-1573\(02\)00013-3](https://doi.org/10.1016/S0370-1573(02)00013-3).
- [77] AMS-01 Collaboration. AMS-01 Brochure. URL: <https://ams.cern.ch/ams01/5.htm>.
- [78] Roskosmos. STS-91 PLB, 1998. Retrieved 16:20, July 20, 2022 from: [https://commons.wikimedia.org/wiki/File:STS-91\\_PLB.jpg](https://commons.wikimedia.org/wiki/File:STS-91_PLB.jpg).
- [79] NASA/Crew-2. View of the ISS taken during crew-2 flyaround (iss066-e-081311), 2021. Retrieved 16:20, July 20, 2022 from: [https://commons.wikimedia.org/wiki/File:View\\_of\\_the\\_ISS\\_taken\\_during\\_Crew-2\\_flyaround\\_\(ISS066-E-081311\).jpg](https://commons.wikimedia.org/wiki/File:View_of_the_ISS_taken_during_Crew-2_flyaround_(ISS066-E-081311).jpg).
- [80] M. Aguilar et al. (AMS Collaboration). The Alpha Magnetic Spectrometer (AMS) on the international space station: Part II – Results from the first seven years. *Physics Reports*, 894:1–116, Feb 2021. DOI: [10.1016/j.physrep.2020.09.003](https://doi.org/10.1016/j.physrep.2020.09.003).
- [81] AMS Collaboration. The Alpha Magnetic Spectrometer on the International Space Station, 2022. URL: <https://ams02.space>.
- [82] V. L. Ginzburg and I. M. Frank. Radiation of a Uniformly Moving Electron Due to Its Transition from One Medium to Another. *J. Phys. (USSR)*, 9:353–362, 1945.
- [83] M. Heil et al. Operations and Alignment of the AMS-02 Transition Radiation Detector. In *33rd International Cosmic Ray Conference*, page 1232, 2013. URL: <https://www.cbpf.br/icrc2013/papers/icrc2013-1232.pdf>.
- [84] T. Siedenburg. The AMS TRD. A gasdetector designed for operation in space. *Nuclear Physics B - Proceedings Supplements*, 150:30–33, 2006. DOI: [10.1016/j.nuclphysbps.2004.06.001](https://doi.org/10.1016/j.nuclphysbps.2004.06.001).
- [85] T. Kirn. The AMS-02 transition radiation detector. *Nuclear Instruments and Methods in Physics Research Section A: Accelerators, Spectrometers, Detectors and Associated Equipment*, 581(1):156–159, 2007. DOI: [10.1016/j.nima.2007.07.052](https://doi.org/10.1016/j.nima.2007.07.052).
- [86] D. Haas. The Silicon Tracker of AMS02. *Nuclear Instruments and Methods in Physics Research Section A: Accelerators, Spectrometers, Detectors and Associated Equipment*, 530(1):173–177, 2004. DOI: [10.1016/j.nima.2004.05.068](https://doi.org/10.1016/j.nima.2004.05.068).
- [87] P. E. Saouter. Operation and Performance of AMS-02 Silicon Tracker. *PoS, Vertex2014:028*, 2015. DOI: [10.22323/1.227.0028](https://doi.org/10.22323/1.227.0028).
- [88] S. Haino. Performance of the AMS-02 silicon tracker in the ISS mission. *Nuclear Instruments and Methods in Physics Research Section A: Accelerators, Spectrometers, Detectors and Associated Equipment*, 699:221–224, 2013. DOI: [10.1016/j.nima.2012.05.060](https://doi.org/10.1016/j.nima.2012.05.060).

- [89] G. Ambrosi et al. Alignment of the AMS-02 Silicon Tracker. In *33rd International Cosmic Ray Conference*, page 1260, 2013. URL: <https://ui.adsabs.harvard.edu/abs/2013ICRC...33..570A>.
- [90] B. Alpat et al. The internal alignment and position resolution of the ams-02 silicon tracker determined with cosmic-ray muons. *Nuclear Instruments and Methods in Physics Research Section A: Accelerators, Spectrometers, Detectors and Associated Equipment*, 613(2):207–217, 2010. DOI: [10.1016/j.nima.2009.11.065](https://doi.org/10.1016/j.nima.2009.11.065).
- [91] R. L. Gluckstern. Uncertainties in track momentum and direction, due to multiple scattering and measurement errors. *Nuclear Instruments and Methods*, 24:381–389, Jul 1963. DOI: [10.1016/0029-554X\(63\)90347-1](https://doi.org/10.1016/0029-554X(63)90347-1).
- [92] P. Zuccon. AMS-02 Track reconstruction and rigidity measurement. In *33rd International Cosmic Ray Conference*, page 1064, 2013. URL: <https://s3.cern.ch/inspire-prod-files-7/71c48c76263c1f7bee2621c779ba3320>.
- [93] V. Bindi et al. Calibration and performance of the AMS-02 time of flight detector in space. *Nuclear Instruments and Methods in Physics Research Section A: Accelerators, Spectrometers, Detectors and Associated Equipment*, 743:22–29, 2014. DOI: [10.1016/j.nima.2014.01.002](https://doi.org/10.1016/j.nima.2014.01.002).
- [94] V. Bindi et al. The time of flight detector of the AMS-02 experiment on the international space station. *Nuclear Instruments and Methods in Physics Research Section A: Accelerators, Spectrometers, Detectors and Associated Equipment*, 718:478–480, 2013. DOI: [10.1016/j.nima.2012.11.061](https://doi.org/10.1016/j.nima.2012.11.061).
- [95] V. Bindi et al. The AMS-02 Time of Flight (TOF) System: Construction and Overall Performances in Space. In *International Cosmic Ray Conference*, volume 33, page 2298, Jan 2013. URL: <https://ui.adsabs.harvard.edu/abs/2013ICRC...33.2298B>.
- [96] L. Hu et al. The RICH detector of AMS-02: 5 years of operation in space. *Nuclear Instruments and Methods in Physics Research Section A: Accelerators, Spectrometers, Detectors and Associated Equipment*, 876:5–8, 2017. DOI: [10.1016/j.nima.2016.12.011](https://doi.org/10.1016/j.nima.2016.12.011).
- [97] R. Pereira. The AMS-02 RICH detector: Performance during ground-based data taking at CERN. *Nuclear Instruments and Methods in Physics Research Section A: Accelerators, Spectrometers, Detectors and Associated Equipment*, 639:37–41, 2011. DOI: [10.1016/j.nima.2010.09.036](https://doi.org/10.1016/j.nima.2010.09.036).
- [98] F. Giovacchini, J. Casaus, and A. Oliva. The AMS-02 RICH detector: Status and physics results. *Nuclear Instruments and Methods in Physics Research Section A: Accelerators, Spectrometers, Detectors and Associated Equipment*, 952:161797, 2020. DOI: [10.1016/j.nima.2019.01.024](https://doi.org/10.1016/j.nima.2019.01.024).

- [99] F. Giovacchini. Performance in space of the AMS-02 RICH detector. *Nuclear Instruments and Methods in Physics Research Section A: Accelerators, Spectrometers, Detectors and Associated Equipment*, 766:57–60, 2014. DOI: [10.1016/j.nima.2014.04.036](https://doi.org/10.1016/j.nima.2014.04.036).
- [100] R. L. Sylvie. Performance of the AMS02 electromagnetic calorimeter in space. *Journal of Physics: Conference Series*, 404:012034, 2012. DOI: [10.1088/1742-6596/404/1/012034](https://doi.org/10.1088/1742-6596/404/1/012034).
- [101] M. Vecchi et al. The electromagnetic calorimeter of the AMS-02 experiment. In *Semaine de l’Astrophysique Francaise (SF2A 2012)*, Nice, France, Jun 2012. URL: <http://hal.in2p3.fr/in2p3-00745677>.
- [102] C. Adloff et al. The AMS-02 lead-scintillating fibres Electromagnetic Calorimeter. *Nuclear Instruments and Methods in Physics Research Section A: Accelerators, Spectrometers, Detectors and Associated Equipment*, 714:147–154, 2013. DOI: [10.1016/j.nima.2013.02.020](https://doi.org/10.1016/j.nima.2013.02.020).
- [103] I. Marco. Performance of the AMS-02 Electromagnetic Calorimeter in Space. *PoS*, TIPP2014:025, 2014. DOI: [10.22323/1.213.0025](https://doi.org/10.22323/1.213.0025).
- [104] M. Vecchi, K. Wu, and Y. Chang. A 3-dimensional electromagnetic shower characterization and its application to AMS-02 pointing capability. In *33rd International Cosmic Ray Conference*, page 0653, 2013. URL: <https://www.cbpf.br/icrc2013/papers/icrc2013-0653.pdf>.
- [105] G. Gallucci and (for the AMS-02 ECAL group). Performance of the AMS-02 Electromagnetic Calorimeter in Space. *Journal of Physics: Conference Series*, 587:012028, Feb 2015. DOI: [10.1088/1742-6596/587/1/012028](https://doi.org/10.1088/1742-6596/587/1/012028).
- [106] D. F. Stefano. Results of 2007 test beam of AMS-02 Electromagnetic Calorimeter. *Advances in Space Research*, 45:112–122, 2010. DOI: [10.1016/j.asr.2009.08.005](https://doi.org/10.1016/j.asr.2009.08.005).
- [107] P. von Doetinchem et al. The AMS-02 Anticoincidence Counter. *Nuclear Physics B - Proceedings Supplements*, 197:15–18, 2009. DOI: [10.1016/j.nuclphysbps.2009.10.025](https://doi.org/10.1016/j.nuclphysbps.2009.10.025).
- [108] T. Bruch and W. Wallraff. The Anti-Coincidence Counter shield of the AMS tracker. *Nuclear Instruments and Methods in Physics Research Section A: Accelerators, Spectrometers, Detectors and Associated Equipment*, 572:505–507, 2007. DOI: [10.1016/j.nima.2006.10.376](https://doi.org/10.1016/j.nima.2006.10.376).
- [109] A. Basili et al. The TOF-ACC flight electronics for the fast trigger and time of flight of the AMS-02 cosmic ray spectrometer. *Nuclear Instruments and Methods in Physics Research Section A: Accelerators, Spectrometers, Detectors and Associated Equipment*, 707:99–113, 2013. DOI: [10.1016/j.nima.2012.12.089](https://doi.org/10.1016/j.nima.2012.12.089).

- [110] P. von Doetinchem et al. The Anticoincidence Counter System of AMS-02. In *International Cosmic Ray Conference*, Jun 2009. URL: <https://srl.utu.fi/AuxDOC/kocharov/ICRC2009/pdf/icrc1064.pdf>.
- [111] N. Zimmermann. *Precision measurement of the cosmic-ray electron and positron fluxes as a function of time and energy with the Alpha Magnetic Spectrometer on the International Space Station*. Dissertation, RWTH Aachen University, Aachen, 2020. DOI: [10.18154/RWTH-2020-02650](https://doi.org/10.18154/RWTH-2020-02650).
- [112] R. Brun and F. Rademakers. Root - An object oriented data analysis framework. *Nuclear Instruments and Methods in Physics Research Section A: Accelerators, Spectrometers, Detectors and Associated Equipment*, 389(1):81–86, 1997. DOI: [10.1016/S0168-9002\(97\)00048-X](https://doi.org/10.1016/S0168-9002(97)00048-X).
- [113] B. Beischer. *Measurement of high energy gamma rays from 200 MeV to 1 TeV with the Alpha Magnetic Spectrometer on the International Space Station*. Dissertation, RWTH Aachen University, Aachen, 2020. DOI: [10.18154/RWTH-2020-06535](https://doi.org/10.18154/RWTH-2020-06535).
- [114] S. Agostinelli et al. GEANT4—a simulation toolkit. *Nuclear Instruments and Methods in Physics Research Section A: Accelerators, Spectrometers, Detectors and Associated Equipment*, 506:250–303, 2003. DOI: [10.1016/S0168-9002\(03\)01368-8](https://doi.org/10.1016/S0168-9002(03)01368-8).
- [115] J. Allison et al. Recent developments in geant4. *Nuclear Instruments and Methods in Physics Research Section A: Accelerators, Spectrometers, Detectors and Associated Equipment*, 835:186–225, 2016. DOI: [10.1016/j.nima.2016.06.125](https://doi.org/10.1016/j.nima.2016.06.125).
- [116] V. Helge et al. TMVA, the toolkit for multivariate data analysis with ROOT. In XI International Workshop on Advanced Computing and Analysis Techniques in Physics Research, volume 50, page 040. SISSA Medialab, 2009. DOI: [10.22323/1.050.0040](https://doi.org/10.22323/1.050.0040).
- [117] J. Neyman, E. S. Pearson, and K. Pearson. Ix. On the problem of the most efficient tests of statistical hypotheses. *Philosophical Transactions of the Royal Society of London. Series A, Containing Papers of a Mathematical or Physical Character*, 231(694-706):289–337, 1933. DOI: [10.1098/rsta.1933.0009](https://doi.org/10.1098/rsta.1933.0009).
- [118] T. Kirn. The AMS-02 TRD on the international space station. *Nuclear Instruments and Methods in Physics Research Section A: Accelerators, Spectrometers, Detectors and Associated Equipment*, 706:43–47, 2013. DOI: [10.1016/j.nima.2012.05.010](https://doi.org/10.1016/j.nima.2012.05.010).
- [119] F. James and M. Roos. Minuit - a system for function minimization and analysis of the parameter errors and correlations. *Computer Physics Communications*, 10(6):343–367, 1975. DOI: [10.1016/0010-4655\(75\)90039-9](https://doi.org/10.1016/0010-4655(75)90039-9).
- [120] J. D. Sullivan. Geometric factor and directional response of single and multi-element particle telescopes. *Nuclear Instruments and Methods*, 95(1):5–11, 1971. DOI: [10.1016/0029-5114\(71\)90005-7](https://doi.org/10.1016/0029-5114(71)90005-7).

- [121] K. Nakamura et al. Absorption and Forward Scattering of Antiprotons by C, Al, and Cu Nuclei in the Region 470-880 MeV/c. *Phys. Rev. Lett.*, 52(9):731–734, Feb 1984. DOI: [10.1103/PhysRevLett.52.731](https://doi.org/10.1103/PhysRevLett.52.731).
- [122] A. S. Carroll et al. Absorption cross-sections of  $\pi^\pm$ ,  $k^\pm$ , p and  $\bar{p}$  on nuclei between 60 GeV/c and 280 GeV/c. *Phys. Lett. B*, 80:319–322, 1979. DOI: [10.1016/0370-2693\(79\)90226-0](https://doi.org/10.1016/0370-2693(79)90226-0).
- [123] N. Abgrall et al. Measurements of cross sections and charged pion spectra in proton-carbon interactions at 31 GeV/c. *Phys. Rev. C*, 84:034604, Sep 2011. DOI: [10.1103/PhysRevC.84.034604](https://doi.org/10.1103/PhysRevC.84.034604).
- [124] J. R. Letaw, R. Silberberg, and C. H. Tsao. Proton-nucleus total inelastic cross sections - an empirical formula for E greater than 10 MeV. *Astrophysical Journal Supplement*, 51:271–275, Mar 1983. DOI: [10.1086/190849](https://doi.org/10.1086/190849).
- [125] C. Stormer. The polar aurora. *Quarterly Journal of the Royal Meteorological Society*, 82(351):115–115, 1956. DOI: [10.1002/qj.49708235123](https://doi.org/10.1002/qj.49708235123).
- [126] D. F. Smart and M. A. Shea. A review of geomagnetic cutoff rigidities for earth-orbiting spacecraft. *Advances in Space Research*, 36(10):2012–2020, 2005. DOI: [10.1016/j.asr.2004.09.015](https://doi.org/10.1016/j.asr.2004.09.015).
- [127] T. Adye. Unfolding algorithms and tests using RooUnfold. In *PHYSTAT 2011*, pages 313–318, Geneva, 2011. CERN. DOI: [10.5170/CERN-2011-006.313](https://doi.org/10.5170/CERN-2011-006.313).
- [128] G. D'Agostini. A multidimensional unfolding method based on Bayes' theorem. *Nuclear Instruments and Methods in Physics Research Section A: Accelerators, Spectrometers, Detectors and Associated Equipment*, 362(2):487–498, 1995. DOI: [10.1016/0168-9002\(95\)00274-X](https://doi.org/10.1016/0168-9002(95)00274-X).
- [129] J. W. Bieber et al. Antiprotons at solar maximum. *Phys. Rev. Lett.*, 83:674–677, Jul 1999. DOI: [10.1103/PhysRevLett.83.674](https://doi.org/10.1103/PhysRevLett.83.674).
- [130] M. S. Potgieter et al. A perspective on the solar modulation of cosmic anti-matter. *Physics*, 3(4):1190–1225, 2021. DOI: [10.3390/physics3040076](https://doi.org/10.3390/physics3040076).
- [131] S. Schael et al. AMS-100: The next generation magnetic spectrometer in space - An international science platform for physics and astrophysics at Lagrange point 2. *Nuclear Instruments and Methods in Physics Research Section A: Accelerators, Spectrometers, Detectors and Associated Equipment*, 944:162561, 2019. DOI: [10.1016/j.nima.2019.162561](https://doi.org/10.1016/j.nima.2019.162561).

# Acknowledgements

First, I would like to thank Prof. Dr. Stefan Schael for giving me the opportunity to work in his institute as a member of the AMS-02 collaboration. During the last few years, I have always benefited from his supervision and guidance. His passion for physics and his enthusiasm have really inspired me. Moreover, I have learned a lot from his ambition to push things forward. I would also like to thank Prof. Dr. Christopher Wiebusch for agreeing to be my second supervisor for the thesis.

Secondly, I would like to thank Prof. Samuel Ting, the Primary Investigator of the whole AMS-02 experiment. Without his effort in the last decades, the AMS-02 project would not have come true. His spirit of never giving up will inspire me in the future. In addition, I admire his concentration and perseverance throughout his career.

Many friends and colleagues helped me a lot during my PhD time in Aachen. Special thanks to Robin Sonnabend who helped me from zero ground when I was a beginner in AMS. He is always patient to teach me and answer stupid questions. I would like to thank Dr. Henning Gast. As the actual host in the Aachen analysis group, he put a lot of effort to support the Aachen data analysis.

During my PhD study in the institute, many friends and colleagues have made my working time pleasant: Dr. Nikolas Zimmermann, Dr. Bastian Beischer, Dr. Fabian Machate, Dr. Nikolay Nikonov, Dr. Leila Ali Cavasonza, Dr. Sofia Chouridou, Manbing Li, Emiliano Rampi, and Yasaman Najafi. I have always learned a lot from the discussions with you, and the time I spent with you guys will always be a precious memory for me.

I would like to thank again Dr. Henning Gast and Dr. Sofia Chouridou who did proofreadings for this thesis. Many thanks for your time and valuable comments.

I would like to thank Dr. Georg Schwering, Natalie Driessen, Tanja Bingler and Gina Wilden for their support work in the administration branch of the institute. As a foreigner working in Aachen, I was guided by them in almost every step of my PhD program.

During my shifts at CERN, many friends and colleagues there made my stay enjoyable. I would like to thank Dr. Mike Capell, Dr. Zhili Weng, Dr. Weiwei Xu, Dr. Valery Zhukov, Dr. Youmin Yu, Dr. Baosong Shan, Dr. Yi Jia, Dr. XiaoTing Qin and so many other people. The discussions we had at the POCC had always made my time there delightful.

Last but foremost, I would like to thank my family. Their continuous love and encouragement are the sources of power for me that support me all the time. This thesis wouldn't have been possible without your support.